UNIVERSITEIT
GENT

Faculteit Wetenschappen

Vakgroep Fysica en Sterrenkunde

Determination of the Interstellar Dust Mass in Galaxies using Deep Optical and Near-Infrared Observations

Sébastien VIAENE

Promotor: Prof. dr. M. Baes

Co-promotor: dr. J. Fritz

Academic year 2011 - 2012

Contents

Acknowledgments

Introduction

<div style="text-align: right">1</div>

In the beginning there was nothing,
which exploded.

Terry Pratchett

1.1 Dusty galaxies: status quaestionis

Interstellar dust in galaxies has been topic of research for many decades. The spatial distribution, composition, quantity and origin of this component is up to this day not very well known. The dust has cold temperatures (Amblard et al. 2010), making it only directly visible at far-infrared (FIR) and submm wavelengths. Before the advent of FIR space astronomy, dust could only be detected through extinction and scattering of optical and near-infrared (NIR) starlight. Interstellar dust comes in all sorts and sizes, but the main components consist of small, millimetre sized silicate and carbonaceous grains (Draine & Lee (1984), Zubko et al. (2004)) . The total mass of these dust grains is negligible compared to the gas and stellar masses in galaxies (see e.g. Cortese et al. (2012)). Nevertheless, dust plays a vital role in the way starlight is processed and sent towards observers outside the galaxy. Dust grains are made up of many molecules and thus possess a wide range of possible absorption frequencies, which makes them very effective in absorbing the light from stars. This light heats up the grains and they will function as black bodies, re-emitting their energy at lower, FIR and submm frequencies. With the launch of IRAS, the first FIR fluxes of extragalactic objects could be obtained, yet they still poorly constrained even the most basic dust properties. Recently, Spitzer and especially Herschel made spatially resolved FIR and submm imaging possible, opening a new window for the study of interstellar dust.

Spiral galaxies which are viewed at inclinations of almost 90° are called edge-on spiral galaxies. The extinction by interstellar dust in the plane of these specific spirals adds up along the line of sight, resulting in prominent extinction regions in their optical

and NIR wavelengths. Extinction of the starlight directly points to a higher concentration of interstellar dust. Deep imaging of such dust-rich galaxies show prominent dust lanes, vertically constrained as a thin, dark line which runs through the galaxy's center. Hence, these type of galaxies can be used to investigate both the vertical extent and the extinction properties of interstellar dust. These dusty structures can also be seen in the FIR and submm imaging by the Herschel Space Telescope. It is clear that new technologies from optical to submm imaging provide the astronomical community with a huge amount of information from which the dust properties of edge-on spirals can be accurately determined.

Much later than the dust lane edge-ons, prominent dust structures were discovered in early type galaxies (Sadler & Gerhard 1985; Hawarden et al. 1981). Although it was once thought that elliptical galaxies did not hold much interstellar matter, a significant fraction of ellipticals were found to have dust lanes. Consequently recent efforts have been made to observe early-type galaxies with the Herschel telescope and extend the study of interstellar dust to this group of galaxies (De Geyter et al. 2012).

Two simple approaches are used to make estimates of the dust mass and its distribution. One way is to investigate the spatial and wavelength dependency of galaxy fluxes, hereby carefully separating the extinction effects from dust and the wavelength dependency of the stellar luminosity. Once this relation is known, it is possible to fit a theoretical dust model to the observations and translate extinction to optical depth and dust mass. This process is called reddening and is the most basic way of determining the dust mass (Goudfrooij et al. 1994). Another approach makes uses of the direct dust fluxes in FIR and submm. Dust models can make a link between the intensity of the dust radiation and its mass (Gordon et al. 2010). These two techniques should be consistent, i.e. the energy from starlight should be converted and re-emitted at longer wavelengths. This dust energy balance, however, is not fulfilled for any of the investigated galaxies. As it appears, the FIR/submm emission is systematically underestimated by a factor of about three for all galaxies (Popescu et al. 2000; Misiriotis et al. 2001; Alton et al. 2004; Dasyra et al. 2005; Baes et al. 2010). A possible explanation for this discrepancy are clumpy dust structures who don't play a large role in extinction, but do in emission (Bianchi 2008). Another reason may be a severe underestimation of the FIR/submm emissivity in the used dust models, although this seems rather unlikely (Baes et al. 2010). In any case, there is need of additional galaxy samples and detailed modelling to accurately constrain the properties of interstellar dust.

The best way to accurately test the dust energy balance is to treat extinction and emission in a self-consistent way by fully computing the path of each photon from its birth in the star to its detection by telescope. This requires full 3-D radiative transfer modelling, a tedious task that requires a lot of computing power and complex algorithms

to include all the physical interactions acting between the dust and photons (Alton et al. 2004; Kylafis & Bahcall 1987; Xilouris et al. 1999; Baes et al. 2010). The use of 3-D galaxy models will give greater insight to the spatial distribution of interstellar dust, its composition and the way it influences our view of the universe.

This work reports the acquisition and reduction of optical and NIR observations for various projects involving dusty galaxies. This chapter outlines the various projects and their goals; chapter 2 reports the acquisition of optical data and a detailed explanation of the data reduction. chapters 3, 4 and 5 presents data from various observing runs along with the data reduction. As a second part, dust masses for several elliptical galaxies are determined by two different approaches in chapter 6. Finally, chapter 7 discusses the results of this research and presents the overall conclusions.

1.2	HEROES

The HERschel Observations of Edge-On Spirals (HEROES) project (Verstappen et al. 2012) is one of the main Herschel projects led by Ghent University. The project aims to investigate the dust properties and energy balance of 7 large edge-on galaxies. This will be done, for the first time, by imaging the galaxies in FIR and submm wavelengths using both the Photoconductor Array Camera and Spectrometer (PACS, Poglitsch et al. (2010)) and the Spectral and Photometric Imaging REceiver (SPIRE, Griffin et al. (2010)) instruments aboard the Herschel Space Observatory (ESA 2012). Apart from FIR and submm coverage, which will image the dust directly through its emission in these wavelengths, there is also need for imaging and photometry at other wavelengths. On the long wavelength side of the spectrum, radio observations near the the HI and CO emission lines are required to map the atomic and molecular gas distribution and density of the sample (Allaert et al. 2012). On the shorter wavelength part of the spectrum, observations will eventually cover near infrared, optical and ultra-violet wavelengths, suitable to investigate the role of the interstellar dust in extinction and scattering of starlight. Table 1.1 lists the HEROES sample and their basic properties.

Eventually panchromatic 3-D radiative transfer models will be fitted to the observed galaxies to not only map the 3-D dust distribution, but also study the energy balance of the galaxies. These 3-D models use the UV, optical and NIR fluxes to predict the FIR and submm fluxes by detailed radiative transfer computations in a dusty environment. Previous studies on this energy balance of edge-on galaxies (Popescu et al. (2000); Misiriotis et al. (2001); Alton et al. (2004); Dasyra et al. (2005); Baes et al. (2010) systematically underestimate the FIR and submm flux. A better understanding of this

Galaxy	RA (J2000)	Dec (J2000)	Size	D (Mpc)	m_B	This work
UGC 2048	$02:34:20.1$	$+32:30:20.0$	$4.1' \times 0.5'$	63.5	13.8	✓
UGC 4277	$08:13:57.2$	$+52:38:54.0$	$4.0' \times 0.4'$	76.5	14.4	✓
IC 2531	$09:59:55.8$	$-29:37:01.0$	$7.5' \times 0.9'$	36.8	13.2	
NGC 4013	$11:58:31.4$	$+43:56:48.0$	$5.2' \times 1.0'$	18.6	12.4	
NGC 4217	$12:15:50.9$	$+47:05:30.0$	$5.2' \times 1.5'$	19.6	12.4	
NGC 5529	$14:15:34.1$	$+36:13:36.0$	$6.3' \times 0.6'$	49.5	12.9	✓
NGC 5907	$15:15:53.8$	$+56:19:44.0$	$12.7' \times 1.4'$	16.3	11.4	✓

Table 1.1: Overview of the HEROES sample. The last column indicates the galaxies treated in this work. These objects were observed in both optical and NIR bands.

curiosity will be the ultimate goal of the HEROES project. This work presents the acquiring of optical and near-infrared observations of several northern galaxies of the HEROES sample. Some observations were acquired directly through visitor mode observations (see chapter 2). Other observations were requested and performed in service mode, see chapters 3 and 4.

1.3 NHEMESES

NHEMESES: The New HErschel Multi-wavelength Extragalactic Survey of Edge-on Spirals (Holwerda et al. 2011) can be seen as an expansion of HEROES to less massive edge-on galaxies. It has been noted (Dalcanton et al. 2004) that the vertical extent of the dust distribution in edge-ons depends on the overall galaxy mass. Speculations go so far as to say that there is a phase change in the interstellar medium (ISM). The largest and most massive galaxies, which coincide with the HEROES sample, feature a thin and smooth primary dust lane accompanied with a secondary extended dusty envelope, associated with HI gas. Less massive edge-ons show a less smooth dust lane, clumpy structures, or no significant dust lane at all. A sample of 12 nearby edge-on galaxies of low and intermediate mass has been constructed and is being observed by both PACS and SPIRE instruments on Herschel (see table 1.2). For the first time, the dusty features of these galaxies will be resolved at FIR and submm wavelengths and will permit the study of a phase change in the ISM.

Secondly, optical and NIR data of this sample will be acquired through ground-based observations. From this optical and NIR imaging, it will be possible to study the extinction and scattering of the dust in the different regions of the galaxies. Comparing these with the emission of the dust in the FIR and submm, detailed energy balance studies can be carried out to constrain the properties of dust in the ISM and its effect

Galaxy	RA (J2000)	Dec (J2000)	Size	D (Mpc)	m_B	This work
IC2233	08 : 13 : 58.9	+45 : 44 : 32.0	$4.7' \times 0.5'$	13.4	13.1	✓
NGC3501	11 : 02 : 47.3	+17 : 59 : 22.0	$2.6' \times 0.4'$	22.93	13.8	
NGC4144	12 : 09 : 58.6	+46 : 27 : 26.0	$4.2' \times 1.4'$	6.6	12.3	✓
NGC4183	12 : 13 : 16.9	+43 : 41 : 55.0	$3.9' \times 1.2'$	16.7	13.5	✓
NGC4206	12 : 15 : 16.8	+13 : 01 : 26.0	$4.1' \times 0.8'$	19.9	12.8	
NGC4244	12 : 17 : 29.6	+37 : 48 : 26.0	$9.2' \times 2.8'$	4.6	10.8	✓
UGC7321	12 : 17 : 34.0	+22 : 32 : 25.0	$4.0' \times 0.6'$	3.8	14.5	✓
NGC4460	12 : 28 : 45.5	+44 : 51 : 51.0	$3.0' \times 0.9'$	8.8	12.5	✓
NGC4526	12 : 34 : 03.0	+07 : 41 : 57.0	$4.7' \times 2.0'$	15.2	10.6	
NGC4634	12 : 42 : 40.9	+14 : 17 : 44.9	$2.6' \times 0.4'$	4.0	13.6	
NGC5023	13 : 12 : 12.6	+44 : 02 : 28.0	$5.3' \times 1.4'$	9.0	13.2	✓
NGC5746	14 : 15 : 34.1	+36 : 13 : 36.0	$5.7' \times 1.5'$	29.0	12.3	

Table 1.2: Overview of the NHEMESES sample. The last column indicates the galaxies treated in this work. These objects were observed in both optical and NIR bands.

on starlight. Unlike the HEROES project, galaxy modelling will be done through spiral disk Spectral Energy Distribution (SED) models. This type of modelling has gained a lot of accuracy and sophistication in the last decade (Bianchi & Xilouris 2011; Popescu et al. 2011; MacLachlan et al. 2011; Baes et al. 2010). This work focusses on the observing and data reduction of optical and NIR data of most of the northern and equatorial NHEMESES galaxies.

1.4   FRIEDL

The Far-infraRed Investigation of Early-type galaxies with Dust Lanes (FRIEDL) focusses on elliptical galaxies which show prominent dust lanes. Early-type galaxies were once thought not to hold much interstellar matter and subsequently not suffering from extinction by dust. However the recognition of dust lanes and their extinction of starlight in some early type galaxies led to a new way to investigate the nature of interstellar dust (Brosch 1988). Because of their elliptical shape, and smooth light distribution, early type galaxies with prominent dust lanes are quite easy to model, making these the ideal test laboratories to study dust and ISM properties in other galaxies. 11 elliptical galaxies with very regular shapes and prominent dust lanes were chosen. Their smooth and symmetric shapes will make it easier to model and allows a detailed study of the ISM. Table 1.3 lists the basic properties of the FRIEDL sample.

Just like the HEROES and NHEMESES projects, a large wavelength interval will be

Galaxy	RA (J2000)	Dec (J2000)	Size	D (Mpc)	m_B	This work
NGC2534	08 : 12 : 54.1	+55 : 40 : 19.0	$0.8' \times 0.8'$	48	15.1	✓
NGC2907	09 : 31 : 36.7	−16 : 44 : 05.0	$1.8' \times 1.1'$	28	13.0	
NGC3283	10 : 31 : 11.6	−46 : 15 : 05.0	$2.1' \times 1.3'$	36	12.7	
NGC3497	11 : 07 : 18.1	−19 : 28 : 18.0	$1.7' \times 1.1'$	48	12.8	
NGC3665	11 : 24 : 43.7	+38 : 45 : 46.0	$2.3' \times 1.8'$	32	13.3	✓
NGC4370	12 : 24 : 54.9	+07 : 26 : 42.0	$1.5' \times 0.8'$	10	15.6	✓
NGC5485	14 : 07 : 11.3	+55 : 00 : 06.0	$2.0' \times 1.6'$	27	13.8	✓
NGC5525	14 : 15 : 39.2	+14 : 16 : 57.0	$1.4' \times 0.7'$	76	14.1	✓
NGC5626	14 : 29 : 49.1	−29 : 44 : 54.0	$1.2' \times 1.1'$	93	14.0	
NGC5799	15 : 05 : 35.2	−72 : 25 : 58.0	$1.1' \times 0.8'$	31	13.5	
NGC5866	15 : 06 : 29.5	+55 : 45 : 48.0	$3.5' \times 1.5'$	15	10.7	

Table 1.3: Overview of the FRIEDL sample.The last column indicates the galaxies treated in this work. These objects were observed in both optical and NIR bands.

covered by both space and ground based observations. Herschel will image the galaxies in both PACS and SPIRE to cover the FIR and submm part. UV, optical and NIR observations will complete the panchromatic dataset. As a first study, the galaxies will be modelled with a multi-Gaussian expansion set based on the optical and NIR data. This will yield dust-free galaxy models. These will then be subtracted from the observations to produce dust maps. Also based on the optical and NIR data, colour difference maps will be constructed to compare with the dust maps from the modelling. This way, basic dust properties and morphologies can be derived. In a second phase, panchromatic 3-D radiative transfer models will be computed to make an in depth study of the dust distribution, composition and properties. The energy balance in these galaxies will be investigated and compared with the HEROES and NHEMESES results. This work will present the data reduction of the optical data and the expansion of the dataset to UV and NIR. Chapter 6 will cover the modelling, construction of extinction maps and deriving dust properties and morphology.

The Skinakas Observing run

<div align="right">

2

</div>

Keep your eyes on the stars, and your feet on the ground.

Theodore Roosevelt

As a part of this thesis, an observing run was organized in collaboration with the National Observatory of Athens. The goal was to obtain optical data of HEROES and NHEMESES galaxies to further complete the dataset.

2.1   Site and Observations

Because of the fairly large galaxies in the sample, a suitable telescope had to be chosen, preferably with a field of view of at least 9 arcmin. Because of the tight collaboration between the University of Ghent and the National Observatory of Athens, a Greek telescope was an obvious choice. Telescope time for the 1.3m telescope at the Skinakas observatory was awarded for the nights of the 25th to the 29th of July 2011.

2.1.1   Site

The Skinakas Observatory (UOC 2012) is located on mount Ida at the centre of the island Crete, Greece. The site was constructed in 1984 as a joint effort of the University of Crete and the Max-Planck-Institut für Extraterrestrische Physik (Germany). Located on a small island at high altitude makes Skinakas one of the best astronomical sites of Europe with the potential to achieve an astronomical seeing down to 0.6 arcseconds. With a sky brightness in V band of 21.74 magnitudes per square arcsecond, Skinakas is a dark site, suitable for imaging faint objects such as galaxies. During the observing nights for this project, the weather was not ideal, but good enough for the required accuracy. Air humidity kept below 51% and wind speeds up to 40km/h were measured, leading to a seeing between 1.54″ and 2.25″ with an average of 1.83″.

Figure 2.1: View of the Skinakas observatory site with the three telescopes.

2.1.2 Instrumental setup

The 1.3 m telescope, a modified Ritchey–Chrétien telescope with a focal length of 9.86 m, was used to do the observing. It deviates from the standard Ritchey–Chrétien model in the sense that both primary and secondary mirrors are hyperbolic. This has the advantage to create a large field of view of about 9 arcminutes with a high image quality. The telescope, which was commissioned in 1995, has an equatorial mount, is computer controlled and equipped with tracking and an off-axis autoguider system. The device is thus suitable for professional observations and acquisition of scientific data. The used CCD camera is an ANDOR iKon-L DW436 Large-Area camera cooled down to $-72°$ centigrade and set at 1x1 binning. At these temperatures, the dark current is negligible. The back illuminated CCD chip has a quantum efficiency above 90%, is linear up to 50000 e$^-$ and over exposes at 2^{16} e$^-$. The gain factor is 1 e$^-$/ADU and the readout noise about 2.24 e$^-$. Attached is a filter wheel, bearing Johnson-Cousins B,V and R filters with central wavelengths of 4350 Å, 5380 Å and 6300 Å respectively. In combination with the 1.3 m telescope, each pixel covers a sky surface of 0.28×0.28 arcseconds squared and 1×1 binning provides 2048×2048 pixels.

Figure 2.2: The 1.3 m telescope of the Skinakas observatory in Greece.

2.1.3 Observing run

As mentioned before, this observing run consisted out of four nights which turned out to have decent weather quality. The Moon had just passed its last quarter phase, making the nights dark enough for the observation of galaxies. A list of proposed objects was constructed for which additional data was needed. Visibilities were calculated and an observing priority was given to each of the galaxies. HEROES galaxies gained priority one, NHEMESES galaxies priority two and other galaxies priority three and four. Because there were no long periods of bad weather during the nights, all planned observation could be carried out. Both imaging and photometric calibration are needed to make a reliable scientific observation of an object. Apart from the galaxies themselves, also bias frames, sky flat fields and photometric standard stars were observed each night.

Science objects

The science objects in this case are the edge-on galaxies. Three HEROES galaxies were observed in B, V and R filters: UGC 2048, NGC 5529 and NGC 5907. One NHEMESES galaxy, NGC 5023 was observed in all three B, V and R filters. Additionally, NGC 0128 and NGC 7332 were observed in the V band, as a part of a project to investigate boxy/peanut shaped bulges in edge-on galaxies (Patsis & Xilouris 2006). An overview

Galaxy	B (sec)	V (sec)	R (sec)
NGC 0128	0	5400	0
NGC 5023	3600	1800	1800
NGC 5529	3600	1800	1800
NGC 5907	12600	5400	3600
NGC 7332	0	7200	0
UGC 2048	9000	5400	3600

Table 2.1: Overview of the observed galaxies by the 1.3m telescope on Skinakas.

of the exposure times for each galaxy and filter is listed in table 2.1

Bias, flat fields and standard stars

Bias frames   The bias frames are simple zero second exposures with a closed shutter. In other words: the CCD is just read out without any external light shed upon the chip. A CCD chip converts the gathered electrons to a digital signal through multiplication of a constant factor, which is in this case just 1 e$^-$/ADU. To make sure the conversion does not create negative numbers, a small voltage is applied to the CCD. This voltage is called the "bias" and has to be subtracted from all images during the data reduction phase. Usually, a bias frame is a flat, uniform array of pixels with only a small rms: the readout noise. In uncooled cameras, additional noise may occur due to the thermal excitation of electrons. This so called dark current noise is, however negligible for most modern cameras. Sometimes, a small gradient can occur towards the side where the frames are read out. This is caused by the on-chip amplifier and favours the subtraction of the bias frame rather than its median value during data reduction. Bias frames are usually taken during the day, or at the beginning and end of the night, when the sky is too bright to execute any other kind of observations.

Sky flat fields   Flat fields are short exposures of a uniform light source, mostly the zenith sky at twilight or near dawn. It is only during a small time window (up to 15 minutes) that the zenith sky qualifies as a uniform light source. Flat fields are taken for each band used that night. For each band at least five flat-fields are desired, each with around 30000 ADU counts, which is half the full well capacity of the CCD chip. For this observing run, only twilight flats were taken. There was no need of additional morning flats because the twilight flats had good quality. Figure 2.3 shows an example of a flat field frame in the R band. Flat fields are probably the most important calibration tools for imaging and photometry. It cancels out the pixel to pixel variations inherent to the
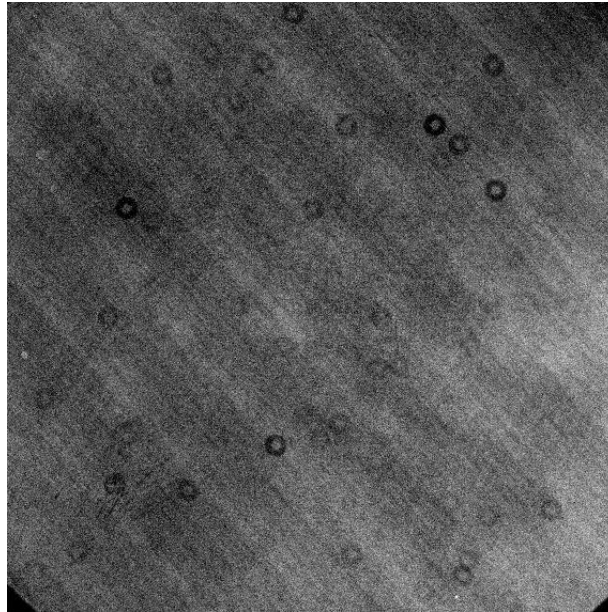
Figure 2.3: An R band flat field of the Skinakas observing run.

CCD chip and corrects for dust and scratches on the camera, which can severely scatter the incoming light.

After bias and flat fielding, the dome slit has to be synchronised so that the telescope looks right through it. This was done by pointing the telescope exactly south and aligning the dome slit. Throughout the night the dome will now follow the telescope's movements. The last step for the instrumental setup is fine-tuning of the secondary mirror. This focussing is done by finding a focal star, usually Vega and adjusting the secondary mirror to obtain minimum Full Width at Half Maximum (FWHM). Everything is now calibrated and set up, the actual observations can start.

Photometric standard stars Photometric standard stars are non-variable stars or stellar fields which have been accurately observed multiple times. This way their relative magnitudes are known in detail and it is possible to create a correct magnitude scale. Standard star fields are found in several catalogs, depending on the part of the sky and the used filters. In this case, the Landolt catalog (Landolt 1992) was used to select the stellar fields for the BVR filters. Standard stars are used to calibrate the observed galaxies to the standard magnitude scale and eliminate the effects of Earth's atmosphere, which change from night to night and even within each night. This is also the reason why the observation of standards has to be done each night and preferably several times during the night. Upon choosing the stellar fields, it was carefully checked that the standard stars were observed at airmasses varying from 1 to 2, which was the region in which the galaxies were observed. Airmass χ is defined by the secant
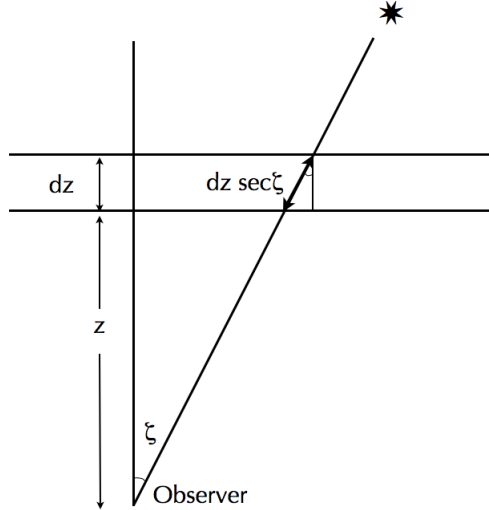
Figure 2.4: Starlight passing through a thin atmosphere layer dz under an angle ζ. Integration over all atmosphere layers yields the airmass $\chi = sec\zeta$.

of the angle ζ between the line of sight and zenith position (see figure 2.4) and can be calculated from the standard coordinate system:

$$\chi = sec\,\zeta = (\sin\phi\,\sin\delta + \cos\phi\,\cos\delta\,\cos H)^{-1}, \tag{2.1}$$

where ϕ is the observer's longitude, δ the declination of the source and H its hour angle.

By choosing airmasses between 1 and 2, it is possible to interpolate the effects of the atmosphere to all airmasses in that region. Eventually, the atmospheric effects can be extrapolated to airmass zero, which is how the star would look like from space, see figure 2.5. The several standard star fields resulted in close to thirty stars in each band. Exposure times for the star fields varied from 60 to 180 seconds, depending of the brightness of the stars and the wavelength band (B band imaging typically requires longer exposure time than V band).

2.2	Data reduction

Once the observations are done, the reduction of the gathered data is the next step towards scientific imaging. The goal of data reduction is to remove instrumental and physical effects which hinder accurate imaging and photometry, and to increase the signal-to-noise ratio of the images. The signal-to-noise ratio (SNR) is, together with the astronomical seeing, a widely used tool to indicate the quality of the images. Theoreti-
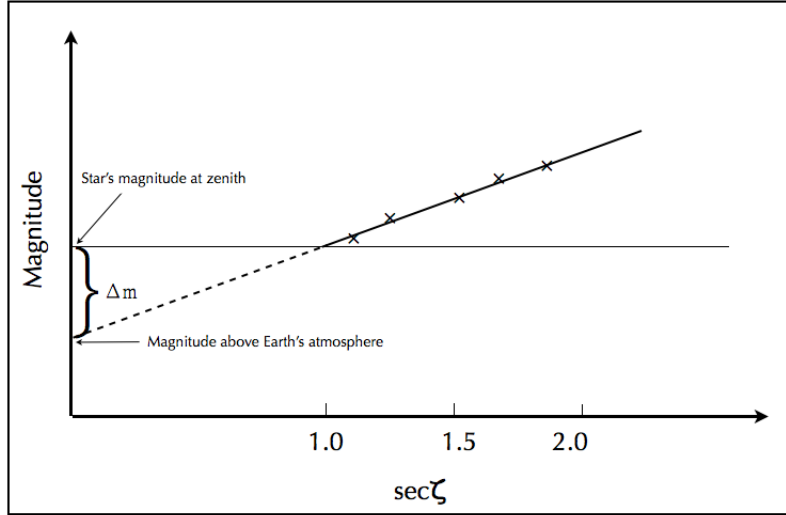
Figure 2.5: Extrapolation towards airmass $\chi = sec\zeta = 0$: above Earth's atmosphere.

cally, the SNR can be calculated using the CCD equation:

$$SNR = \frac{N_*}{\sqrt{N_* + n_{pix}(N_S + N_D + N_R^2)}},$$
(2.2)

where N_* is the measured signal in counts per second, n_{pix} the number of pixels of the region for which the SNR will be determined and N_S, N_D and N_R the number of photons per pixel of the sky background, the number of dark current electrons per pixel and the number of electrons per pixel from the readout noise. Usually the contribution of the dark current is negligible and the sky background is corrected for after a good data reduction.

Scientific data reduction of optical and near-infrared data consists of several steps, for which different routines and software are used. First of all, there is imaging: removing instrumental effects and cleaning the images. Next there is the photometric calibration, based on the standard stars, to convert the magnitudes of stars and galaxies to the standard magnitude scale. The third step consists of combining or co-adding single exposures from a single night to increase the SNR. Sometimes also images from different nights have to be combined to further increase the SNR. A correct calibration is of vital importance here. Last step is to fine-tune the astrometric information, which comes down to adding world coordinate system (WCS) information to project the images on their correct position on the sky. This step is sometimes performed before the co-addition to simplify the aligning. Three different software packages were used, each have their specific strengths or user-friendly approach for the different tasks:

ESO-MIDAS or European Southern Observatory - Munich Image Data Analysis Sys-

tem (version 11FEB, ESO (2012)) is a very flexible set of routines for analysing scientific data systems. It is easy to write additional scripts to execute case specific operations. ESO-MIDAS scripts were written for this thesis, to facilitate the imaging, co-adding and application of the calibration. All these steps require arithmetic calculations of data arrays, for which ESO-MIDAS is a fast and reliable tool.

IRAF or Image Reduction and Analysis Facility (version 2.14 NOAO (2012)) is a software package written by the National Optical Astronomy Observatory (NOAO) and provides excellent routines for photometric measurements. IRAF was used to investigate the standard star fields and make the flux calibration.

GAIA or Graphical Astronomy and Image Analysis (version 4 Draper et al. (2009)) is a display and analysis tool by the Joint Astronomy Centre. It is a user friendly program, suitable for accurate astrometric calibration.

The observations of the galaxies were done during four consecutive nights and in three different wavelength bands. During the data reduction, each observing band will be treated separately and each night will be treated separately. Final combination of images from different nights will only be done at the end of the road.

2.2.1 Imaging

Imaging is all about removing as many instrumental and physical effects from the science objects. A first step is to make a master bias and flat field frame. This is done by combining all bias frames which are taken during the night using a median method. An ESO-MIDAS routine takes the median of each set of corresponding pixels of the bias frames. This way most statistical fluctuations are cancelled out and a flat and uniform master bias is created. The same median method is used to create the master flat field, only, the master bias frame was subtracted from each separate flat field frame before combination. Because of the high count rate of flat fields, typically around 30000 counts/pixel, the master flat is normalized to one. Without this normalization, science frames would be left with very low count rates, making the analysis and photometric calibration less workable. The pixel distribution of a good flat field should be Gaussian and centred around 1, see figure 2.6. A normalized master flat only holds the pixel variations, but will not affect the intensity of science frames, see figure 2.7. All object frames, including standard star frames, can now be bias subtracted and divided by the master flat.

Long exposure images suffer from a non-negligible number of cosmic ray impacts. Cosmic rays are very energetic particles that hit the CCD detector and leave very clear signatures, see figure 2.8. ESO-MIDAS contains an efficient routine to remove the cosmic rays, based on the background level and some threshold value to recognize a set
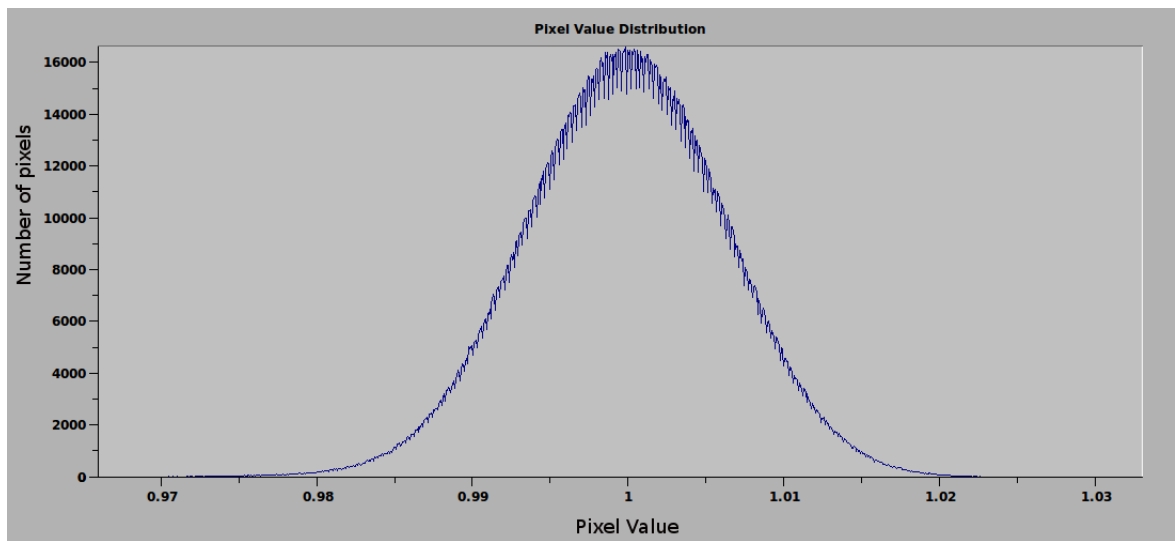
Figure 2.6: Pixel distribution of a V band master flat. The distribution closely resembles a Gaussian curve.
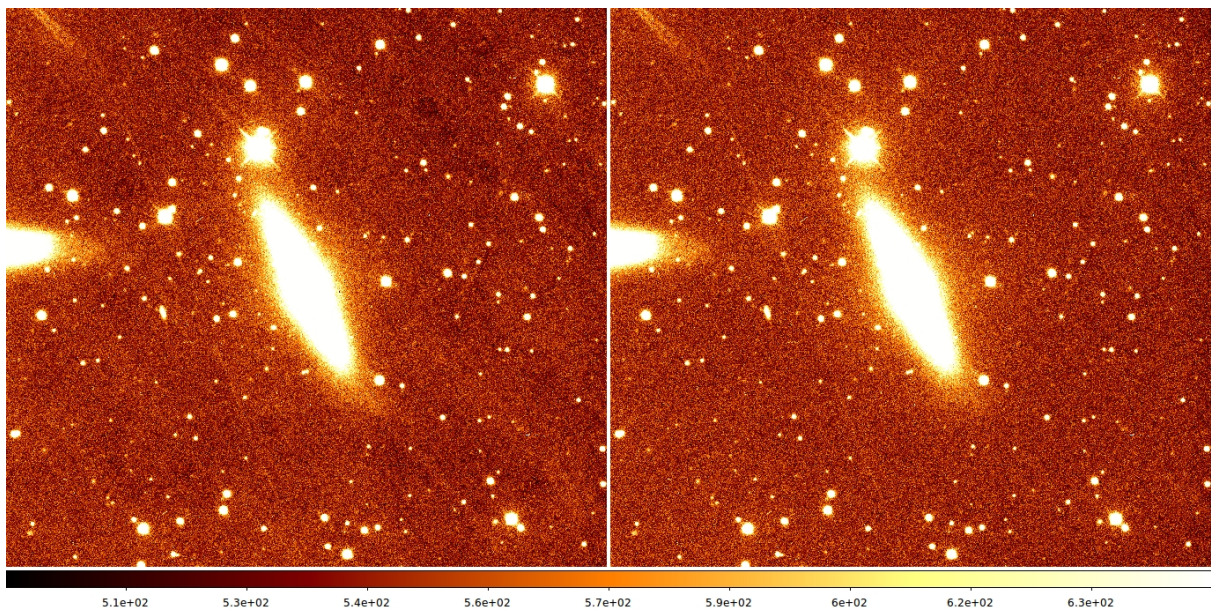

Figure 2.7: V band image of NGC 7332 without (left) and with (right) flat field correction. The difference is visible in the background structures and the doughnut shapes, caused by diffraction on dust grains.
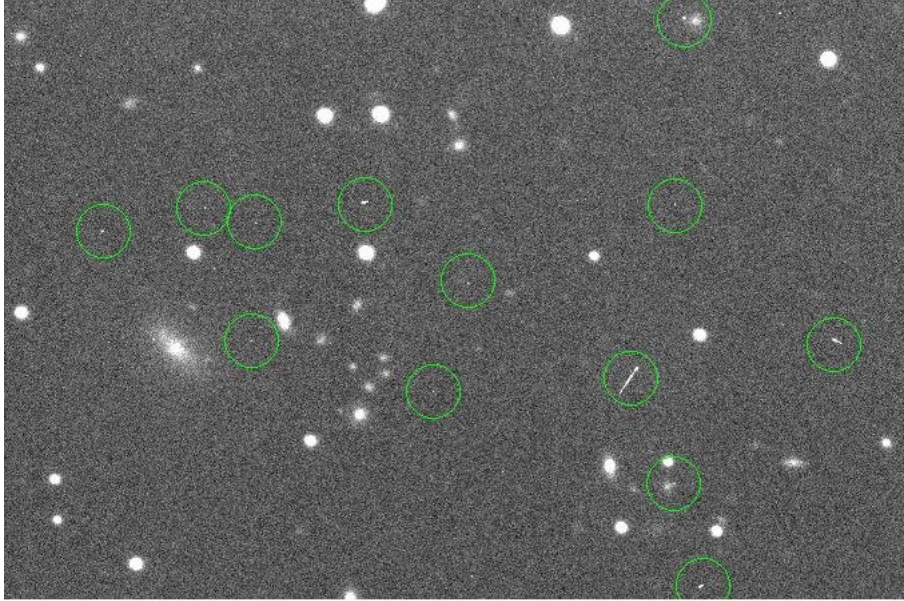
Figure 2.8: Cosmic rays in an R band image, after 1800 seconds of exposure.

of pixels as a cosmic ray event. The next step is to subtract the sky background from the images. The sky background is a combination of intrinsic sky brightness and unresolved sources and should be brought back to around zero. To estimate the sky, several source-free regions in the field of view were taken and their mode was calculated and subtracted from the frame. As a final step in the imaging process, all images were divided by their respective exposure times to set the pixel units to counts per second.

A strange feature was spotted on some of the R band images, see figure 2.9. Next to each strong stellar source, a weak signal could be distinguished at a constant offset to the main stellar peak. Only R band images from the first night were affected, ruling out detector related defects. The secondary source may be explained by a telescope jump during the exposure. Because the signal is weak and only R band is affected (stars are brighter in R compared to B or V), it looks like the jump took place at the very beginning or at the end of the exposure. In any case, the right part of figure 2.9 shows that the signal is negligible and probably will not affect the flux of the galaxy itself.

2.2.2 Photometry

The cleaned images were calibrated using IRAF routines. Optical photometry is based on the formula

$$m_{cat} = ZP + m_{obs} + a\chi, \tag{2.3}$$

18

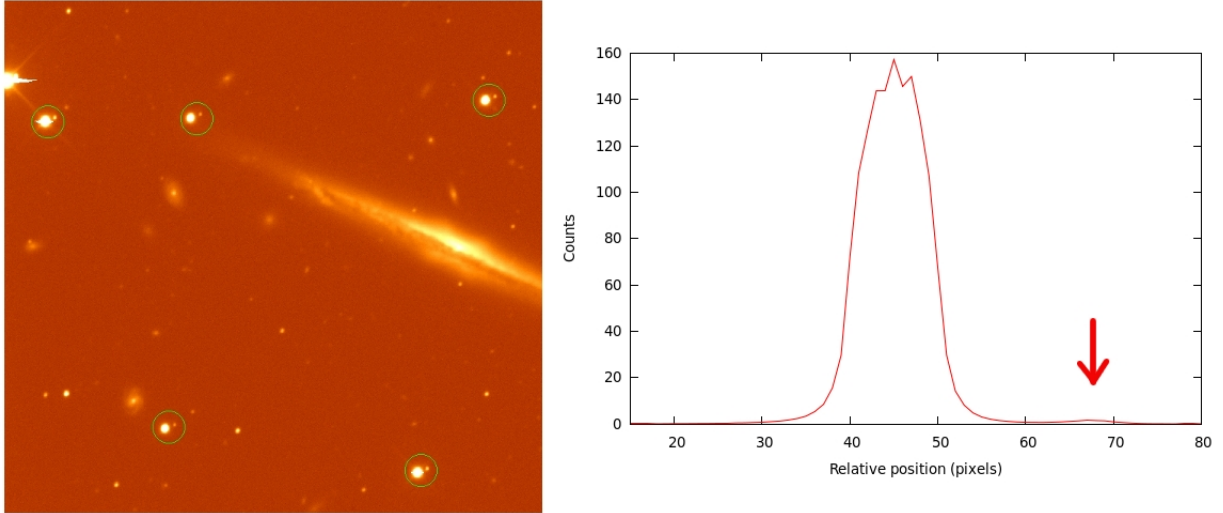**Figure 2.9:** Left: R band image of NGC 5529. Weak secondary sources are visible near all bright stars, with the same offset. Right: projection of one of the bright stars. A very weak signal is present next to the main stellar peak.

Night	Star Fields	# Standard Stars
1	SA92, SA107, SA110, PG1633+099, Mark A	30
2	SA92, SA107, SA110, PG1633+099, Mark A	35
3	SA92, SA107, SA110, PG1633+099, Mark A	27
4	SA92, SA110, PG1633+099, Mark A	31

Table 2.2: Observed Standard Star fields from A. Landolt's catalog.

where m_{cat} and m_{obs} are the catalogued and observed magnitudes of the object and χ is the airmass at which the object was observed. The zero point ZP and extinction a are free parameters that hold the effects of the atmosphere (scattering, extinction, turbulence, humidity,..) and the instrumental setup. These two parameters will have to be determined by using the measured standard stars, for which all other terms χ, m_{cat} and m_{obs} are known. Each night a number of standard star fields were observed. Table 2.2 lists the number of calibration stars that were used each night.

In each star field the standard stars were identified. Their total flux was determined by a technique called aperture photometry. Aperture photometry simply sums all pixel values within a certain annulus (usually four times the FWHM) of the selected source and then subtracts the local background, see figure 2.10. A small buffer zone, called the no man's land separates both regions to avoid mix-up. IRAF automatically locates the center of the star by fitting a two-dimensional Gaussian to the point spread function. The local background is estimated by taking the average pixel values of the region between the no man's land and the sky background annulus. Finally, the measured
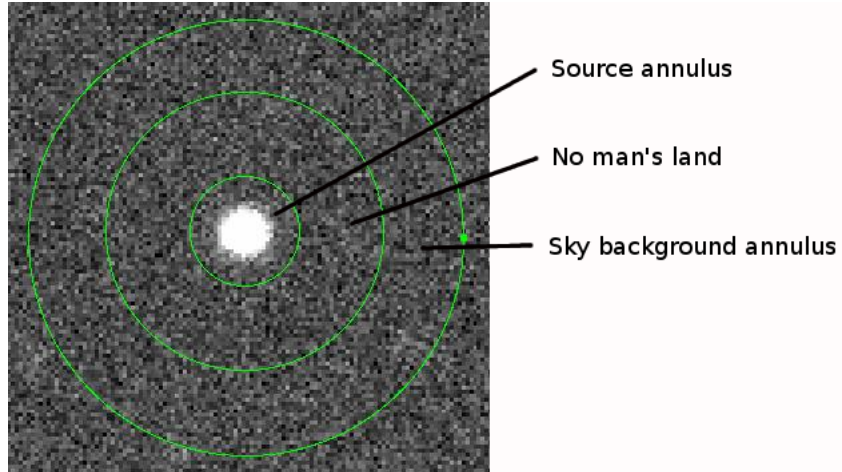
Figure 2.10: Different areas of the annulus used in aperture photometry.

flux was corrected for the exposure time, readout noise and gain and converted to a magnitude scale. This yielded N equations of the form

$$m_{cat,i} = ZP + m_{obs,i} + a \cdot \chi_i, \tag{2.4}$$

where $i = 1, ...N$, to be fitted. A least-squares fit was performed to find the zero points and extinction parameters from the observed and catalogued magnitudes of the standard stars. The results of these fits for each observing band are displayed in table 2.3.

Once the calibration through standard stars is done, it can be applied to the images containing the objects of interest. The calibration equation can now be reversed to obtain m_{cat} for the galaxy images. The subscript 'cat' now has the meaning of true magnitude rather that catalogued magnitude. MIDAS was used to perform the calculation. Note that the image pixels have the unit counts per second, which are linear units. These linear flux units have to be converted in logarithmic units through the standard formula for magnitudes: $m = -2.5 log(F/F_0)$. This can be rewritten:

$$-2.5 \cdot \log(F_{\text{Calibrated Image}}) = -2.5 \cdot \log(F_{\text{Observed Image}}) - ZP - a \cdot \chi. \tag{2.5}$$

The images are now calibrated for each night separately. This means all instrumental and atmospheric influences, which could vary from night to night, are corrected. The last step is combining the measurements from all the nights into final images.

Band	ZP (mag)	Extinction a	fit rms
Night 1			
B	2.027	0.410	0.075
V	2.082	0.234	0.032
R	2.197	0.128	0.030
Night 2			
B	2.096	0.494	0.112
V	2.069	0.303	0.039
R	2.049	0.272	0.028
Night 3			
B	2.209	0.383	0.095
V	2.149	0.248	0.029
R	2.171	0.195	0.023
Night 4			
B	1.971	0.563	0.052
V	2.205	0.239	0.033
R	2.261	0.163	0.032

Table 2.3: Zero points and extinction values form least squares fits to the standard star magnitudes.
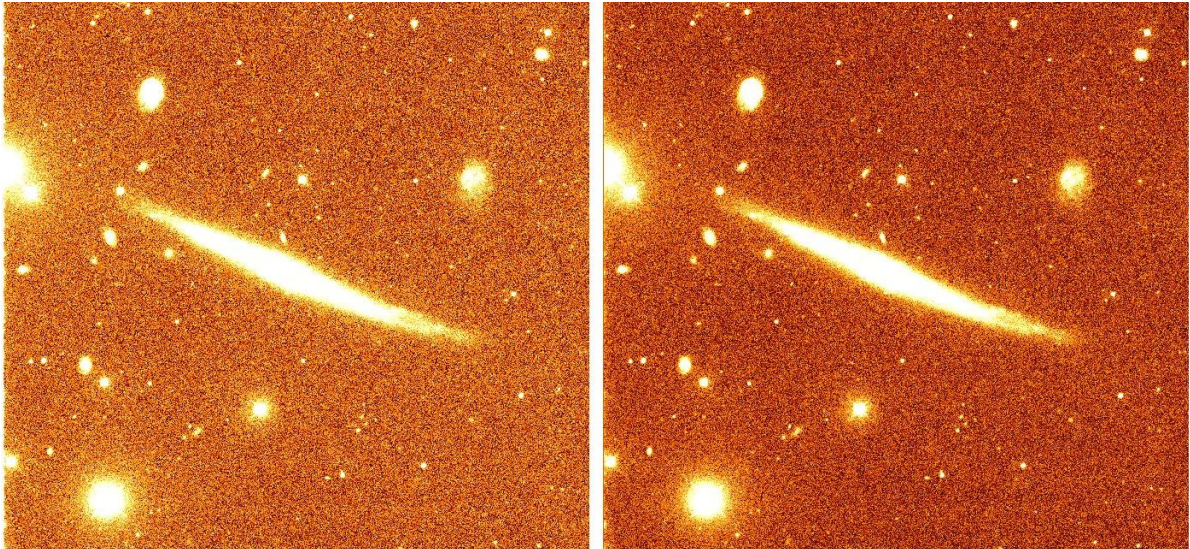

Figure 2.11: Comparison of a single exposure (left) and a combination of two such exposures (right) of NGC 5529. Scale and contrast levels were matched to point out the differences: the combined image has a higher SNR and so shows more and brighter sources on a darker background.

2.2.3   Co-addition

Multiple exposures of the same object in the same observing band can be co-added to produce deeper imaging, see figure 2.11. In fact, co-adding increases both signal and noise in the images, but the overall SNR has a net increase. Before combining the images, they need to be perfectly aligned in the used pixel or world coordinate system. Alignment was done in a few simple steps within ESO-MIDAS. The first image is called the reference image. All other images will be shifted, stretched and rotated to exactly match the coordinate system of this image. In the reference image, a set of stars (usually seven or more) is selected. Preferred stars for this selection are reasonably bright stars with a narrow PSF, for which the center can be accurately determined. To each star, a 2-D Gaussian profile was fitted and the center of the Gaussian was stored. This will make a set of reference points to align the images. The same stars were selected in the other images and their center was also calculated through the 2-D Gaussian fitting method. The next step is to shift, rotate and stretch each image so that their transformed points match the reference points. This method usually reaches accuracies ranging from half a pixel to one tenth of a pixel, depending on seeing and the number of available reference stars. For the Skinakas dataset, alignment up to one tenth of a pixel could be achieved. The images can now be co-added. Depending on the number of images to combine, different techniques are favoured. Usually the median technique, which takes the median for all sets of corresponding pixels, works very well for a large number of images. However, when co-adding 2 or 3 images, it is better to take the average for all sets of corresponding pixels.

2.2.4   Astrometry

For further purposes, it is always useful to add correct astrometric information to the images. This can be done in various ways as there are a lot of different coordinate systems and projections (Greisen & Calabretta 2002). A tangential or gnomic projection of right ascension and declination is one of the most used combinations and was therefore used here. The GAIA program provides a user-friendly interface to perform astrometric calibration: a set of stars in the image was selected and their pixel coordinates were accurately determined by fitting a 2-D Gaussian to the point spread function. Round, non-overexposed, not too bright stars with low proper motion are preferred as a astrometric calibration set. The RA and DEC info of those same stars were then retrieved from the PPMXL catalog of positions and proper motions (Roeser et al. 2010). GAIA possesses a fitting routine to match both sets of stars and reach astrometric accuracies of half an arcsecond by doing so. Figure 2.12 shows the matching of the PPMXL catalog with the combined R band image of NGC 5023.
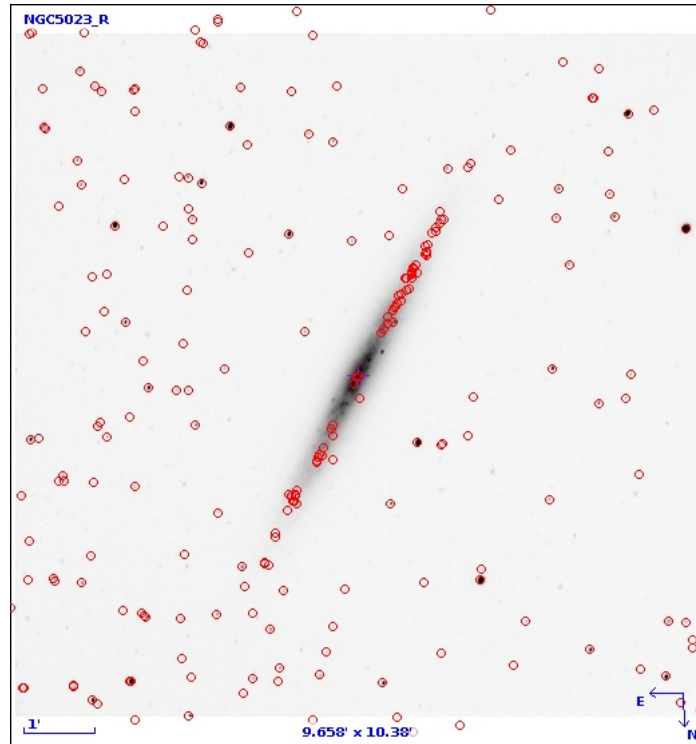
Figure 2.12: R band image of NGC 5023 overlaid with sources of the PPMXL catalog.

A fully detailed overview of the observed and reduced data from the Skinakas run can be found in appendix A.

Observing run on the Telescope Natzonale Galileo

3

*If we knew what we were doing, it
wouldn't be called research, would it?*

Albert Einstein

3.1 HEROES/NHEMESES observations with the TNG

As a second part in completing the HEROES and NHEMESES datasets, observing time
was granted for the Telescope Natzonale Galileo (TNG, ENO (2012)), a 3.58m telescope
of the Roque de Los Muchachos Observatory on La Palma. In total 3 hours in V band
and 21 hours in K band were granted for the program, which was fully executed in
service mode during August and December of 2011 with an average seeing of 1.34
arcseconds. Table 3.1 gives an overview of the observed objects.

3.1.1 Instrumental setup

Roque de Los Muchachos is one of the worlds best astronomical sites thanks to the
combination of high altitude (2396m) with a dry climate. With a V band sky brightness
of 21.9 mag (Benn & Ellison 1998) it is also one of the darkest places of the northern
hemisphere. The observatory is operated by the Instituto de Astrofisíca de Canarias
(IAC) and is part of the European northern Observatory (ENO).

The TNG is a Ritchey-Chrétien telescope with altitude-azimuth mounting and a focal
length of 38.5m. An additional tertiary mirror feeds two Nasmyth foci who pass the
light on to different detectors attached to the system. The telescope is equipped with
an adaptive optics system, to perform high speed corrections to the secondary and
tertiary mirrors. Optical and near-infrared observations were executed with different,
specialized instruments.

Galaxy	RA (J2000)	DEC (J2000)	Project	V (sec)	K (sec)
UGC 2048	02 : 34 : 20.1	+32 : 30 : 20.0	HEROES	750	2880
IC 2233	08 : 13 : 58.9	+45 : 44 : 32.0	NHEMESES	750	2875
NGC 4144	12 : 09 : 58.6	+46 : 27 : 26.0	NHEMESES	750	3105
NGC 4183	12 : 13 : 16.9	+43 : 41 : 55.0	NHEMESES	750	3105
NGC 4244	12 : 17 : 29.6	+37 : 48 : 26.0	NHEMESES	750	3105
UGC 7321	12 : 17 : 34.0	+22 : 32 : 25.0	NHEMESES	750	3105
NGC 4460	12 : 28 : 45.5	+44 : 51 : 51.0	NHEMESES	750	3105
NGC 5023	13 : 12 : 12.6	+44 : 02 : 28.0	NHEMESES	750	2875
NGC 5907	15 : 15 : 53.8	+56 : 19 : 44.0	HEROES	750	3105
Additional: NGC 5907, J band: 2025 sec					

Table 3.1: Overview of the TNG observations of HEROES and NHEMESES galaxies.

Figure 3.1: The TNG telescope on Roque de los Muchachos, La Palma

DOLORES

The Device Optimized for the LOw RESolution (DOLORES) is mounted at the Nasmyth B focus and suitable for optical imaging and spectroscopy. It holds a back illuminated E2V CCD camera with a resolution of 2048 × 2048 pixels. Each pixel is 13.5 × 13.5 μm wide, yielding a field of view of 8.6 × 8.6 arcminutes. The CCD is linear within 1% in its dynamic range. V band quantum efficiency is around 93% and saturation around 65500 ADU. Cooling kept dark current at a negligible level, yielding a readout noise of 9 e⁻ and a gain of 0.97 e⁻/ADU.

NICS

The Near Infrared Camera Spectrometer (NICS), mounted at the Nasmyth A focus, was used for the K band observations. The detector, a Rockwell 1024 × 1024 HgCdTe Hawaii array, has a strongly wavelength-dependent quantum efficiency with a K band value around 60% and is linear up to 20000 ADU. Readout noise is around 24 electrons and gain around 8 e⁻/ADU. The CCD chip is simultaneously read out by four different electronic channels. Any signal in one area of the chip creates negative ghost signals in the other areas due to coupling of these readout channels. This effect is called crosstalking, see figure 3.2, and requires specialized routines to correct for. Near-infrared imaging also suffers from other instrumental defects compared to optical imaging such as non uniform bias frames, memory effects and fringes. Fortunately, specialized data reduction techniques can correct these defaults.

The Large Field (LF) camera was chosen to image the large galaxies. This camera uses a combination of lenses to collimate the light beam to a field of view of 4.2 × 4.2 arcmin. All this limits K band exposures to a maximum of 25 seconds on the LF camera. Processing software then creates a mean image from these multiple short exposures. Additionally there is need for a good sky background estimation to rule out remaining instrumental an physical effects. Therefore, NIR imaging constantly switches between series of "on" source and "off" source (sky) exposures, starting and ending with an "on".

3.2	Data reduction

3.2.1 V band: data and problems

The observations were all done in service mode, which means the requesting party has less control over the way the observations are executed. This brings forth some
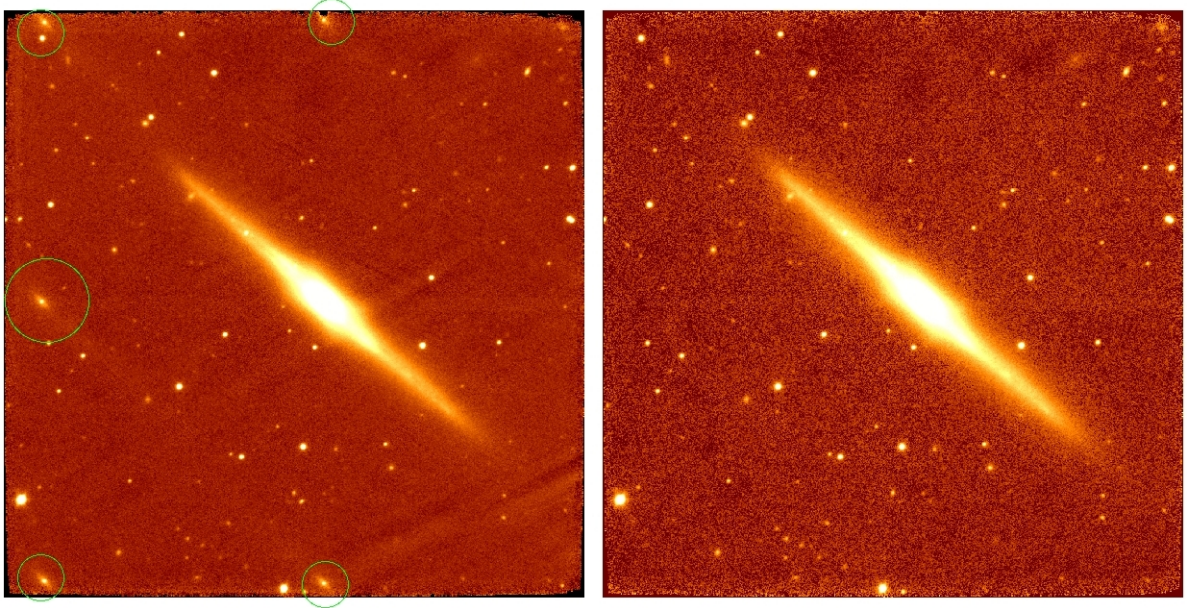
Figure 3.2: Left: K band image of UGC 2048 without cross-talking correction. Several ghost signals of the galaxy's nucleus are visible. Right: the same image, now with the SNAP correction for cross-talking enabled.

problems during the reduction of the data, as will be clear in this section. First of all, the TNG telescope works with monthly master flats. Each month, various sets of flat fields are taken and combined in a median master flat field, which is then released for the public to use. These public releases were sometimes delayed, which subsequently delayed the data reduction of this set. It is likely that nightly variations in the atmosphere can cause minor deviations from the master flat, making them less fit to remove all physical effects. The long period in which all observations were made, makes the data set more sensitive for seasonal effects which also cannot be completely removed by the monthly master flats. Fortunately, this spreading of observations and the poor availability of master flats will not have a large influence on the resulting images because other, instrumental and random noise will be dominant. A second problem is the storage of the CCD information. As usual, this was done using the standard FITS format (Pence et al. 2010). Sometimes WCS information was automatically stored in the FITS files too. However, careful examination showed that this WCS information was just plain wrong. For example the V band image of NGC 4183 had RA = 211.8° and DEC = $-29.2°$ in its lower left column, where the upper right column had RA = 30.3° , DEC = 24.6°. This is fully inconsistent with the size of the galaxy ($3.9' \times 1.2'$), the visible sky on La Palma and the available $4.2' \times 4.2'$ field of view. This was the case for many images, for which WCS information had to be removed and correctly readded later on, see section 3.2.4. A third, more specific problem occurred in the imaging of UGC 2048. The bright star HD 15896 is located 4.5 arcminutes from the center of UGC
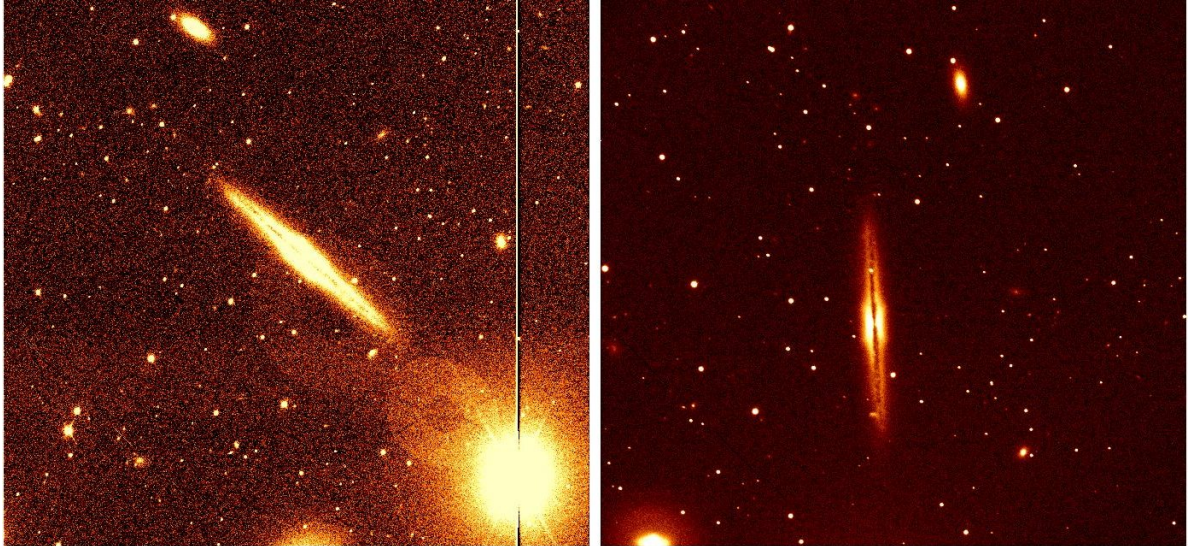
Figure 3.3: Effects of the bright star HD 15896 near NGC 2048. Left: the star lies in the field of view, rendering the images unusable. Right: the star lies just outside the field of view.

2048 and easily overexposes after only a few seconds of observations. This was not accounted for when observing the galaxy, resulting in severe blooming and reflection effects which make the images unusable for scientific purposes. The galaxy was reobserved two months later, this time without the bright star in the field of view, see figure 3.3.

Apart from these issues, imaging was done using the same techniques as explained in section 2.2.1. All frames were bias subtracted and divided with the master flat which corresponded best to their observed period. Cosmic rays were removed using the ESO-MIDAS routine and the frames were divided by their exposure time. Sky background levels were estimated by taking the mode of the pixel values in regions without visible sources around the galaxy. This single value was subtracted from all the pixels in the frame, bringing the average background level down to zero. Most of the galaxies fit nicely in the field of view of the telescope and could be aligned using the method outlined in section 2.2.3. The largest galaxies, however, were too big to fit the field of view. An alternative approach, called mosaicking, was used to combine the frames of NGC 4244 and NGC 5907. This technique is described in section 3.2.3.

3.2.2   K band: SNAP pipeline

K band data reduction of observations with the TNG quickly becomes complicated because all the instrumental effects that influence the imaging. The processing of such NIR data thus is sensitive to errors from non-experienced TNG users. To overcome these perils, an automated pipeline program was developed by Filippo Mannucci
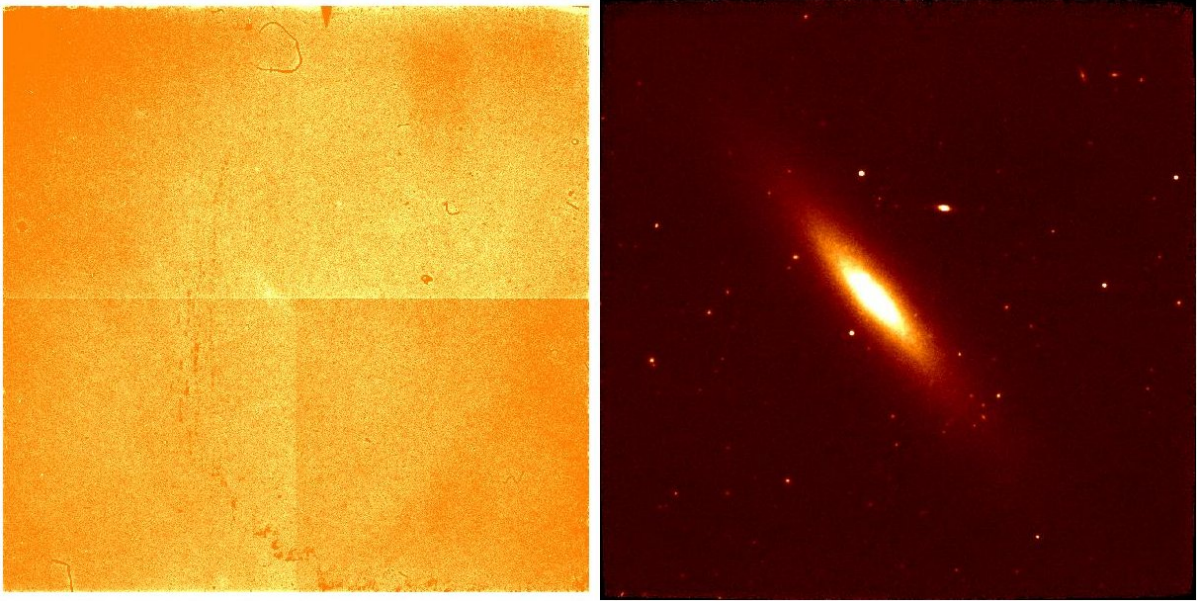
Figure 3.4: Left: one of the 12 'on' exposures of NGC 4460, the light from the galaxy is only barely visible in the center and many artefacts are visible on the image. Right: SNAP reduced combination of the 12 'on' and 11 'off' exposures of the same galaxy.

(IRA-CNR). SNAP (Mannucci 2012) is the Speedy Near-IR data Automatic reduction Pipeline and accurately reduced raw NIR data to clean and co-added science frames. The program uses existing software routines such as IRAF and SExtractor (Bertin & Arnouts 1996) to process the data. Apart from the standard data reduction steps, SNAP also corrects for cross-talking, distortions by the TNG optics and defines an optimum sky level for all images. Figure 3.4 shows the difference between raw K band observations and the SNAP reduced science image.

Only three galaxies were small enough to fit the field of view of the NICS instrument: IC 2233, UGC 2048 and NGC 4460. NGC 5907 was accidentally observed in the J band too, but in a single scanning exposure. The other galaxies had to be combined using mosaicking techniques which are explained below.

3.2.3 Mosaics and MONTAGE

Most of the galaxies are too large to be observed in one NICS field of view. The same applies to the V band observations of NGC 4244 and NGC 5907. These galaxies therefore had to be observed in two or more parts to cover their full extend. Separate images have to be combined into a single larger image, a technique called mosaicking. The Montage Astronomical Image Mosaicking Engine (Jacob et al. 2010) was used to complete the puzzle. Montage requires clean FITS-files with accurate astrometric informations. Astrometric calibration for all images was thus applied before the mosaicking.
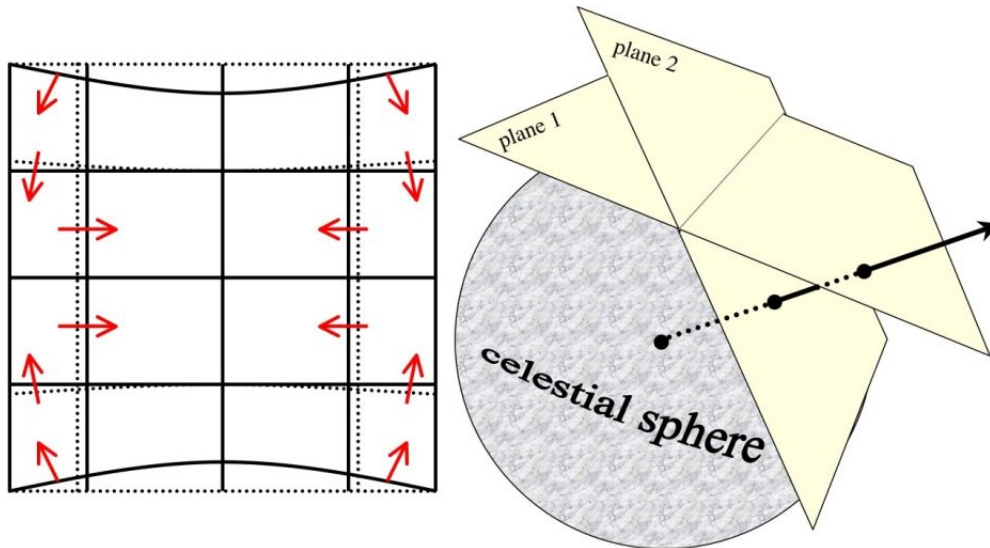
Figure 3.5: Left: exaggerated distortions of a gnomic (TAN) projection. The red arrows indicate the direction of the distortion. Right: plane-to-plane approach to reproject gnomic projections. Two separate images are placed on their respective planes so that a single line can connect the center of the celestial sphere and the two matching pixels for one particular coordinate.

GAIA, see section 2.2.4, was used to achieve accuracies between 0.8 and 0.2 arcseconds. The first step in mosaicking is to reproject all images to the same, undistorted coordinate system. Note that GAIA writes WCS information based on a gnomic projection (TAN), which has its distortions (see figure 3.5, left). An easy way to reproject gnomic projections is the plane-to-plane approach, which is based on a library from Makovoz & Khan (2005), see figure 3.5, right. This approach has the advantage to be computationally less demanding than a general two-step reprojection (which is needed for other types of projections).

A next step is to compare the background levels in the separate images and rectify them to a common background level. This also determined the offsets in flux scales, which is then corrected for too. By using common background and flux levels, the differences between the images is brought to a minimum and the only flux variations will be due to a different SNR. Finally, the reprojected and rectified images are coadded into a final mosaic, see figure 3.6.

NGC 5023

In the specific case of NGC 5023, mosaicking turned out a lot more difficult compared to the other images. Figure 3.7 shows the mosaic of NGC 5023 as the output of the technique outlined above. The image clearly is of very poor quality in the overlapping regions. NGC 5023 was observed during two different nights, each imaging only one
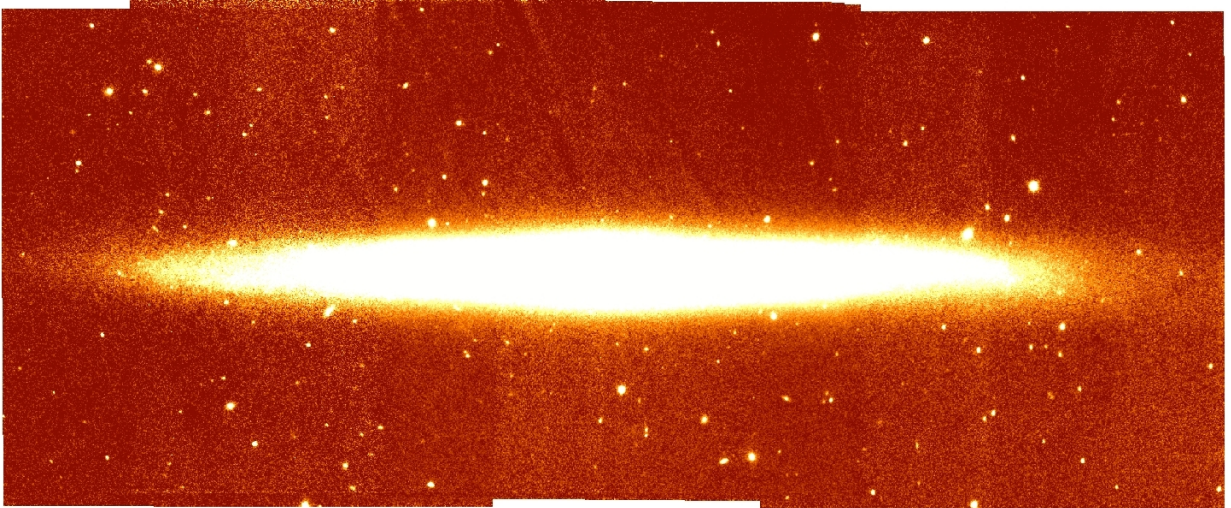
Figure 3.6: Mosaic of NGC 5907: 5 separate images were combined using Montage. The background variations are mainly caused by different SNR's in the overlapping areas.

side of the galaxy. Unfortunately, the only images which overlapped between those two sides were a 15*s* and a 25*s* exposure. This implies very low SNR and a lot of background fluctuations. To make everything even worse, a lot of artifacts and dead pixels are visible right at the centre of the galaxy. The output of the SNAP pipeline could thus not be used to make a mosaic of NGC 5023. However, after careful examination of the images and their correct WCS information, a small overlap area was found. This overlap area was only a few pixels wide and did not hold any stars or artifacts. Both images were cropped to remove the poor quality low exposure area and only keep the small overlap zone and the good quality part. Montage now yielded much better results for the mosaic of NGC 5023, see figure 3.7.

3.2.4   Photometry and astrometry

Mosaicking of multiple images was done using reprojection techniques which needed accurate astrometric information. The resulting mosaics therefore already possess the correct WCS information. Images which were co-added without mosaicking, but with the star-selection approach, still need WCS information. This was added using the GAIA tool, as outlined in section 2.2.4. Once the astrometry was correctly added, only photometric calibrations remain. Unfortunately, it was impossible to use the previous method, see section 2.2.2, because this method is based on photometric standard stars. In some nights, only one set of standard stars was taken, which makes interpolation to other airmasses impossible. During other nights, there were no standard stars at all observed. Consistent calibration through standard stars was not possible for this dataset. Another method to achieve photometric calibration is through catalogs of large sur-
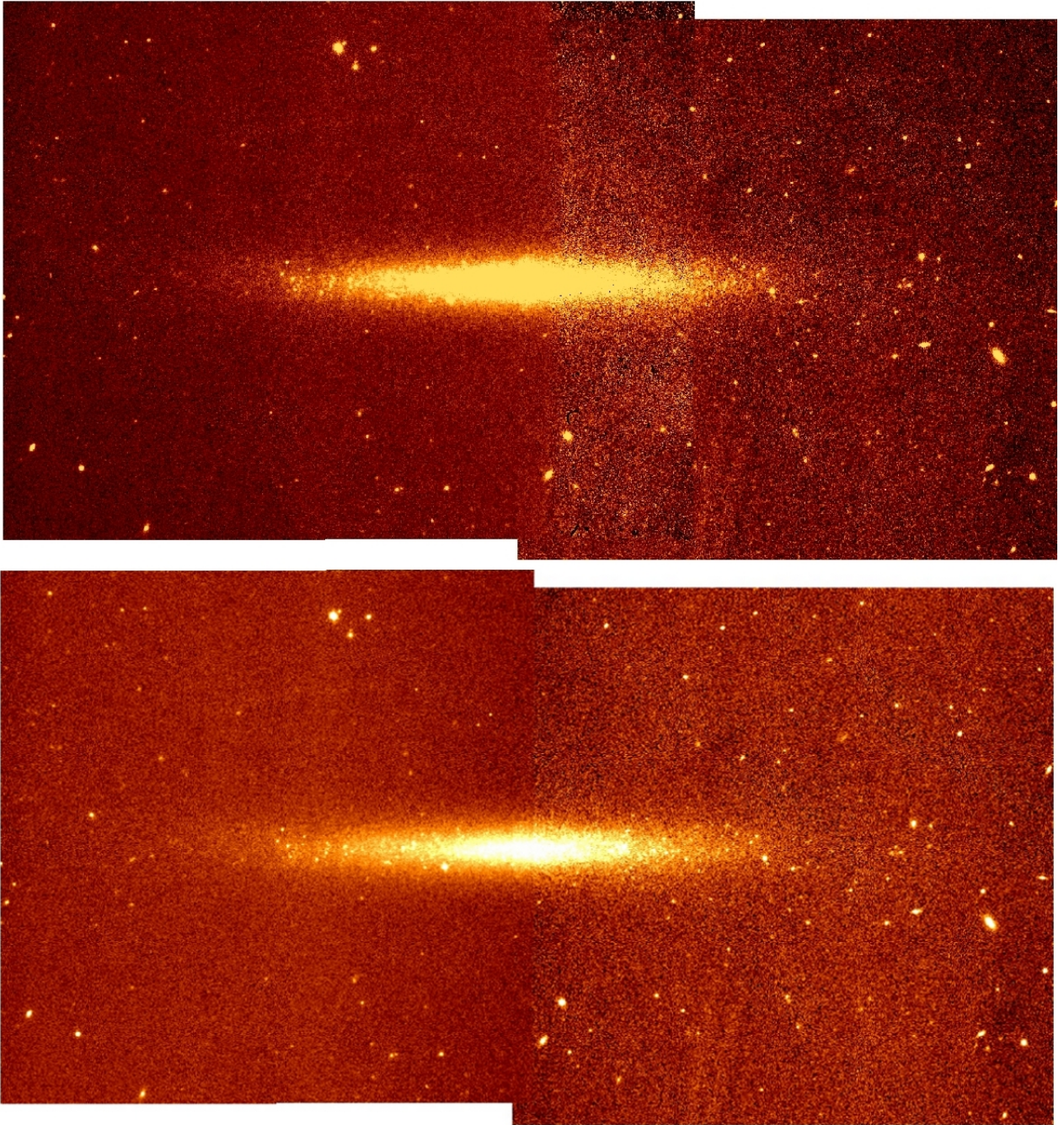
Figure 3.7: Top: mosaic of NGC 5023. The overlapping area in both images was of very poor quality due to the short exposure, which is clearly visible in the resulting image. Bottom: the same galaxy, but now with the bad areas removed before mosaicking.
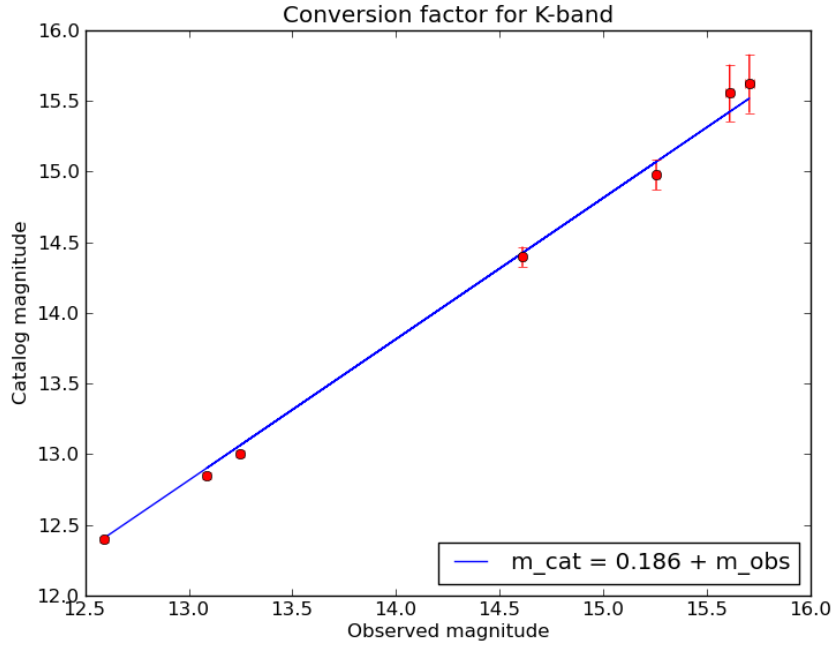
Figure 3.8: Result of the K band photometric calibration of NGC 4183 to the 2MASS catalog. The offset between observed and catalog magnitude scale was 0.186 mag. The rms of this least squares fit was 0.09.

veys. During the years, almost the entire sky has been observed in both optical and NIR bands. Though not so accurate as photometric standard stars, these catalogs are quite well calibrated and a good alternative to standard stars. Measuring the magnitudes of several stars in the observed image field and comparing those with these catalogued values, will show a constant offset in the magnitude scale. When this offset is determined, it is a simple calculation to rescale the observed fluxes to their references in the catalogs. In other words, the airmass dependency of equation 2.3 is not needed here and a simple calibration equation has to be solved:

$$m_{cat} = ZP + m_{obs} \ . \tag{3.1}$$

Figure 3.8 shows the result of a least-squares fit to a set of stars from NGC 4183 with their equivalent magnitudes from the 2MASS catalog. The 2MASS catalog (Skrutskie et al. 2006) was used to calibrate all K and J band images, where all V band images were calibrated to the NOMAD-1 catalog (Zacharias et al. 2004). Table 3.2 lists the solutions of equation 3.1 for the observed galaxies.

A fully detailed overview of the obtained data from the TNG runs can be found in appendix A.

Galaxy	ZP_V	fit rms	ZP_K	fit rms
UGC 2048	-0.343	0.131	5.548	0.071
IC 2233	-0.606	0.238	4.696	0.859
NGC 4144	-0.925	0.305	0.165	0.166
NGC 4183	-0.457	0.348	0.186	0.086
NGC 4244	-0.340	0.417	0.129	0.278
UGC 7321	-0.324	0.360	0.210	0.176
NGC 4460	-0.727	0.428	5.609	0.271
NGC 5023	-0.723	0.263	-0.175	0.123
NGC 5907	-0.318	0.190	0.340	0.085
NGC 5907 J band: $ZP = 5.077$, rms = 0.148				

Table 3.2: V, K and J band zero points for the flux calibration of the TNG dataset. The ZP values are determined to match the NOMAD-1 optical and 2MASS near-infrared catalogues.

Observing run on the William Herschel Telescope

4

How many times must a man look up before he can see the sky?
The answer my friend is blowin' in the wind.

Bob Dylan

4.1 Site and observations

Additional observations for the HEROES and NHEMESES galaxies were executed on the William Herschel Telescope (WHT) on La Palma (ING 2012). This observing run yielded a total of 9 extra hours for the HEROES project and 7 hours for the NHEMESES galaxies with an average seeing of 1.43 arcseconds. Observations took place during 3 moonless nights from the 25th till the 27th of December, 2011. The observed objects are listed in table 4.1.

Galaxy	RA (J2000)	DEC (J2000)	u (s)	g(s)	r (s)	i (s)	z (s)
NGC 891a	02 : 22 : 33.4	+42 : 20 : 47.0	4800	1200	1235	1260	1980
NGC 891b	02 : 22 : 33.4	+42 : 20 : 47.0	4800	1830	1280	1980	1830
UGC 2048	02 : 34 : 20.1	+32 : 30 : 20.0	4800	3600	1500	3600	1740
UGC 4277	08 : 13 : 57.2	+52 : 38 : 54.0	4800	3600	1200	3600	2700
IC 2233	08 : 13 : 58.9	+45 : 44 : 32.0	6000				
NGC 4144	12 : 09 : 58.6	+46 : 27 : 26.0	4800				
NGC 4183	12 : 13 : 16.9	+43 : 41 : 55.0	4800				
NGC 4460	12 : 28 : 45.5	+44 : 51 : 51.0	4800				

Table 4.1: Overview of the observed galaxies by the William Herschel Telescope.

Figure 4.1: View of the William Herschel Telescope on La Palma.

4.1.1 Instrumental setup

The telescope is also located at Roque de los Muchachos on La Palma and can thus benefit the same climate conditions as the TNG, see section 3.1.1. Weather conditions for this observing run were very good with humidity below 15% and maximum wind speeds of 8 kms^{-1}, 23 kms^{-1} and 30 kms^{-1} during the three nights. The WHT is a 4.2 m Cassegrain telescope with altazimuth mounting and a focal length of 10.5 m. It has the possibility to operate with a third mirror and Nasmyth foci just like the TNG, see section 3.1.1. For this particular observing run, the standard Cassegrain setup was used in combination with the ACAM optical imaging instrument. This combination provided a large 8.3 arcmin field of view, or 0.25 arcsec/pixel. The Auxiliary-port CAMera (Benn et al. 2008) is a fairly new focussing instrument suitable for optical and NIR light. ACAM was equipped with Sloan ugriz filters and the AUXCAM detector. AUXCAM was used in slow readout mode and 1×1 binning, yielding a gain factor of 1.16 e^{-}/ADU and readout noise of 3.0 electrons. The chip has 2148×2501 pixels, is linear within 1.5% over its full range and saturates at 65535 electrons. Quantum efficiency is more or less $80 - 90\%$ in the griz bands and much lower, 35% in the u band.

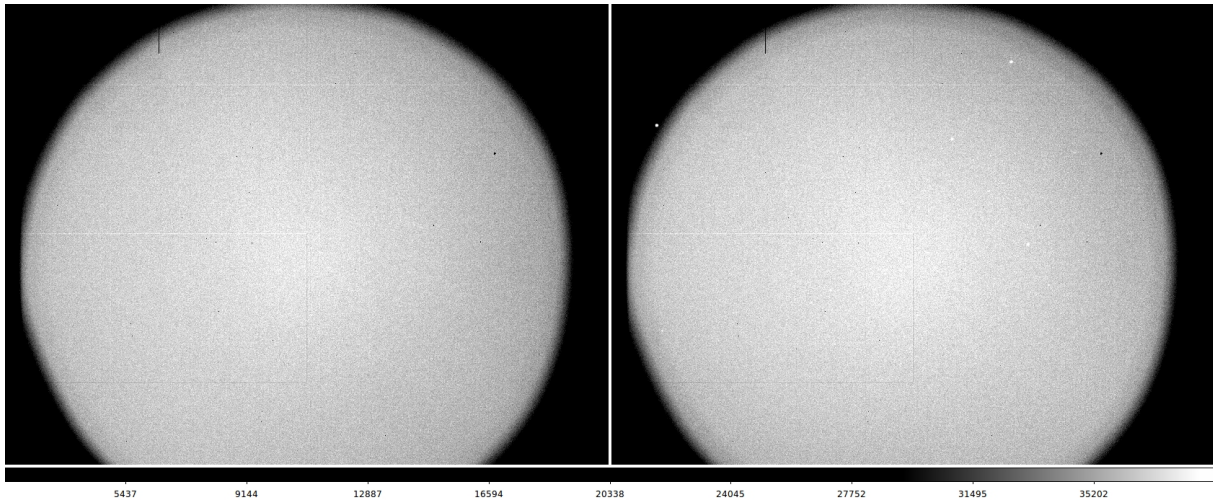|								
5437	9144	12887	16594	20338	24045	27752	31495	35202

Figure 4.2: Left: zoom on a r band dome flat field. Right: zoom on a r band sky flat field, set to the same scale and colour bar. A few stars are clearly visible on the sky flat. There is no other visible difference between sky and dome flats, making dome flat fields a good alternative to sky flats.

4.2   Data reduction

4.2.1   Imaging and aligning

Because of the outstanding quality of the new detectors used for this observing run, data reduction went very fluent and without many problems. Imaging and aligning of the frames was entirely done using ESO-MIDAS routines, see section 2.2.1. Before the observing run, a series of dome flat fields were taken. Dome flats only differ from sky flats in the way the telescope's detector is illuminated. Flat-fielding requires a homogeneous light source which is bright enough to reach half-well capacity within seconds. The twilight or dawn sky are preferred because of their homogeneous character, when taken at the right time. Due to the short time window, the observation of sky flats may sometimes take too long and stars may become visible in the field. This renders the flat field unusable and so an alternative must be available. Dome flats are acquired by pointing the telescope towards a homogeneously illuminated screen on the dome ceiling which then acts as 'sky'. The telescope is then set out of focus to increase homogeneity and short exposures are taken in each filter. They have the advantage that no stars can disturb the imaging and flat fielding can be done over a longer period. Compared to the twilight sky, however, the dome screen is less homogeneous and will result in a less representative flat field, see figure 4.2.

In all three nights, there was not enough time to get star-free sky flats for all the observing bands. The u and g band flats showed no stellar sources in any night and in

this case sky flats could be used. The dome flats taken before the first night had to be used for the r, i and z bands. For each night and each filter, the available flat fields were median combined to a master flat. The same was done for the bias frames. The master bias turned out to be very uniform and so its mode was taken as a single value for the bias. All science images, including standard star fields, were bias subtracted and divided by the normalized master flat. The AUXCAM detector counts a cosmic ray rate of about 130 events per Mpixel per hour, which needed to be removed to avoid errors in the flux determination of stars and the central galaxy. In a last step the sky background was estimated by determining the mode of the source-free regions in the field of view around the galaxy. This value was then subtracted from the image and the resulting frame was divided by its exposure time.

The imaging of the galaxies was always done at airmasses between 1 and 1.5 and no more than 80 minutes passed between the first and last exposure. It is therefore possible to take the average airmass for a galaxy and filter and to assume that the flux variations around this airmass are small. This way all single exposures can be combined at this stage and only the combined image will need to be flux calibrated. Co-adding was done by selecting a set of reference stars and translate the same stars in each frame to the exact same location. Accuracies of half a pixel to one tenth of a pixel could be achieved this way. The aligned images were then combined by taking the median of each set of corresponding pixels an create a final co-added frame with much higher SNR.

4.2.2 Photometry and Astrometry

Each night, sufficient standard stars were taken to perform a decent flux calibration. Only two airmasses were covered, which somehow limits the interpolation to other airmasses, but at each airmass, the frames held three to four photometric standard stars to constrain the flux scale. Well-known stellar fields were used as standard stars, however, this time the Sloan filters were used. The equivalent catalog stars could be found in the SDSS-7 (Abazajian et al. 2009) photometric catalog. However, upon expecting the stellar fluxes in the catalogue, large and inconsistent deviations from their true values popped up. An example is the flux of standard star PG 1047+003A. Table 4.2 lists three catalogued values for this standard star. Smith et al. (2002) made accurate measurements in the u′g′r′i′z′ filters, which could be converted to the normal ugriz system through the equations obtained by Gunn (2001). PG1047+003A is also included in the Landolt catalog (Landolt 1992), (Jester et al. 2005) carefully determined conversion equations to translate Johnson-Cousins UBVRI fluxes to Sloan ugriz fluxes. Finally, the SDSS-7 values were available on the Simbad database. All this somehow

Source	u	g	r	i	z
a	15.207 ± 0.010	13.821 ± 0.032	13.303 ± 0.008	13.091 ± 0.085	13.004 ± 0.008
b	15.572 ± 0.005	14.113 ± 0.005	14.704 ± 0.010	15.764 ± 0.014	13.262 ± 0.006
c	15.150 ± 0.073	13.805 ± 0.025	13.333 ± 0.035	13.153 ± 0.048	13.024 ± 0.043

Table 4.2: Various catalogued values for PG1047+003A. a: Smith et al. converted, b: SDSS-7, c: Landolt converted

Star	u	g	r	i	z
SA92-335	14.202 ± 0.007	12.806 ± 0.002	12.351 ± 0.001	12.243 ± 0.002	12.179 ± 0.003
SA92-339	16.632 ± 0.020	15.728 ± 0.011	15.500 ± 0.010	15.392 ± 0.021	15.327 ± 0.035
SA92-342	12.831 ± 0.003	11.755 ± 0.001	11.540 ± 0.001	11.494 ± 0.002	11.485 ± 0.002
PG942	13.334 ± 0.011	13.708 ± 0.006	14.237 ± 0.005	14.573 ± 0.012	14.904 ± 0.021
PG942-A	$16.645 \pm$ n/a	$15.081 \pm$ n/a	$14.512 \pm$ n/a	$14.278 \pm$ n/a	$14.102 \pm$ n/a
PG942-B	$15.542 \pm$ n/a	$14.303 \pm$ n/a	$13.998 \pm$ n/a	$13.894 \pm$ n/a	$13.835 \pm$ n/a
PG942-C	$16.908 \pm$ n/a	$15.305 \pm$ n/a	$14.794 \pm$ n/a	$14.652 \pm$ n/a	$14.557 \pm$ n/a
PG942-D	$15.221 \pm$ n/a	$13.925 \pm$ n/a	$13.580 \pm$ n/a	$13.468 \pm$ n/a	$13.400 \pm$ n/a
SA101-408	18.239 ± 0.042	15.385 ± 0.036	14.391 ± 0.030	14.042 ± 0.032	13.764 ± 0.037
SA101-410	14.903 ± 0.009	13.854 ± 0.009	13.527 ± 0.009	13.430 ± 0.009	13.376 ± 0.010
SA101-413	15.099 ± 0.014	13.053 ± 0.004	12.280 ± 0.003	12.028 ± 0.005	11.835 ± 0.008
PG1047	12.875 ± 0.007	13.180 ± 0.004	13.706 ± 0.004	14.053 ± 0.009	14.394 ± 0.016
PG1047-A	15.150 ± 0.010	13.805 ± 0.006	13.333 ± 0.005	13.153 ± 0.006	13.024 ± 0.007
PG1047-B	16.389 ± 0.018	15.038 ± 0.007	14.576 ± 0.006	14.438 ± 0.010	14.348 ± 0.015
PG1047-C	13.803 ± 0.012	12.697 ± 0.009	12.308 ± 0.009	12.182 ± 0.010	12.102 ± 0.011

Table 4.3: Overview of the converted catalog values for the used standard stars. Errors are a combination of observational and conversion fluctuations.

questioned the usability of the SDSS-7 catalog for our purposes, an alternative had to be found.

All observed stars are very well know standards and can be found in the Landolt catalog for UBVRI standard stars. Using the conversion equations of Jester et al. (2005), these flux values can be converted to the required Sloan filters. This was done for all the stars in each filter, yielding their correct magnitudes. It was then possible to determine the nightly zero points and the airmass dependence for each filter using the IRAF routines outlined in section 2.2.2. By using this detour, all images could be calibrated with a decent accuracy.

A fully detailed overview of the obtained data from the William Herschel Telescope can be found in appendix A.

Band	ZP (mag)	Extinction a	fit rms
Night 1			
u	1.016	0.513	0.164
g	−1.828	0.267	0.053
r	−1.911	0.122	0.036
i	−1.675	0.061	0.059
z	−1.287	−0.008	0.044
Night 2			
u	0.816	0.672	0.100
g	−1.911	0.324	0.047
r	−1.596	−0.131	0.033
i	−1.761	0.133	0.037
z	−1.385	0.062	0.035
Night 3			
u	2.854	−0.950	0.101
g	0.036	−1.079	0.034
r	−2.234	0.461	0.098
i	−0.366	−0.839	0.029
z	0.279	−1.056	0.081

Table 4.4: Zero points and extinction values form least squares fits to the standard star magnitudes.

The San Pedro Martír observing run

5

A few observations and much reasoning lead to error; many observations and a little reasoning to truth.

Alexis Carrel

5.1	Site and observations

The first acquisition of data for the FRIEDL (see section 1.4) project was done during several nights at the end of April 2011 at the San Pedro Martír (SPM) observatory in Mexico. Both northern and equatorial galaxies were imaged in optical and near-infrared bands. For the FRIEDL galaxies, 3 nights of optical imaging and 5 nights of near-infrared data were gathered with an average seeing of 2.08 arcseconds.

5.1.1   Instrumental setup

The National Astronomical Observatory of Mexico (NAO 2012) is located in the Sierra de San Pedro Martír (Cruz-Gonzalez et al. 2003) at an elevation of 2830m. The site itself lies in the middle of a pine forest, which is fed by short periods of heavy precipitation. In between those periods, most nights are clear and dry with a reported median seeing of 0.59 arcseconds. During this observing run, air humidity varied between $20 - 30\%$. The site houses various telescopes, of which the 1.5m telescope was used for the optical imaging and the 2.1m telescope for the NIR observations. The 1.5m Ritchey-Chrétien telescope has a focal length of 20.3 m and is equatorially mounted. Attached to the telescope was the La Ruca filter wheel, bearing standard Johnson-Cousins UBV filters. The detector is a SITe4 CCD camera (SITe inc. 1995) which was used in 2×2 binning, yielding a 512×512 pixel area and a $4.3' \times 4.3'$ field of view. Binning of the CCD pixels has the advantage to increase the readout speed and consequently save more time for exposures. Disadvantages of binning are a lower pixel resolution and a larger readout

Figure 5.1: View of the San Pedro Martír observing site. The 2.1 m telescope stands in the foreground while the 1.5m telescope is visible at the right. The entire site is surrounded by a pine forest.

noise. The former did not affect the image quality because the point spread function was sufficiently sampled with this resolution. The readout noise was increased from 13.71 e$^-$ to 23.39 e$^-$ and the gain factor was 8.5 e$^-$/ADU. The CCD has a quantum efficiency of about 45% in U band and $80 - 90\%$ in the other optical bands and saturates at about 65000 ADU. The 2.1m telescope is also of Ritchey-Chrétien design and equatorial mount. The device has a focal length of 28.35 m if the near-infrared instrument CAMILA (Cruz-González et al. 1994) is mounted. CAMILA allows NIR observations in the J, H and K bands with a field of view of 2×2 arcminutes on a CCD of 256×256 pixels. The system is based on a NICMOS3 detector, with a gain factor of 9.6e$^-$/ADU, a readout noise of 50 e$^-$ and a quantum efficiency around 70%.

5.1.2   NIR data and additional optical bands

In order to create a dataset for the FRIEDL galaxies, which covers most of the optical and NIR frequencies, more wavelength coverage is needed. As mentioned before, NIR observations on the SPM 2.1 m telescope covered the NIR part of the spectrum. The five galaxies were images in the standard J, H and K bands. Both observations and data reduction of the NIR images were done by Ivanio Puerari, research associate of the INAOE and co-investigator in the FRIEDL project. For this work, only astrometrical and photometrical calibration was added to the reduced images. In accordance with calibration of previous data (see e.g. section 3.2.4), this set was also calibrated to the 2MASS catalog magnitudes. Astrometrical information was added by aligning stars
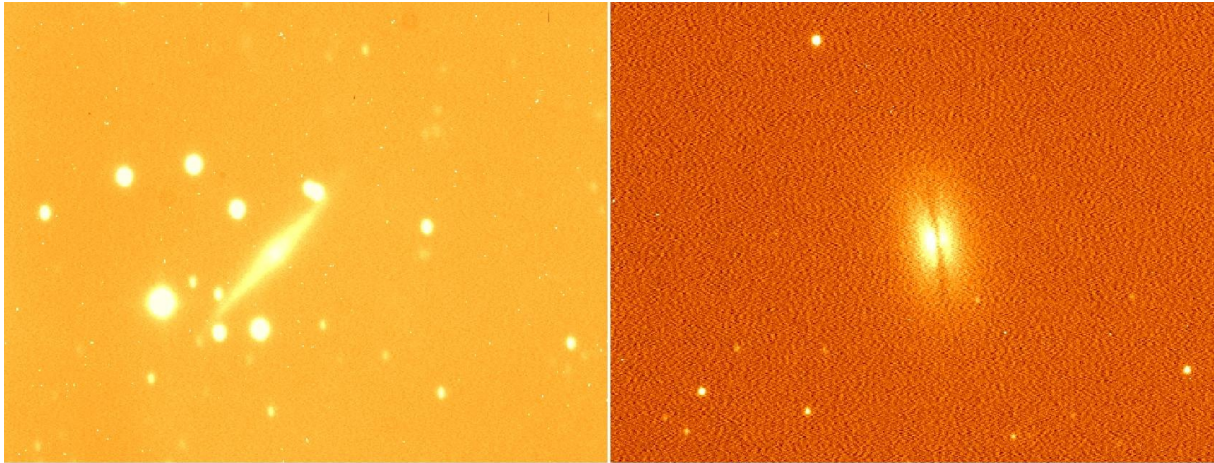
42

Figure 5.2: Left: 600 seconds V band exposure of UGC 4754 without a working guiding system, but with a tracking system. Right: one of the many 30 seconds V band exposure of NGC 4370 under the same conditions.

from the PPXML catalog. Apart from the NIR part of the spectrum, it is also desired to cover the redder part of the optical spectrum. With U, B and V imaging, only blue to green colours are obtained. The Sloan Digital Sky Survey (SDSS, York et al. (2000)) provides imaging in the ugriz broad bands. Inspection of these data for the northern FRIEDL galaxies found that u and z bands were of lesser SNR and were therefore not used. Good quality imaging in the g,r and i band was used to complete the optical/NIR dataset for the FRIEDL galaxies.

5.2	Data reduction

5.2.1 Imaging

Optical and NIR imaging was done during 9 consecutive nights at the end of April 2011. Among others, the northern and equatorial FRIEDL galaxies were observed in U, B and V band. Some problems during the observation prevented efficient imaging and rendered several exposures unusable. The guiding system of the telescope failed during the first night, which resulted in fuzzy images of long exposure. Observations had to be limited to short exposures with only the tracking system to correct for atmospheric and sky movement. Figure 5.2 shows the effects of a poor working guiding system for UGC 4754, which was not reobserved afterwards due to timing constraints. During the first night it was thus only possible to make many short exposures in order to reach the desired image quality. Another known issue with the 1.5m telescope is its reputation to have inconsistent pointing, which can lead to telescope jumps, see figure 5.3.
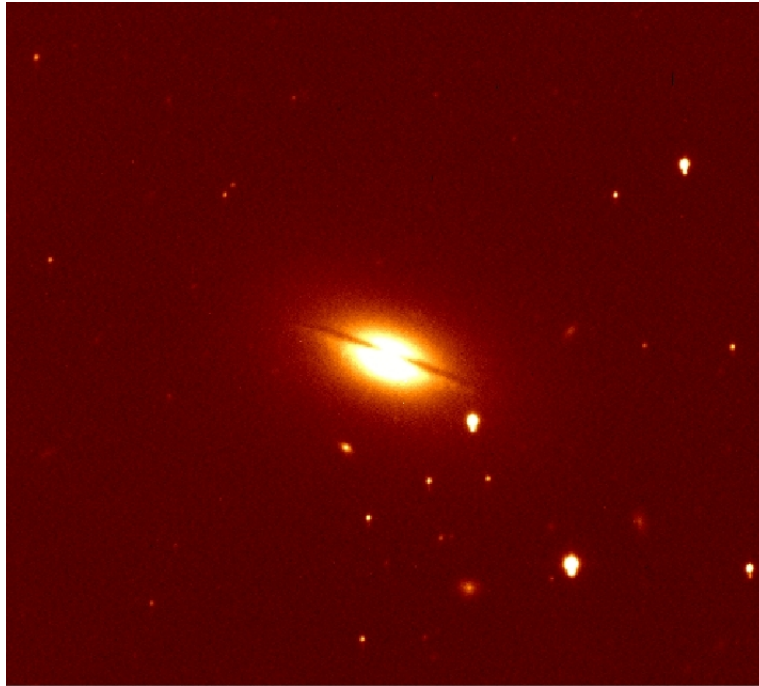
Figure 5.3: Telescope jump during a V band observation of NGC 5525. This is impossible to correct for, the galaxy was thus reobserved.

The cleaning of the images was done the same way as outlined before, using ESO-MIDAS routines. Master bias frames and master flat fields were created by median combining. All science objects, including standard stars, were then bias subtracted and divided by their master flat. Estimates of the sky background were again done by determining the mode of source-free regions around the galaxies and subtracting this value from the image. Cosmic ray identification and removal was executed by the specialized ESO-MIDAS routine. As a final step, all images were divided by their respective exposure time.

Alignment of the images could again be done before the photometric calibration because of the small airmass variations between first and last exposure, see section 4.2.1. A set of reference stars was chosen and for each star a 2-D Gaussian profile was fitted to the point spread function to pinpoint its location. This was done in all images to calculate the offsets for each image compared to the reference one. All frames were then shifted and rotated up to an accuracy of half to one tenth of a pixel. Co-adding of a small set of frames was done by the previously used median method in ESO-MIDAS. Some observations consisted out of many short exposures (see above) in one observing band. For these large set of frames, a sigma-clipping median method could be used to make the co-addition. The advantages of this method is to sweep out many statistical fluctuations and random instrumental effects. This can, unfortunately, only be done when combining a large set of frames.

5.2.2 Photometry and cros-aligning, problems

To save the time lost due to guiding problems, no standard stars were observed during the first night. At first it was attempted to calibrate these data to catalogued magnitudes of the stars in the field of view of the galaxies. This works well for most optical and NIR data, but U band data is very scarce and consequently, no catalogs that hold the required stars were found. To overcome this problem and still make the calibrations in a consistent way, an alternative approach must be used. During the following nights, very well known standard stars were taken, for which U band magnitudes were available in refereed catalogs. This way, the observed galaxies from these nights could be successfully calibrated and with them also the stars in the field of view. Once these stars were at the correct flux scale, their magnitudes could be determined and compared to those measured in the first night. In other words, the observations of the first night were calibrated using newly created standard stars, based on photometric information from the other nights. The transformation equation for night one will thus hold no airmass dependency and follow equation 3.1 for each wavelength. The other nights will then follow the more general equation 2.3 for each band. Table 5.1 lists the obtained calibration parameters. After calibration, the images from different nights could be cross-combined to make the resulting science frame with high SNR. Alignment was performed by using the standard method outlined above. To combine the frames, the average value for each set of corresponding pixels was calculated and stored in the resulting frame. It turned out that the photometric accuracy was better preserved by taking the average instead of the median of the pixel sets. As a final step, astrometric information was added to the resulting images using GAIA, see section 2.2.4. Due to the high astronomical seeing for this observing run, WCS information could only reach accuracies of 0.8 arcseconds, which is somewhat less then the previous observing runs.

A fully detailed overview of the obtained data for FRIEDL can be found in appendix A.

Galaxy/Band	ZP (mag)	Extinction a	fit rms
Night 1			
NGC 4370 U	4.999	n/a	0.019
NGC 4370 B	3.116	n/a	0.100
NGC 4370 V	3.084	n/a	0.161
NGC 5485 U	5.275	n/a	0.081
NGC 5485 B	3.333	n/a	0.056
NGC 5525 U	5.039	n/a	0.203
NGC 5525 B	3.068	n/a	0.082
NGC 5525 V	2.990	n/a	0.101
Night 2			
U	4.461	0.534	0.003
B	2.774	0.302	0.004
Night 3			
U	4.572	0.470	0.002
B	2.845	0.257	0.001
V	2.739	0.132	0.006

Table 5.1: Zero points and extinction values form least squares fits to the standard star magnitudes.

Dust properties of the FRIEDL galaxies

6

Somewhere, something incredible is waiting to be known.

Carl Sagan

The previously processed data contain a huge amount of information that could and probably will lead to large investigations and much valuable science. However, these efforts would not fit the time scale set for this master thesis. As an example science case, to demonstrate part of the potential of this data, a further analysis of the SPM subset of the FRIEDL project is presented. As mentioned before in chapter 1, optical and near-infrared images can be of great use to study dust properties from their extinction effects. This chapter will use two different ways to map the attenuation of five dusty ellipticals from FRIEDL. Section 6.1 will make use of colour maps and reddening effects of the dust, while section 6.2 will make use of a more advanced technique based on Multi-Gaussian Expansion fits for each galaxy. Attenuation maps can then be used to construct optical depths and dust mass maps, see section 6.3 and section 6.4 respectively.

6.1	Colour index maps

6.1.1 Attenuation, extinction and reddening

When light passes through the interstellar medium, it gets scattered and absorbed by dust grains. Scattered light will travel on in a different line of sight, while absorbed light will be radially re-emitted at longer wavelengths. The effects of both processes are often named together as extinction by dust. As a consequence of these processes, a certain stellar flux will lose part of its initial intensity on its trajectory through the ISM. As outlined in Calzetti et al. (1994), attenuation of starlight is the difference between emitted and observed flux in magnitude units:

$$A_\lambda = -2.5 \cdot \log\left(I_{\lambda,obs} / I_{\lambda,emit}\right).$$ (6.1)

Thus, extinction is the effect caused by starlight when interacting with the individual dust grains. Whereas attenuation is more linked to the global loss of intensity of starlight, taking into account both the spatial distribution of the dust and the individual extinction effects of the dust grains.

Stellar fluxes and extinction by dust may be highly wavelength-dependent, leading to a changing attenuation for different observing bands (Binney 1998). In general blue light is attenuated much more efficiently than red light. Therefore, objects appear redder when their light has undergone scattering and absorption on its way to the observer. This phenomenon is often referred to as interstellar reddening and should be separated from the cosmological reddening due to high redshifts. Cosmological reddening is caused by the expansion of the Universe, shifting electromagnetic waves to longer wavelengths. The farther away an object resides from us, the higher this redshift will be, making them redder compared to nearby objects of the same class. Fortunately, the galaxies presented here are quite nearby, with NGC 5525 being at the largest redshift of $z = 0.018523$. It is therefore safe to assume that cosmological reddening will play a negligible role in the total reddening.

6.1.2 The use of the NIR data

In addition to the UBV optical data from San Pedro Martír and the SDSS archive data, the galaxies were also observed in the J,H and K filters at San Pedro Martír (see section 5.1.2). Extinction by optical dust is far less effective in the NIR, making these images less useful to determine the dust mass this way. JHK imaging will however be an important contributor to the constraining of the panchromatic fits and the 3-D radiative transfer models, which should be the follow-up of this work. Figure 6.1 compares the JHK bands for NGC 4370 with the V band image. It is clear that the dust lane in the NIR is far less prominent compared to the optical image, or not even visible at all. Only the J band image, which is closest to the optical part of the spectrum, shows signs of extinction by dust. MGE modelling of NIR images turned out not to be effective, with little or no dust structures visible after analysis. Colour maps (J-H, H-K) did show the presence of a dust lane, but the errors are often quite big. Nevertheless dust maps could be created and total dust masses extracted. However, upon computing the general total dust mass from each wavelength-based total dust mass (see section 6.4.1), the H-K value was often rejected based on a larger than 3-sigma deviation of the general total dust mass.
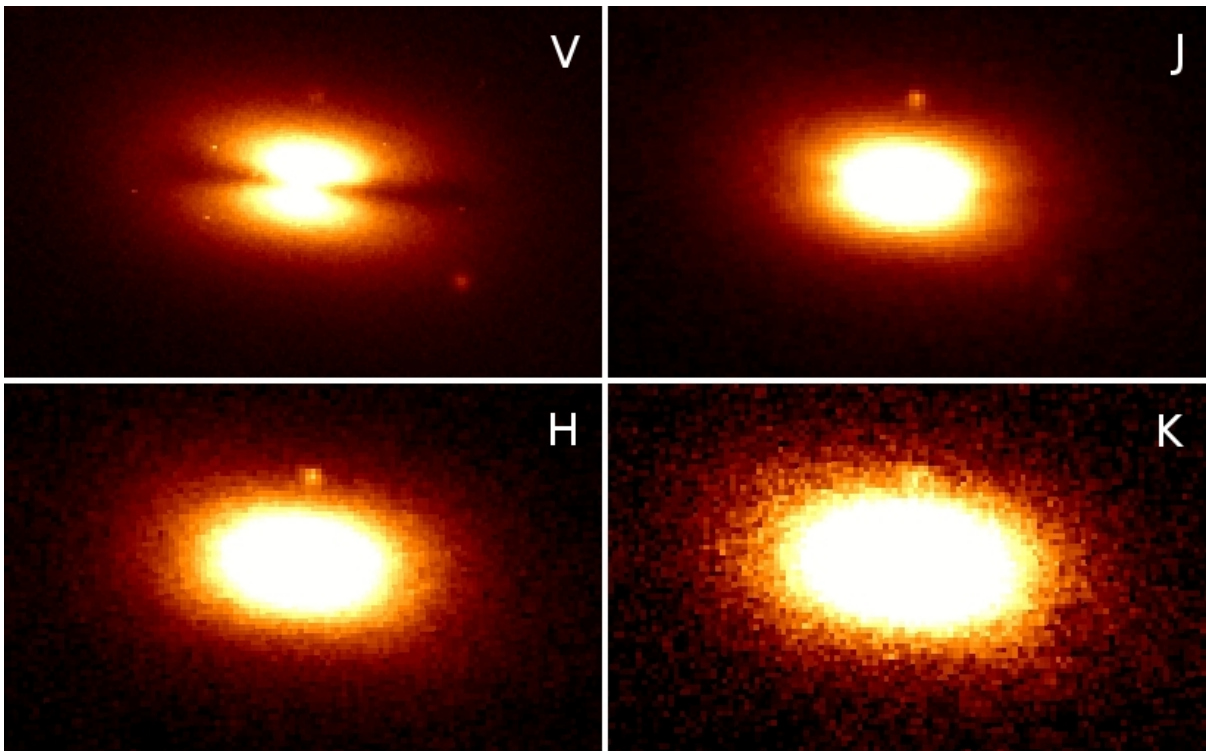
Figure 6.1: Near-infrared images of NGC 4370 at high contrast in an attempt to better visualize the dust lane. Upper left is the optical V band image of the same galaxy for reference. This image shows a clear dust lane running through the galaxy's centre. Only the J band image has a slight hint of this dust lane.

6.1.3   Colours

In astronomy, objects are imaged in broad or narrow band filters, collecting photons around certain central wavelengths. Just like many other quantities, flux scales need to have a zero point and a unit be physically relevant. The distance to an astronomical object is often a large point of uncertainty. It is therefore much more trustworthy to rely on relative measurements for the determination of physical quantities. The difference between the magnitude of two observing bands is called the colour index or simply the colour of an object. Colours are thus determined as a ratio of fluxes at different wavelengths, making these relative measurements distance independent. Colour indices can be directly converted to attenuation difference maps using:

$$(B - V) = (B_0 + A_B) - (V_0 + A_V) \tag{6.2}$$

$$\Updownarrow$$

$$(B - V) - (B_0 - V_0) = (A_B - A_V), \tag{6.3}$$

where B and V represent the observed magnitudes of a galaxy in this band and B_0 and V_0 the intrinsic magnitudes. This means that the difference in attenuation in B and V band of a galaxy is the difference between its observed and intrinsic colour index. The challenge is to define this intrinsic colours of the galaxies. In the case of single stars, intrinsic colour indices can be linked to the spectral types, achievable through spectroscopy. To some extent, spectroscopic analysis of the stellar populations could be used for an estimation of the intrinsic colours of the galaxies. This, however, lies beyond the scope of this work and a more empirical approach is used. Starting from the idea that the majority of the interstellar dust resides in the central dust lane, it is assumed that the regions around the dust lane are more or less dust-free and thus only suffer from a negligible amount of extinction. By selecting the assumable dust-free regions around the primary dust lane and determining the average pixel value, it is possible to estimate the intrinsic colour index of the galaxy in these regions. Figure 6.2 shows a B-V image of NGC 4370, the assumable dust-free regions are overlaid on the image. Early-type galaxies are found to be more constant in colour compared to spirals or irregular galaxies. It was therefore assumed that the average colour index in the outer regions would be the same in the regions where the dust lane appears. This extrapolation then permitted to determine the attenuation difference of the interstellar dust from the colour difference maps. Figure 6.3 shows the average intrinsic reddening for different galaxies in different colours. Some scattering can be seen in the average reddening values of the different galaxies. This may be attributed to different stellar populations, metallicity or age on the one hand. On the other hand, it may be possible
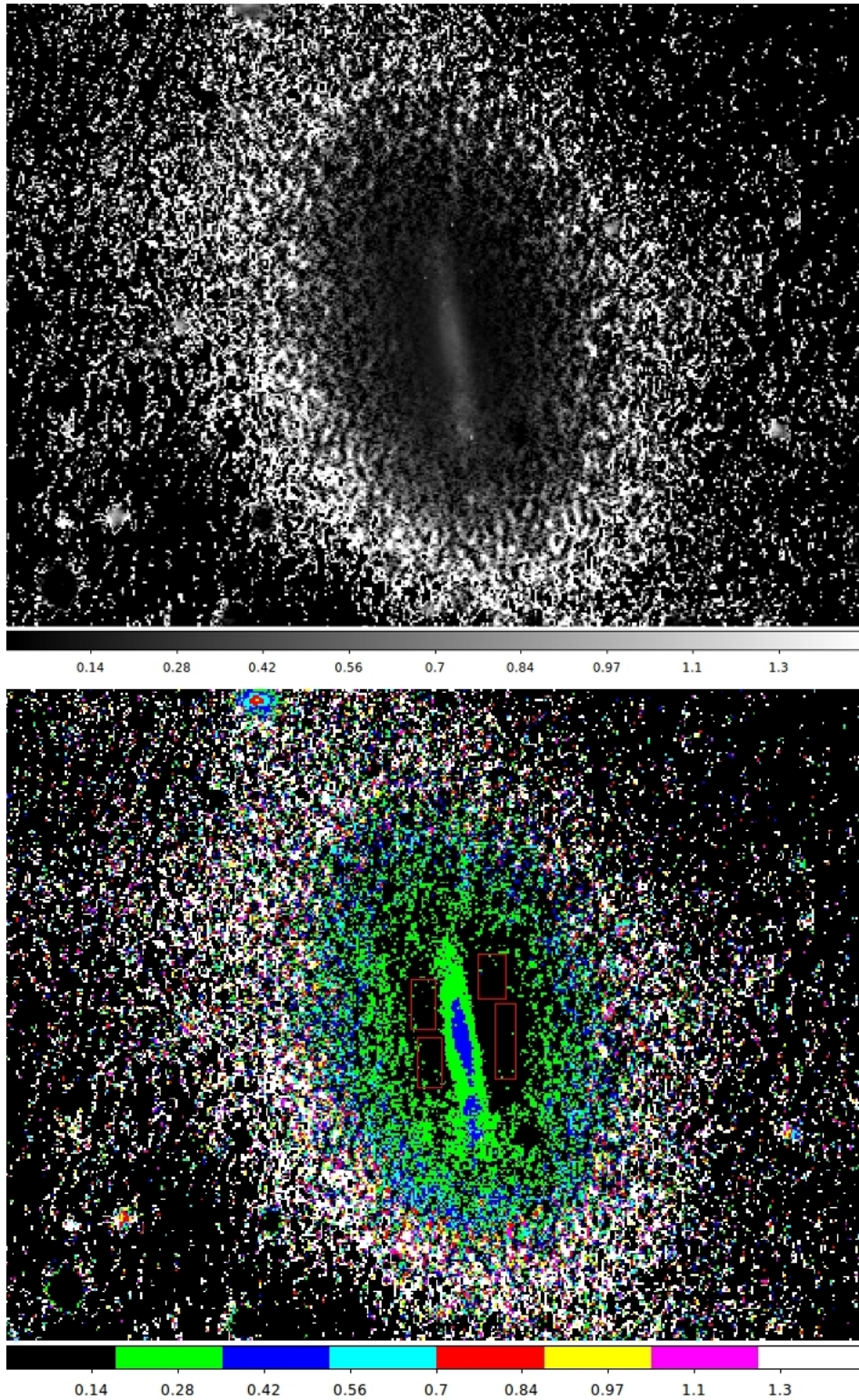
Figure 6.2: Top: B-V colour image of NGC 4370. The galaxy is clearly visible in the centre, with a prominent dust lane. The outer regions of the image are basically residuals of sky-sky subtractions and do not have a physical meaning. Bottom: discrete colour code map to distinguish the dust (green, blue) from the surrounding dust-free regions (black). The red rectangles indicate the regions used to determine the intrinsic colour of the galaxy.
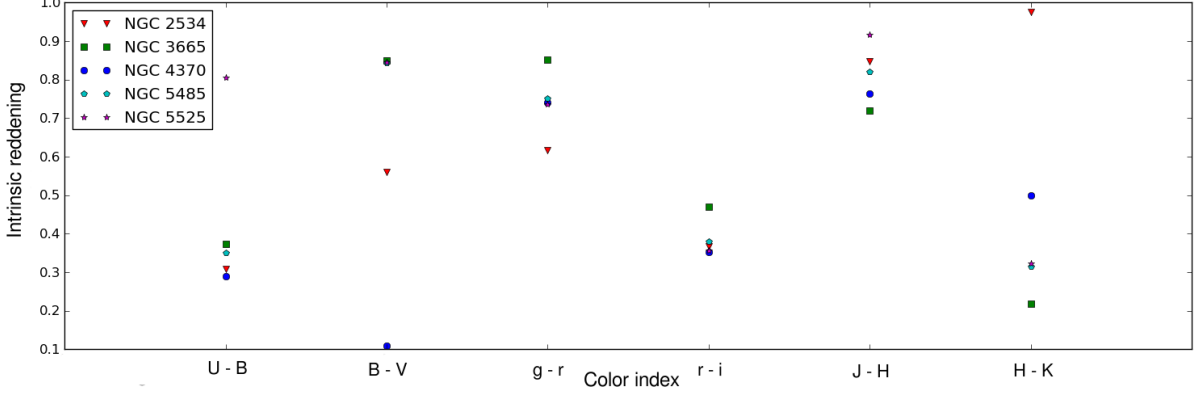
Figure 6.3: Intrinsic reddening for each of the colour indices of the five galaxies. The large scatter in certain colours may hint to different stellar populations and/or hidden dust structures.

that this technique misses some dusty structures outside the dust lane of certain galaxies. The former is more likely than the latter given the fact that no galaxies have the exact same stellar populations.

In the present study, several attenuation difference maps were created for each of the five galaxies. As mentioned in section 5.1.2, three main sets of filters were acquired for this subset: UBV, gri and JHK. To avoid uncertainties in rescaling and aligning the images between these sets, only intra-set colour maps were created: U-B, B-V, g-r, r-i, J-H, H-K. Additionally, a B-i map was created for each galaxy to probe a larger wavelength difference and compare with the B-I values for NGC 4370 achieved by Finkelman et al. (2008). The actual process of converting the reduced images into attenuation difference maps was done by a self-written IDL routine. IDL (ITTvis 2012) or Interactive Data Language, is a useful programming language for processing arrays. The astronomical community has created the AstroLib (NASA-GSFC 2012) database with specialised IDL routines for handling FITS files.

In a first step, the seeing of both images is compared and the image with lowest seeing is convolved to match the other image in seeing. This was done by the AstroLib routine 'convolve()' (Varosi & Landsman 1993). An intermediate step, is the alignment and rescaling of the convolved image to the pixel scale of the other one, done by 'hastrom()' (Landsman 1989). Last step is to make the colour map by computing

$$m_a - m_b = -2.5 \times (log(image_a) - log(image_b)), \qquad (6.4)$$

where the indices a and b represent one of the used filters and $image_a$ and $image_b$ represent the arrays of pixel fluxes which make up the images. A simple ESO-MIDAS task then allowed to define the dust-free regions and subtract the intrinsic reddening from $m_a - m_b$ to construct the attenuation difference map $A_a - A_b$, often referred to as
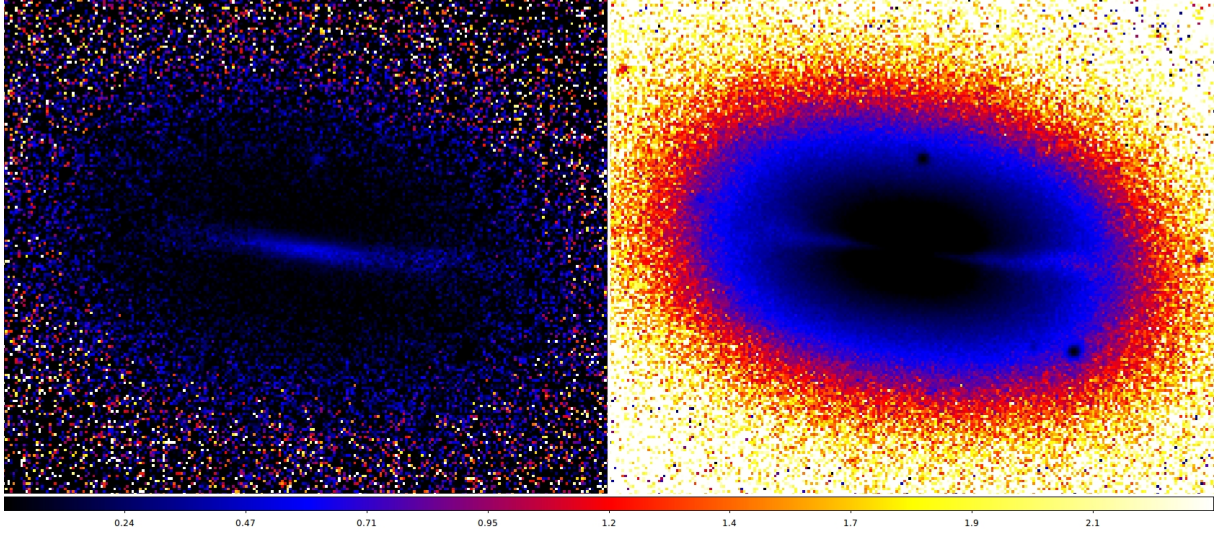
Figure 6.4: Left: attenuation difference map for NGC 4370, based on the r-i colour map. Right: corresponding error map with the same colour code.

selective attenuation.

6.1.4   Error analysis

The uncertainties on the maps produced by equation 6.4 and post-processed by ESO-MIDAS was derived by using the standard error-on-function formula:

$$\sigma_f^2 = \sum_{i=1}^{n} \left(\frac{\partial f}{\partial a_i} \right)^2 \sigma_{a_i}^2, \tag{6.5}$$

where a_i, $i = 1, \ldots, n$ are a number of parameters (pixel fluxes) of the function f. In this case, the function f is a sum of logarithms of fluxes. The signal-to-noise ratio of the initial images is quite high and the galaxy is clearly visible. It is therefore justified to assume a Poissonian error on the flux in each pixel: $\sigma_{a_i} = \sqrt{a_i}$. All this yields:

$$\sigma_{m_i - m_j} = \frac{2.5}{\ln 10} \sqrt{\frac{1}{image_a} + \frac{1}{image_b}}. \tag{6.6}$$

Figure 6.4 shows the r-i attenuation difference map for NGC 4370 and the corresponding error map, derived from 6.6.

Creating colour maps and converting them to attenuation maps is a quick and dirty job which relies purely on the given data (broad band imaging) and the assumption that colours remain the same throughout the entire galaxy. This purely empirical approach is however sufficient to extract differences in optical depth (section 6.3.1) and, later on,

dust masses (section 6.3.2) for the galaxies.

6.1.5 Comparison with previous colour maps

Colour maps for most of these galaxies were already constructed by Finkelman et al. (2008, 2010). Figure 6.5 shows B-i colour maps from this work compared to B-R images from Finkelman et al. (2010) and a B-I image for NGC 4370 from Finkelman et al. (2008). There was no literature colour map found for NGC 5525, only the one from this work is displayed. B-i images cover a larger wavelength range than B-R, this means reddening effects will be larger in the former. Larger reddening permits a more detailed mapping of the dust structures, as is visible in the figure. Quite a few different morphologies of the dust lanes can be identified. NGC 4370 has a very straight line, which probably points at inclinations close to the edge-on value of $90°$. The other galaxies express a more arc-shaped dust lane, which hints towards lower inclinations. The central regions of all these galaxies with arc-shaped dust lanes show a small round structure of increased reddening. This could be identified as a tight clump of dust in the nucleus of the galaxy, but it is more probably that this is a fake signal. Comparing with the dust maps from Multi-Gaussian Expansion fitting (see section 6.2 and appendix B.2) not all of these central regions are visible and thus not caused by dust reddening. Due to the high brightness of these central regions, they will have a larger seeing disk. Finkelman et al. (2008) already mentioned that these seeing affected central regions should be treated with caution before extracting dust masses. In the colour maps for NGC 3665 a torus-shaped dust structure can be identified, indicating that little dust is present in the central regions. It may thus be that the dust distribution in early-type galaxies is more like a torus rather than a thin disk.

6.2	Multi-Gaussian Expansion fitting

One of the possible underestimations of the previous method is the assumption of a constant intrinsic colour index for both centre and outer regions of the galaxy. Variations of the galaxy's intensity may be different in each observing band and the intrinsic reddening may not be constant throughout the galaxy. Looking for dusty structures in colour maps thus suffers from a few unpredictable errors which are very difficult to estimate or correct for. A great improvement on this, would be the treatment of each broad band image on its own and use a basic model for the galaxy's intensity variations. Previous efforts have already been made to make basic, dust-free models of elliptical galaxies based on fitting to single images (Finkelman et al. 2012, 2008; Patil et al. 2007). These efforts usually make a rough model by fitting ellipses or a mathe-
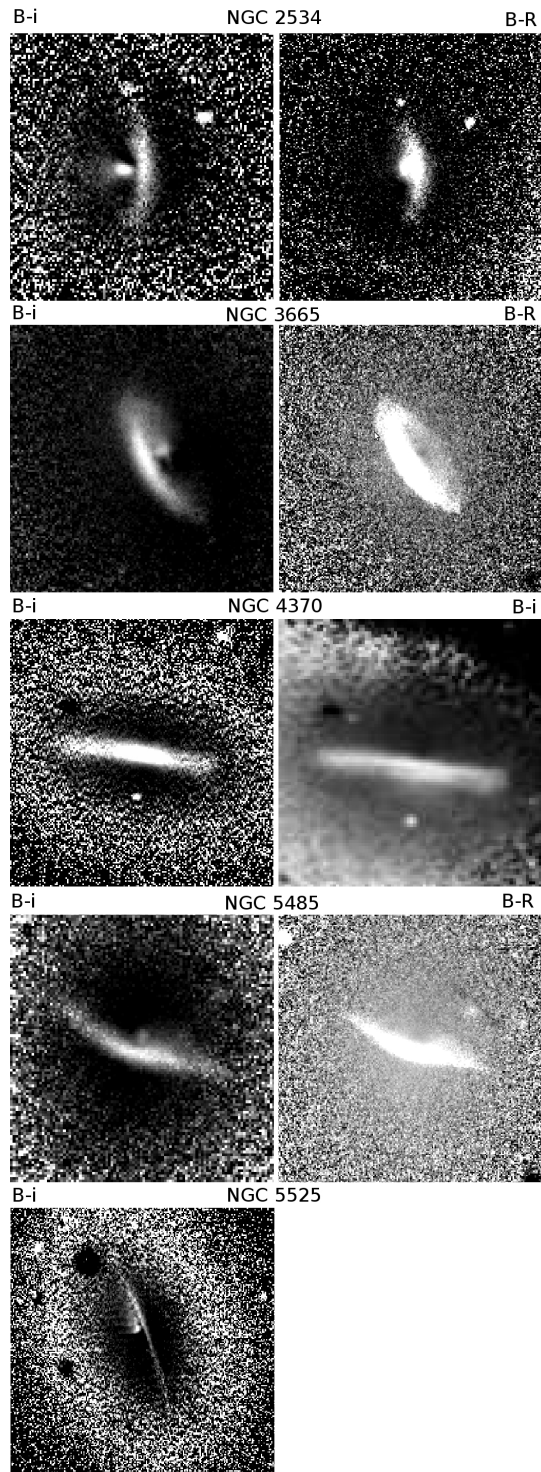
Figure 6.5: Colour maps for the five different galaxies. Left are B-i maps from this work, right are B-R and B-i colour maps found in the literature. Various shapes can be identified for the different galaxies. Different shapes are probably caused by different inclinations and position angles. No colour maps were found for NGC 5525.

matical model such as the de Vaucouleurs or Sérsic laws to the light distribution. In this work, a slightly more complicated approach will be used to model the light distribution of the galaxies. This method is called Multi-Gaussian Expansion fitting.

6.2.1 The Multi-Gaussian Expansion fitting procedure

The idea of MGE fitting is to model the surface brightness profile of a galaxy as close as possible by summing multiple 2-D Gaussian functions. The technique was first presented by Emsellem et al. (1994). Later, a full IDL package was written by Cappellari (2002) to search for the best fitting combination of Gaussians. Described below is the method used in these IDL routines.

The routine makes use of the pixel coordinate system of the image, with x' and y' axis in the plane of the image, centred around the galaxy nucleus and the z' axis towards the observer. The surface brightness $\Sigma(x', y')$ of a galaxy can then be written as:

$$\Sigma(x', y') = \sum_{j=1}^{N} G_j(x', y') = \sum_{j=1}^{N} \frac{L_j}{2\pi\sigma_j'^2 q_j'} \exp\left[-\frac{1}{2\sigma_j'^2}\left(x_j'^2 + \frac{y_j'^2}{q_j'^2}\right)\right], \qquad (6.7)$$

where L_j is the total luminosity of each Gaussian, q_j' the observed axial ratio and σ_j' the dispersion along the major axis. Before this MGE surface brightness can be compared to the observed one, it needs to be convolved with the instrumental point-spread-function (PSF). This PSF can be constructed again by the use of multiple (circular) Gaussian functions:

$$PSF(R') = \sum_{k=1}^{M} \frac{G_k}{2\pi\sigma_k^{*2}} \exp\left(-\frac{R'^2}{2\sigma_k^{*2}}\right) \qquad (6.8)$$

and fitting them to the PSF of a star in the image of the galaxy. Here $R'^2 = x'^2 + y'^2$ is the radial polar coordinate and $\sum_{k=1}^{M} G_k$ must be equal to 1. A useful characteristic of Gaussians is that they can be convolved separately and re-added afterwards, making the problem computationally less demanding. Upon convolving $\Sigma \otimes PSF$, the total luminosity of a Gaussian function does not change. Each Gaussian then has the following convolved surface brightness:

$$\bar{\Sigma}(x', y') = L \sum_{k=1}^{M} \frac{G_k}{2\pi\bar{\sigma}_k'^2 \bar{q}_k'} \exp\left[-\frac{1}{2\bar{\sigma}_k'^2}\left(x'^2 + \frac{y'^2}{\bar{q}'^2}\right)\right], \qquad (6.9)$$
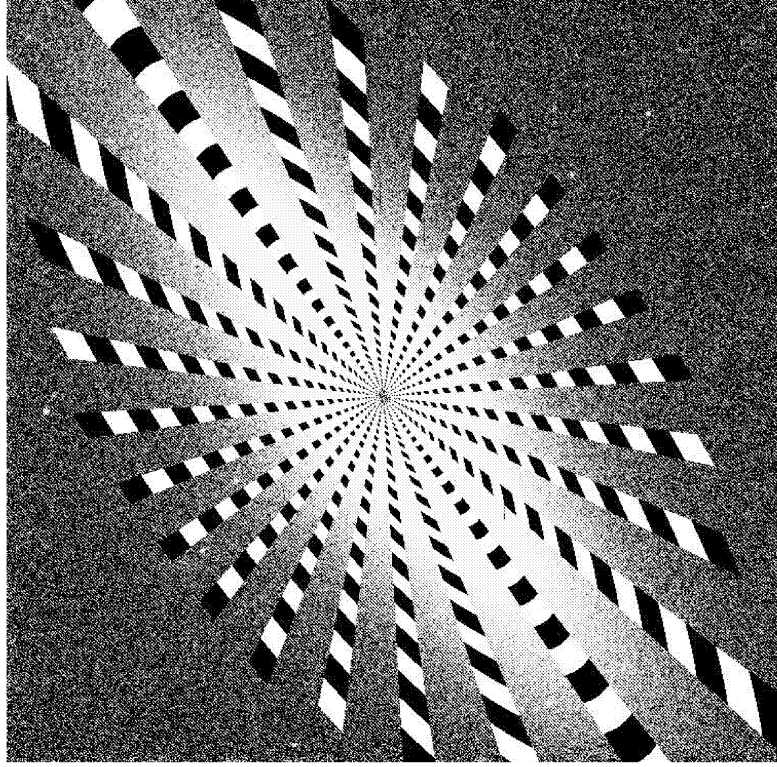
Figure 6.6: Example of how the IDL routine divides the galaxy's surface in different sectors before comparing the MGE model with the pixel values of the original image.

with

$$\begin{cases} \bar{\sigma}_k'^2 = \sigma'^2 + \sigma_k^{*2} \\ \bar{\sigma}_k'^2 \bar{q}_k'^2 = \sigma'^2 q'^2 + \sigma_k^{*2} \end{cases} \tag{6.10}$$

Thus, MGE models make use of standard Gaussian functions and convolution properties to mimic the surface brightness of a galaxy. As mentioned, the IDL package created by Cappellari (2002) was used here to fit MGE models to the broad band images. The routine defines a set of sectors along the galaxy, uniformly spaced in angle, but logarithmic in radius, at radii $m'^2 = x'^2 + y'^2/q'^2$ (see figure 6.6). The MGE model is compared to the observed image in all sectors and adjusted accordingly, minimizing the χ^2:

$$\chi^2 = \sum_{i,j} \left[\frac{C_{i,j} - \Sigma(x_i', y_j')}{\Delta_{i,j}} \right]^2, \tag{6.11}$$

where $C_{i,j}$ are the observed pixel values and $\Delta_{i,j}$ a weight factor. In order to create a dust-free model, MGE fitting should only be done in the regions of the galaxy where no dust lane or foreground stars are visible. This requires masking the disturbing structures from the image, leaving only the unobstructed parts of the galaxy (see figure
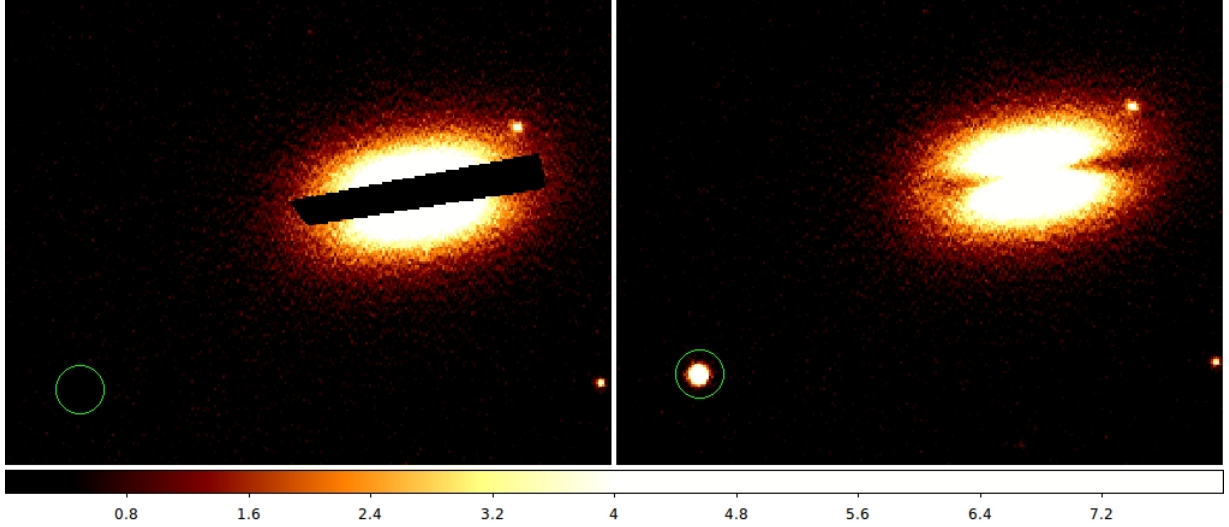
Figure 6.7: Left: masked B band image of NGC 4370, both the galaxy's dust lane and the bright star in the lower left corner were masked before modelling the dust-free galaxy. Right: unmasked image for reference.

6.7). A threshold value must also be defined before starting the program. Pixel values below this threshold were not considered in the fit, because their SNR was too low to be reliable.

The fitting procedure requires a few initial parameters to get the process going and uses the Bounded-Variables Least-Squares (BVLS) algorithm (Lawson 1995) to optimize the fit. A good guess of the galaxy centre, its ellipticity and position angle resulted in decent χ^2 values within minutes. It was then only a matter of fine tuning some initial parameters to get to the final model, with χ^2 values around unity. Figure 6.8 shows the original, dusty B band image of NGC 4370 overlaid with contours. The dust lane clearly has an influence on the surface brightness, deforming most of the inner contours. On the right part of the figure is the dust-free MGE model overlaid with roughly the same contours of the masked B band image. The mathematical contours are extrapolated into the masked regions to construct the dust-free galaxy. Apart from some small scale deviations, the model follows the contouring very well and makes this a good fit of the galaxy. At the end of the procedure, a fake image of the dust-free galaxy was created using the MGE model (see figure 6.9).

Similar to equation 6.1, the attenuation maps of the galaxies in each particular wavelength band were calculated from

$$A_\lambda = -2.5 \log \frac{I_{\lambda,original}}{I_{\lambda,model}}. \tag{6.12}$$

Sky subtraction of each image during data reduction might cause some pixels to have
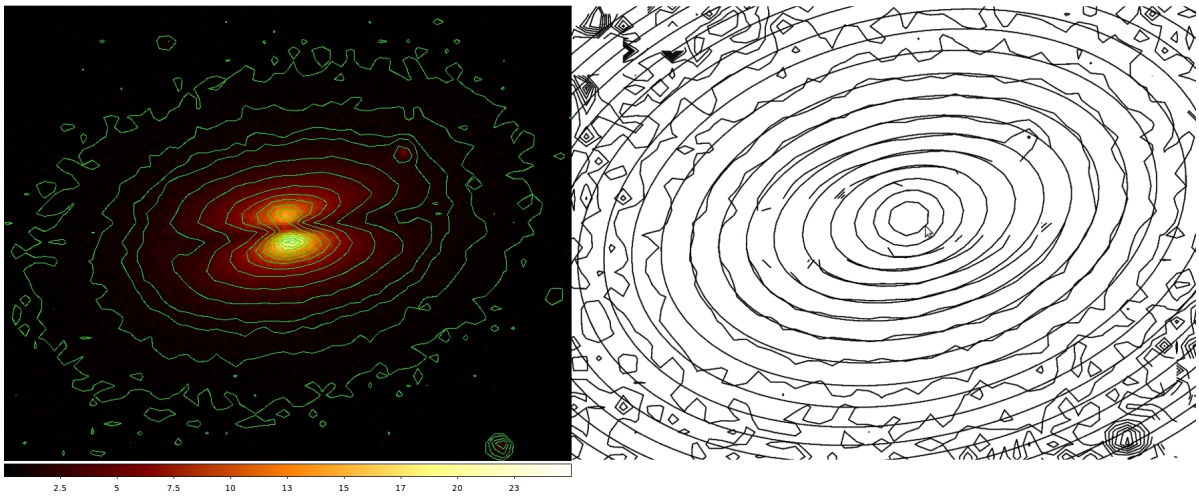
Figure 6.8: Left: B band image of NGC 4370, overlaid with contours to illustrate the effects of the dust lane and foreground stars on the surface brightness. Right: the dust-free MGE model (smooth ellipses) overlaid with the contours of the masked B band image of the same galaxy.
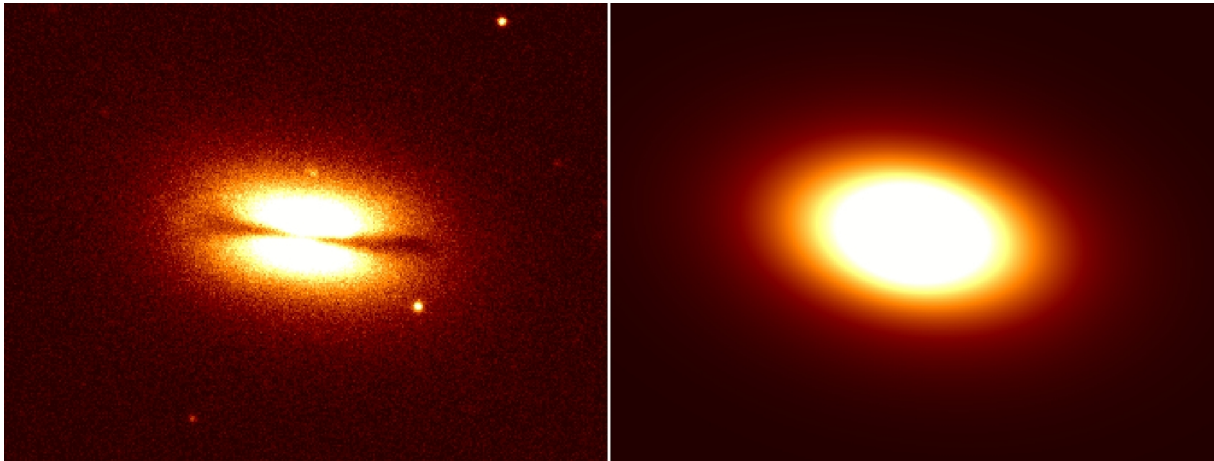

Figure 6.9: Left: observed g band image of NGC4370, the dust lane is prominently visible. Right: MGE model of the image on the left. Only dust-free structures were used for the fitting. The dust lane and foreground stars were masked.

small negative values in the source-free regions. The MGE model doesn't suffer from these non-physical values, yielding a flux ratio which is smaller than zero. Mathematically, log functions cannot handle negative values, thus a lot of nan's appeared in the attenuation maps. A simple filtering loop replaced these with a fixed large negative value (e.g. -123) to make sure they can be identified afterwards.

6.2.2   MGE fits

For each galaxy, a MGE model was made for the UBV and gri bands except for NGC 2534, for which no V band image was available. Each fit required the tweaking of initial values to obtain a desirable accuracy. There were two criteria to label the fit as a good one: one is off course the χ^2 value, which the program strives to minimize. However, not always the smallest possible χ^2 yielded the best overlapping contours. This is because the program fits to all the pixels above the set threshold. In some cases, the outer regions, with low signal to noise, followed very wobbly contours, making it almost impossible to mimic this with a set of Gaussian functions. Another issue is small foreground stars or intrinsic deviations from the global surface brightness profile of the galaxy. All these regions then increased the χ^2 value, even though the fit of the relevant part (i.e the inner, dusty part) of the galaxy could be great (see figure 6.10). A second criterion was needed to account for this: a careful inspection of the contour overlap in the central galaxy regions by human eye. Initial parameters and threshold values were adjusted until the best possible fit was achieved. Table 6.1 lists the final outputs for the MGE fits. Figure 6.11 shows the attenuation maps for NGC 4370. There are some morphological differences on the smaller scales, but the global dust lane is clearly visible in each map. The main difference between the maps is the intensity of the attenuation in the dust lanes, because each wavelength reacts in a slightly different way to the interstellar dust. Attenuation maps for the other galaxies can be found in appendix B.1.

6.2.3   Error analysis

Similar to the error analysis for the selective attenuation from colour indices, error maps were constructed based on the individual errors on the pixel values. Once again, it was assumed that the relevant pixels had a high enough SNR, allowing a Poissonian error on the fluxes. Additionally, it was assumed that the MGE models were virtually errorless because they are a theoretical model which hold no uncertainties in se. The quality of the fit of this model to the observations does however contribute to the overall uncertainty on the attenuation maps. From the previous section, it is clear that the MGE procedure results in good fits. The uncertainty on the pixel fluxes will there-
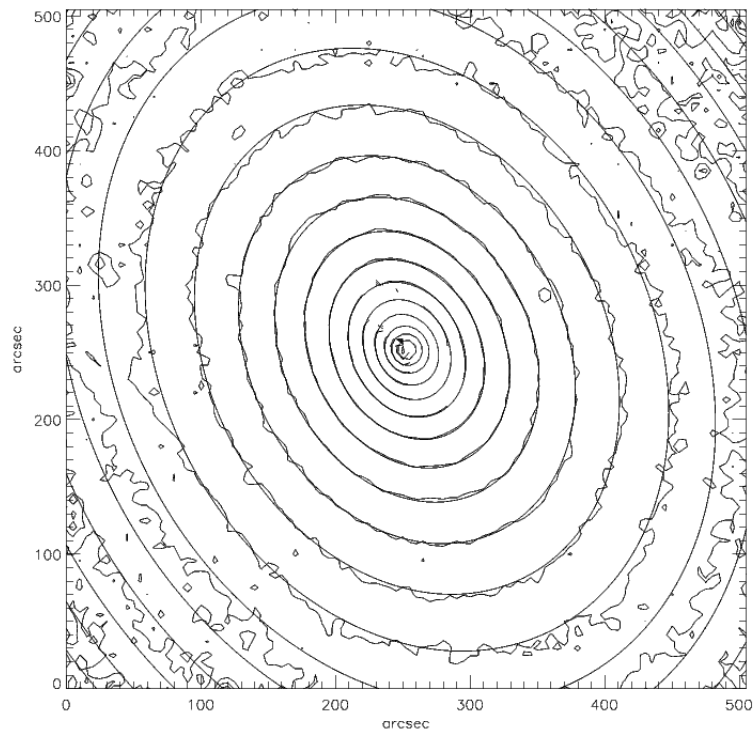
Figure 6.10: The g band fit for NGC 3665, for which $\chi^2 = 12.3123$ is the highest value of the set of fits. Ironically, it is clear that the central regions are very well fitted. NGC3665 is the largest galaxy of the set. Fitting to so many pixels and in outer regions of the image increases the χ^2, making it less representative to indicate a good model.

Band	χ^2	Fitted regions	Fitted pixels
NGC2534			
U	6.5222	566	12147
B	0.7679	474	16286
g	1.0025	337	10773
r	2.4177	494	104574
i	2.8628	503	104044
NGC3665			
U	1.6500	732	70762
B	4.0907	844	74161
V	0.6914	737	119932
g	12.3123	918	128187
r	2.7013	912	34605
i	3.7914	931	12530
NGC4370			
U	2.4482	316	7677
B	1.0311	356	14461
V	0.9689	444	16885
g	2.8946	381	21085
r	1.5553	464	33106
i	1.2951	495	44537
NGC5485			
U	2.9817	710	29371
B	0.9735	703	29140
V	1.0241	747	57551
g	1.1787	783	66742
r	0.7841	841	118182
i	0.9889	870	80615
NGC5525			
U	3.3299	584	9600
B	1.2533	434	11711
V	1.4699	521	21624
g	0.2968	336	17266
r	0.8418	473	29398
i	0.5557	427	41831

Table 6.1: Overview of the MGE fits for each of the bands of the galaxies. The number of regions and used pixels were determined by a threshold value below which the SNR was considered too low to make a reliable fit.
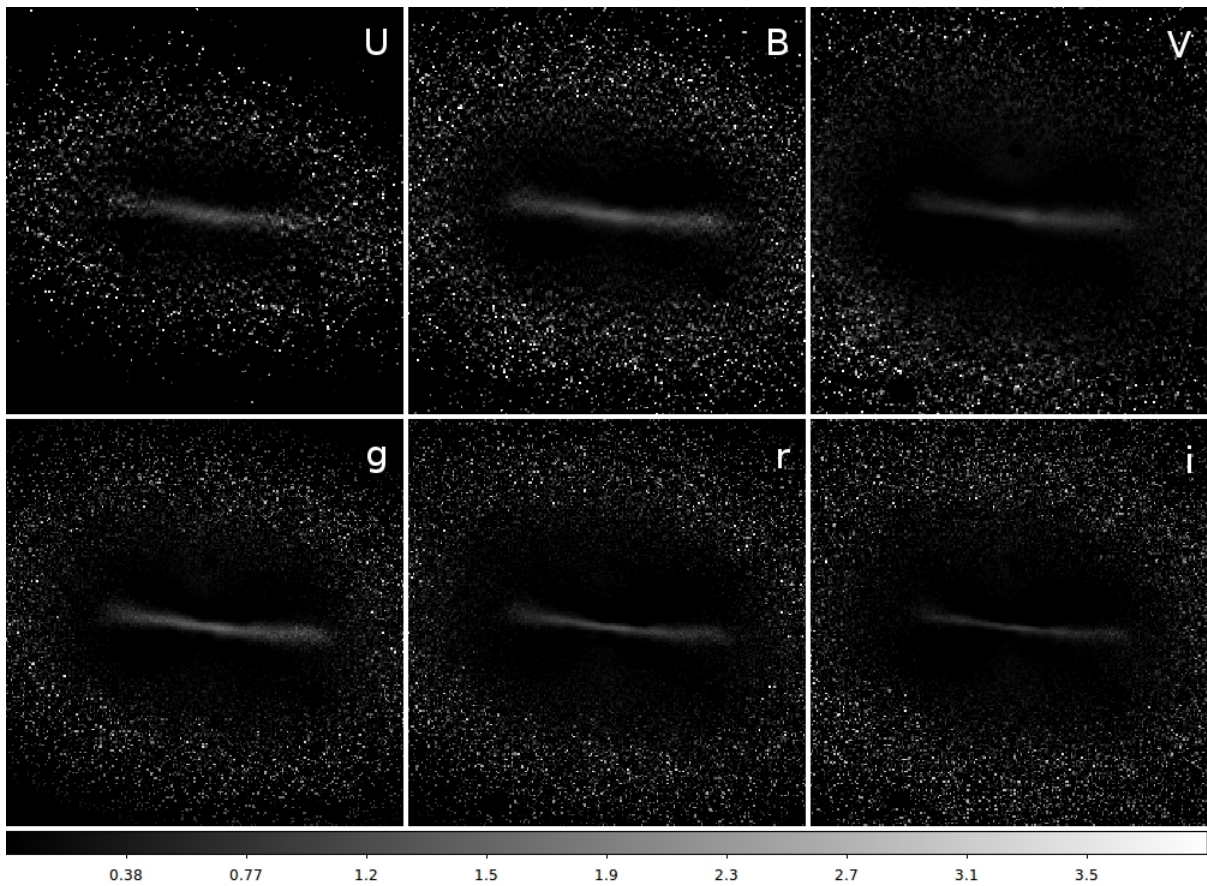
Figure 6.11: Attenuation maps for each of the broad band images of NGC4370. These maps are in fact the residuals between the original and dust-free MGE model images. The residuals begin to dominate in the outer regions of the galaxy, where MGE fitting becomes less effective because the lower SNR of the pixels. In the center, the residuals are almost naught, except off course for the prominent dust lane.
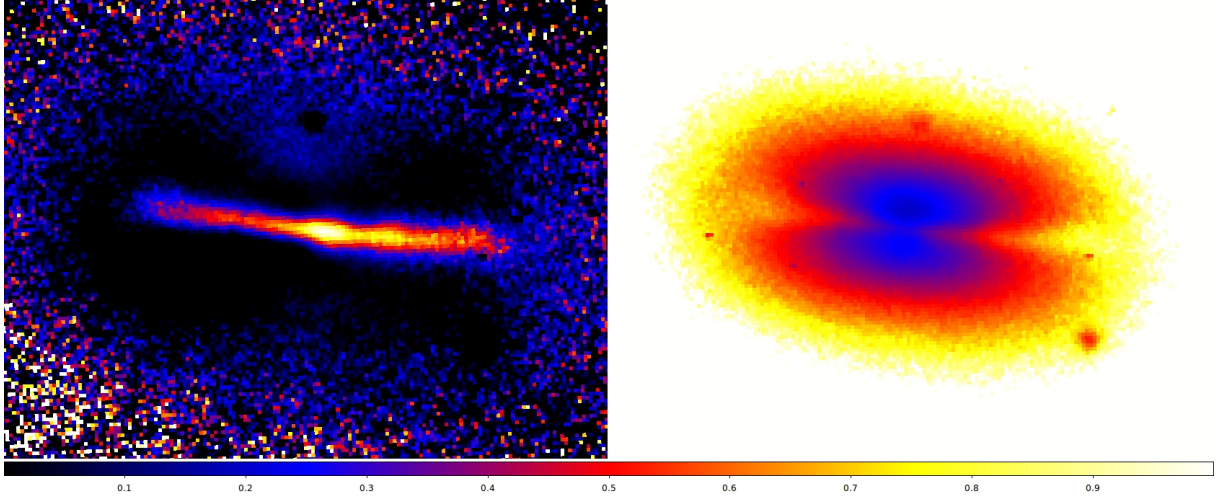
Figure 6.12: V band attenuation map of NGC 4370 (left) along with the corresponding error map (right).

fore be dominant over the hard to quantify uncertainty on the fitting. The full error equation for equation 6.12:

$$\sigma_{A_\lambda}^2 = \left(\frac{-2.5}{\ln 10}\right)^2 \left(\frac{1}{I_{\lambda,obs}^2}\sigma_{I_{\lambda,obs}}^2 + \frac{1}{I_{\lambda,mod}^2},\sigma_{I_{\lambda,mod}^2}\right) + \sigma_{fit}^2 \tag{6.13}$$

thus reduces to

$$\sigma_{A_\lambda} = 1.086\frac{1}{\sqrt{I_{\lambda,obs}}} \tag{6.14}$$

for each pixel. Figure 6.12 shows the V band attenuation map of NGC 4370 and the corresponding error map. The galaxy and dust lane regions clearly show a Poissonian error - brighter regions have larger errors - while the area outside the galaxy has a very high uncertainty because the MGE model fails to mimic the observed image here.

6.3	Attenuation and optical depths to dust masses

6.3.1   Dust distribution and optical depth

The next step in extracting dust masses from optical extinction effects is to convert the attenuation maps into optical depth maps. Optical depth τ_λ is defined by the gradual decay of the intensity of light through a slab of dust:

$$\frac{I_\lambda}{I_{\lambda,0}} = exp\left(\int_0^s \frac{1}{l_\lambda}ds'\right) = exp(-\tau_\lambda), \tag{6.15}$$

with l_λ the mean free path of a photon of wavelength λ. Optical depth is thus a measure for how good the dust extinguishes light. From this equation, it is easy to see that the link between optical depth and attenuation 6.1 is:

$$A_\lambda = -2.5 \log e^{-\tau_\lambda} = 1.086\tau_\lambda, \tag{6.16}$$

for a slab of dust between the emitter and the observer. This is the most basic conversion from attenuation to optical depths, which requires a minimum of dust to achieve certain attenuations. Another approach is assuming a uniform dust-starlight distribution:

$$A_\lambda = -2.5 \log \frac{1 - e^{-\tau_\lambda}}{\tau_\lambda}. \tag{6.17}$$

However, in the case of dust lane galaxies, it is clear that the interstellar dust is not uniformly distributed in between the stars. More realistic models abduct a mixing parameter p, which represents the fraction of the light between the dust and the observer:

$$A_\lambda = -2.5 \log \left(p + (1-p)e^{-\tau_\lambda} \right). \tag{6.18}$$

Both models were originally derived by Walterbos & Kennicutt (1988). The latter assumes a slab of dust and places it somewhere in between the stars. In the case of dust lane galaxies, this is a good representation of the reality. Knapen et al. (1991) tested this model on the Sombrero galaxy and obtained a fraction $p = 0.15$.

6.3.2   Scattering, absorption and dust masses

The computation of optical depths is crucial to the conversion of attenuation to dust masses. Based on the integral in equation 6.15, optical depth can be re-written as:

$$\int_0^s \frac{1}{l_\lambda} ds' = \int_0^s \kappa_\lambda \rho(s) ds' = \kappa_\lambda \Sigma_d \tag{6.19}$$

Where Σ_d is the dust surface mass density of the galaxy and κ_λ the total extinction coefficient for the interstellar dust. κ_λ is simply the sum of both scattering and absorption coefficients: $\kappa_\lambda = \kappa_\lambda^{abs} + \kappa_\lambda^{sca}$. Often the extinction coefficient is computed using the albedo ω_λ of the dust grains, which is the ratio of scattered light and the total extinction:

Band	ω_λ	κ_λ^{abs} (cm^2/g)	κ_λ (m^2/kg)
U	0.6203	15950	4200.685
B	0.6529	11910	3431.288
V	0.6735	8551	2618.989
g	0.6609	10830	3193.748
r	0.6756	7209	2222.256
i	0.6651	5616	1676.918
J	0.5846	3224	776.119
H	0.5200	2351	489.79
K	0.4391	1670	297.736

Table 6.2: Properties of the used dust model for each wavelength band. ω_λ and κ_λ^{abs} values can be found in the tables of Draine (2003), values for κ_λ were calculated using 6.20.

$$\omega_\lambda = \frac{\kappa_\lambda^{sca}}{\kappa_\lambda} \implies \kappa_\lambda = \frac{\kappa_\lambda^{abs}}{1 - \omega_\lambda}. \tag{6.20}$$

On the other hand, the dust mass in an area of the galaxy can be written as the product of the surface density and the surface of that area:

$$M_d = A\Sigma_d = (\alpha_{pix}D)^2 \sigma_d, \tag{6.21}$$

where the conversion of the pixel scale α_{pix} to the corresponding area of the galaxy was used. Both equations combine to the simple conversion of optical depth to dust mass:

$$M_d = \frac{(\alpha_{pix}D)^2 \tau_\lambda}{\kappa_\lambda}. \tag{6.22}$$

In a perfect world, the wavelength dependency of τ_λ and κ_λ should be removed by dividing them. However, it will be clear later that some residual wavelength dependency remains visible in the dust mass determinations. Suitable values for κ_λ, which are quite model-dependent, were obtained from Draine (2003) and listed in table 6.2. The used dust model is a combination of carbonaceous grains and amorphous silicate grains yielding an Galactic $R_V = 3.1$ value.

In the case of the colour maps, which provided a difference in attenuation, the calculations are analogously, but replacing the attenuation by an attenuation difference and the optical depth in the difference between two optical depths in equations 6.16, 6.17 and 6.18. The dust mass can then be calculated just like 6.22:

$$M_d = \frac{(\alpha_{pix}D)^2(\tau_{\lambda_1} - \tau_{\lambda_2})}{\kappa_{\lambda_1} - \kappa_{\lambda_2}}. \tag{6.23}$$

6.3.3   Error analysis

All these calculations increase the uncertainty on the outcome, which will be dominated by the error on the optical depth and on the distance to the galaxies. For each pixel, the following general error equation was adopted:

$$\sigma_{M_d}^2 = \left(\frac{\partial M_d}{\partial A}\right)^2 \sigma_A^2 + \left(\frac{\partial M_d}{\partial \tau_\lambda}\right)^2 \sigma_{\tau_\lambda}^2, \tag{6.24}$$

which specifies to:

$$\sigma_{M_d} = \sqrt{\left(\frac{\tau_\lambda}{\kappa_\lambda}\sigma_A\right)^2 + \left(\frac{A}{\kappa_\lambda}\sigma_{\tau_\lambda}\right)^2}, \tag{6.25}$$

with

$$\sigma_A = \frac{\partial A}{\partial D}\sigma_D = 2\alpha_{pix}^2 D\sigma_D. \tag{6.26}$$

Error maps for the dust maps from the colour indices were derived analogously, with τ_λ simply replaced by the difference in optical depth and κ_λ with the difference between two extinction coefficients. Figure 6.13 shows error maps for both the V band dust map and the B-V colour dust map. It is immediately clear that the dust map from the MGE model has a more symmetric nature and the extent of the dust lane is better constrained. Obviously, it are these dust maps from MGE models that should be used to spatially constrain the dust lane and derive the total mass. Other dust maps with their corresponding error maps can be found in appendix B.2.

6.4	Dust maps and total dust masses

Now that the dust maps are created, it is quite straightforward to calculate the total dust mass of the galaxies. After inspection of these dust maps, no real dust structures could be identified outside the main dust lane. It was therefore assumed that this dust lane contains almost all the interstellar dust in these galaxies. The amount of dust outside the dust lane is not visible through extinction in the optical, which could mean
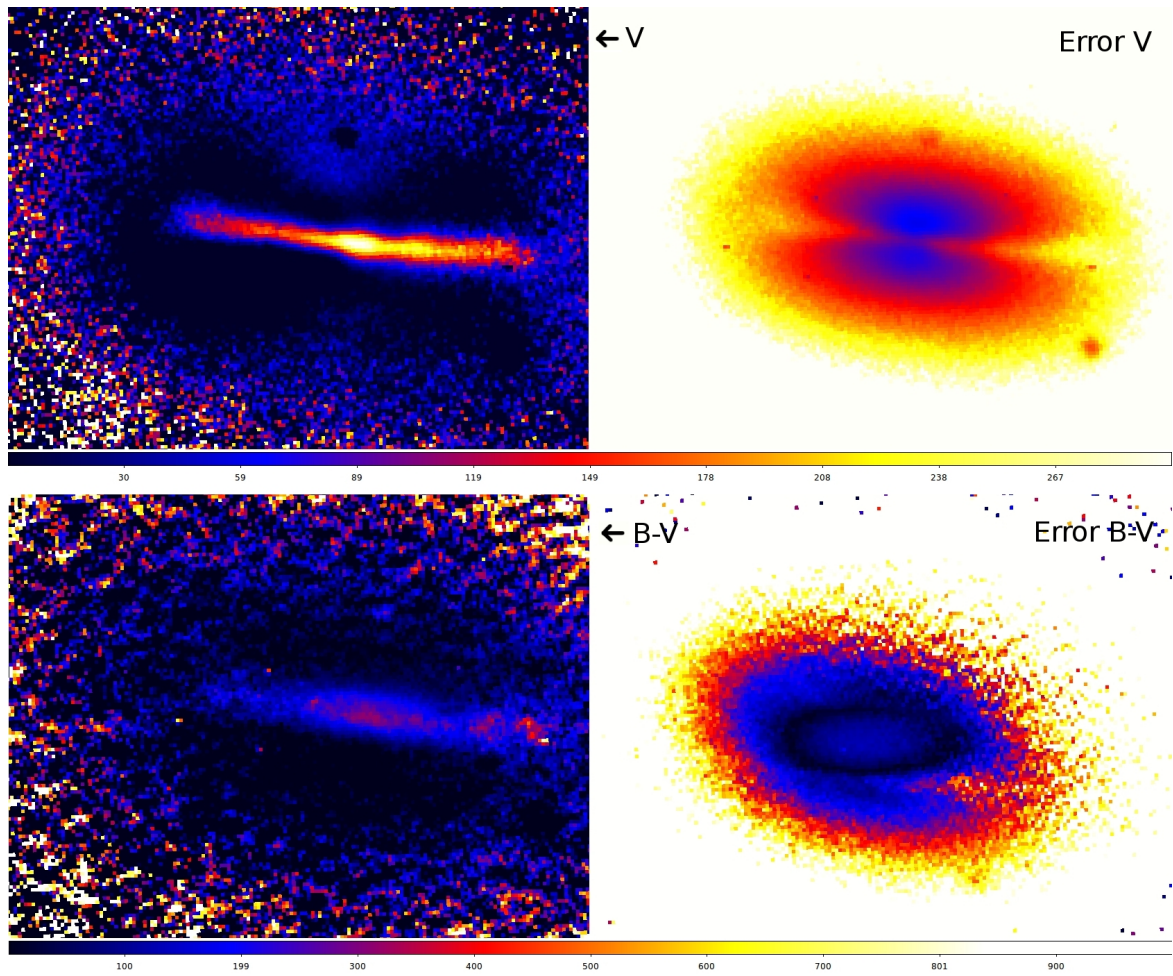
Figure 6.13: Top: dust map and error map of NGC 4370 derived from its V band image. Bottom: B-V colour dust map and the corresponding error maps for the same galaxy.

there is only a negligible amount of dust present in these regions. Another explanation is the presence of clumpy structures outside the dust lane (de Looze et al. 2012). These 'halo' dust structures should be compact and will not contribute to the extinction. This should become clear once the Herschel images are available, but for now it was assumed that these structures do not add significantly to the total dust mass.

6.4.1   Polygon regions of the dust lane and total masses

To quantify the total dust mass, the spatial extent of the dust lane must be determined for each galaxy. This was done by inspecting a high contrast image of the dust map in a well chosen wavelength band. Given the quality variations of the different wavelength bands, the dust lane may be more prominent in one image compared to the other. Because of the high SNR of the V band images and the fact that dust extinction works well at this wavelength, it was chosen to define the spatial boundaries of the dust lane from the V band images. In the case of NGC 2534, for which no V band imaging was done, the B band image was used. The defined region was also used to determine the extent of the dust lane in the colour dust maps, which allowed for better comparison between the two approaches. Figure 6.14 shows the different wavelength bands for NGC 4370. The dust lane is enclosed in a polygon region defined from the V band image. This region also encloses the dust lane in all other wavelength bands, making it possible to derive the total dust mass for each wavelength band and comparing them in a consistent way.

An IDL routine was written to extract the pixel values and their corresponding errors out of this polygon region and write them to a list. Several pixel values, extracted from the edges of the polygon region, had negative values and huge errors. Negative masses are obviously non-physical and these pixels were therefore removed from the list. To make a decent estimate of the uncertainty on the total mass, the list of good pixels and their uncertainties was exported to a self-written Python routine which performed a bootstrapping error analysis and calculated the average total mass and the uncertainty of this value. The bootstrapping method used the normalvariate function of Pythons random generator (Murray 2012) to create perturbed sets of pixel values. A thousand iterations were done for each total dust mass computation. The resulting values were stored and plotted against their respective wavelengths, see figure 6.15. The best fitting constant line to these total mass points was considered as the actual total mass for this dust model. As an estimation for the uncertainty of this fitted value, the maximum upper and lower masses were compared to the fit and their difference was used as maximum upper and lower errors. Table 6.3 lists the derived masses for each of the wavelengths and colours of all the galaxies. Similar fits as the one in figure 6.15 can be
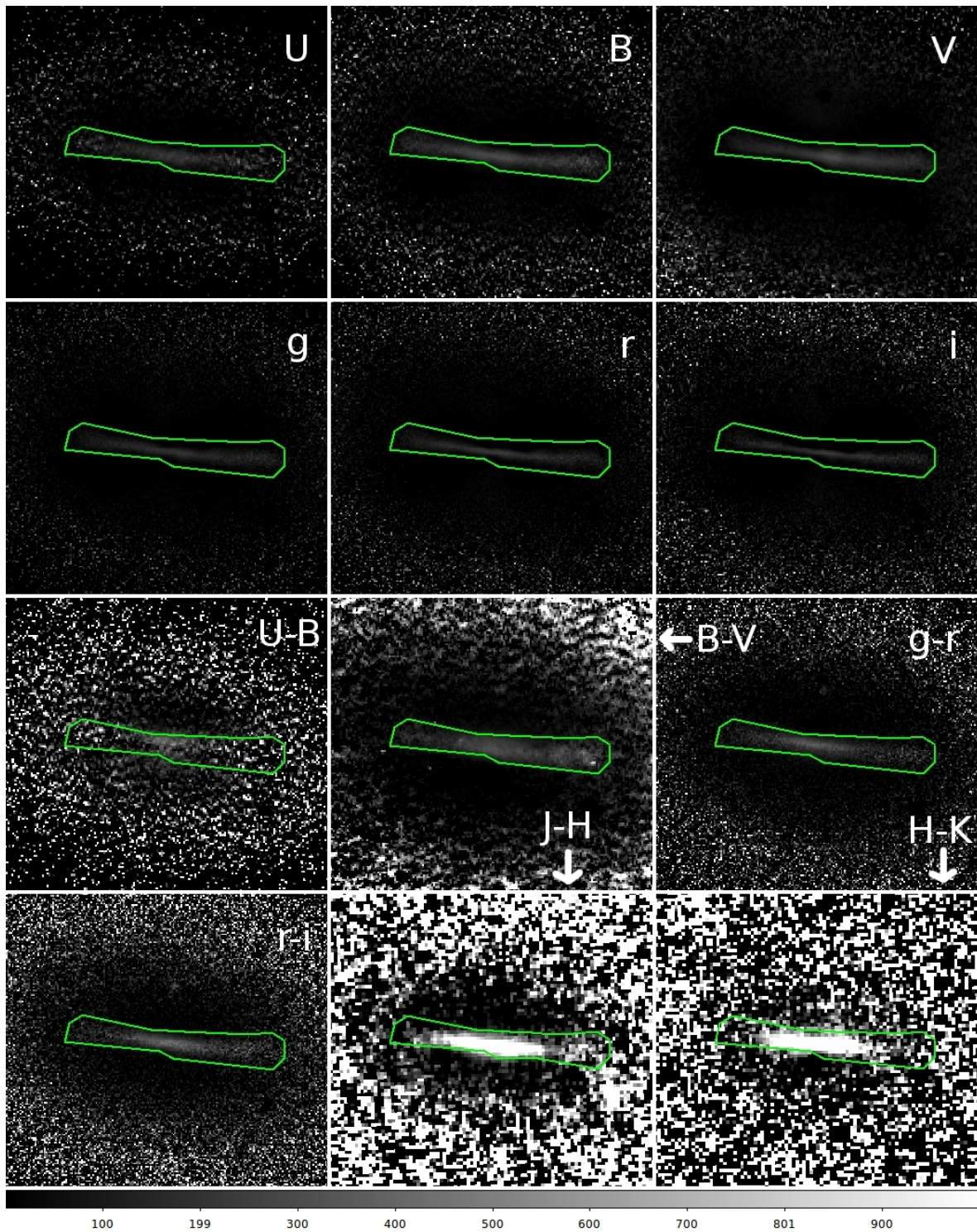
Figure 6.14: Top six panels: dust maps for NGC 4370 from the MGE models. The dust lane is clearly visible and the noise around it is fairly low. Bottom six panels: dust maps for the same galaxy from the colour maps. The dust lane is still quite clearly visible, but there is but more noise around it. The green regions are the same polygon, based on the spatial extent of the V band dust lane.
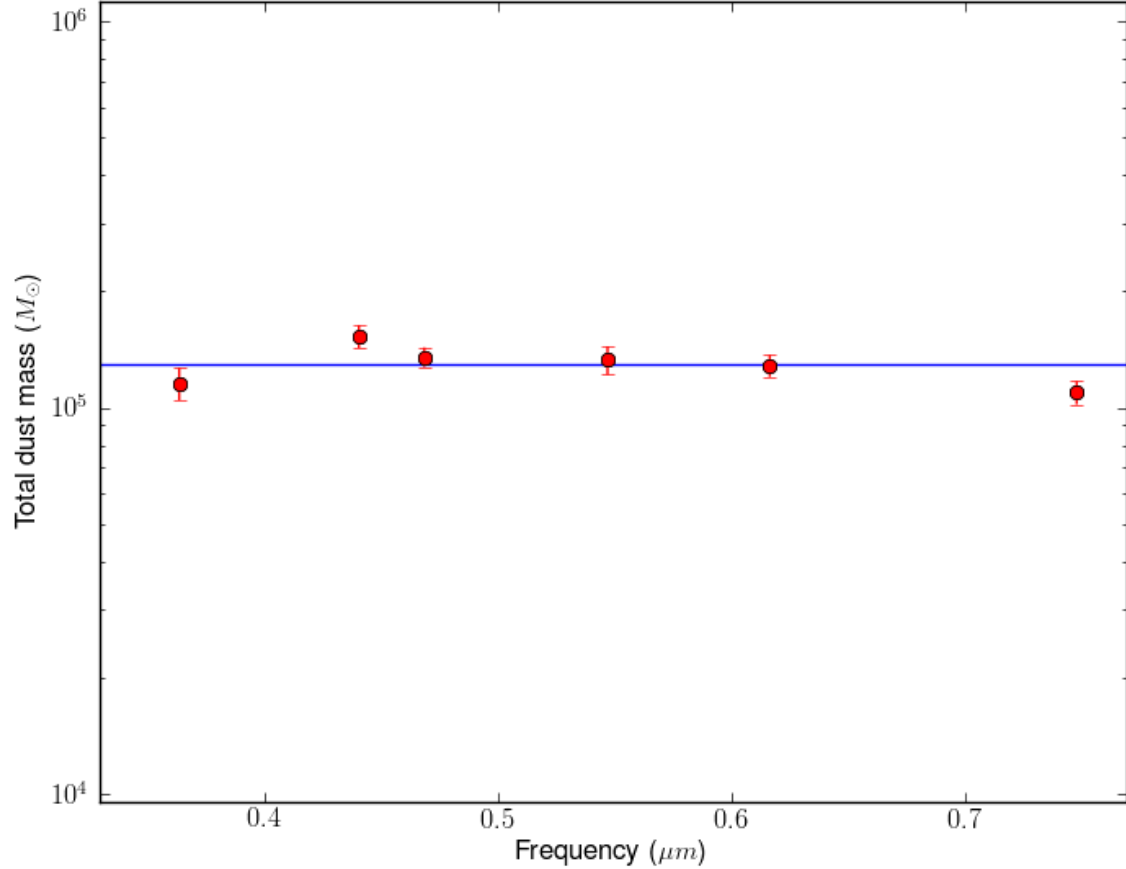
Figure 6.15: Total dust masses of NGC 4370 for each wavelength band, based on the MGE models. In blue is the best fitting constant line for these values. This was considered to be the general total dust mass, in this case $(1.29 \pm 0.16) \times 10^5 \, M_\odot$.

found in appendix B.3.

6.4.2 Dust masses from FIR emission

Interstellar dust re-emits the starlight in the far-infrared and submm regions, making it visible for the Herschel and IRAS space telescopes. FIR fluxes can be used to derive the total mass in dust, based on some assumed dust properties. Hildebrand (1983) used the following relation to convert IRAS fluxes F_ν to dust mass:

$$M_d = \frac{4}{3} a \rho_d D^2 \frac{F_\nu}{Q_\nu B_\nu(T_d)}, \tag{6.27}$$

where a is the grain radius, ρ_d the specific grain mass density, D the distance to the galaxy and Q_ν the emissivity of the dust grains. $B_\nu(T_d)$ is the Planck function of temperature $T_d = (S_{60}/S_{100})^{0.4}$ (Young et al. 1989). Finkelman et al. (2010) used this technique to derive dust masses from IRAS fluxes, see table 6.4. For NGC 2534, NGC 3665

Band/colour	Total dust mass ($\log\left(M/M_\odot\right)$)				
	NGC 2534	NGC 3665	NGC 4370	NGC 5485	NGC 5525
U	5.90 ± 0.06	5.38 ± 0.03	5.06 ± 0.04	5.06 ± 0.05	6.52 ± 0.04
B	5.85 ± 0.03	5.45 ± 0.02	5.19 ± 0.03	5.16 ± 0.04	6.52 ± 0.02
V	n/a	5.53 ± 0.02	5.12 ± 0.04	5.11 ± 0.04	6.39 ± 0.03
g	5.78 ± 0.03	5.55 ± 0.02	5.13 ± 0.03	5.19 ± 0.03	6.42 ± 0.02
r	5.80 ± 0.03	5.64 ± 0.02	5.11 ± 0.03	5.18 ± 0.03	6.53 ± 0.02
I	5.79 ± 0.03	5.68 ± 0.02	5.04 ± 0.03	5.17 ± 0.03	6.48 ± 0.02
Fit	$5.83^{+0.15}_{-0.02}$	$5.55^{+0.17}_{-0.12}$	$5.11^{+0.12}_{-0.04}$	$5.15^{+0.08}_{-0.04}$	$6.48^{+0.08}_{-0.06}$
U-B	5.86 ± 0.04	5.30 ± 0.04	5.43 ± 0.06	5.37 ± 0.04	6.89 ± 0.06
B-V	5.80 ± 0.08	5.55 ± 0.05	5.35 ± 0.03	5.27 ± 0.03	6.38 ± 0.04
G-r	5.86 ± 0.03	5.64 ± 0.02	5.40 ± 0.02	5.37 ± 0.02	6.40 ± 0.03
R-i	5.81 ± 0.03	5.60 ± 0.02	5.48 ± 0.02	5.39 ± 0.03	6.58 ± 0.03
B-i	5.75 ± 0.03	5.56 ± 0.03	5.40 ± 0.02	5.32 ± 0.02	6.25 ± 0.04
J-H	5.82 ± 0.10	5.70 ± 0.06	5.48 ± 0.05	5.13 ± 0.09	6.95 ± 0.03
H-K	5.49 ± 0.06	5.98 ± 0.08	5.53 ± 0.04	4.90 ± 0.13	6.84 ± 0.02
Fit	$5.82^{+0.09}_{-0.04}$	$5.61^{+0.18}_{-0.20}$	$5.43^{+0.11}_{-0.04}$	$5.32^{+0.11}_{-0.09}$	$6.42^{+0.24}_{-0.11}$

Table 6.3: Overview of the total mass in dust from optical extinction effects. Top part of the table lists the masses from MGE modelling for each wavelength band. The bottom part lists the masses from colour maps. The general total mass was calculated by performing a least squares fit of a constant value to the separate masses.

Galaxy	IRAS/Herschel $(\log(M_{FIR}/M_\odot))$	Literature, optical $(\log(M_{Optical}/M_\odot))$	This work, MGE $(\log(M_{Optical}/M_\odot))$	This work, colour $(\log(M_{Optical}/M_\odot))$
NGC 2534	4.79 ± 0.86	4.98 ± 0.24	$5.83^{+0.15}_{-0.02}$	$5.82^{+0.09}_{-0.04}$
NGC 3665	6.22 ± 0.08	5.04 ± 0.03	$5.55^{+0.17}_{-0.12}$	$5.61^{+0.18}_{-0.20}$
NGC 4370	$6.51^{+0.03}_{-0.02}$	4.57 ± 0.02	$5.11^{+0.12}_{-0.04}$	$5.43^{+0.11}_{-0.04}$
NGC 5485	5.86 ± 0.28	5.86 ± 0.28	$5.15^{+0.08}_{-0.04}$	$5.32^{+0.11}_{-0.09}$
NGC 5525[1]	n/a	5.99 ± 0.10	$6.48^{+0.08}_{-0.06}$	$6.42^{+0.24}_{-0.11}$

Table 6.4: Overview of the literature (Finkelman et al. 2010) FIR and optical dust masses for the five galaxies. To compare, the optical dust mass from our two models are also displayed. The general trend is that our dust mass estimates lie between the literature's optical values and the FIR-based mass estimates.

[1] The literature optical dust mass for this galaxy was obtained from Patil et al. (2007).

and NGC 5485, these are currently the best FIR mass estimations. For NGC 5525, no FIR data were found. FIR masses will be derived in the near future from Herschel PACS and SPIRE fluxes. These data are already available for NGC 4370, which was observed in the Herschel Virgo Cluster Survey (Davies et al. 2010) in both PACS and SPIRE. Figure 6.16 shows the FIR images in Herschel's PACS (100 and 160 μm) and SPIRE (250, 350 and 500 μm) bands. These observations were considered to be more accurate then IRAS and so for this galaxy, the dust mass from FIR emission was derived from these Herschel fluxes. Figure 6.17 shows a modified black body fit to the Herschel data, from which the dust mass could be derived using 6.27. Modified black body (or grey body) models are commonly used to fit emission from interstellar dust (Dunne et al. 2000; Hildebrand 1983). A modified black body consists out of a regular Planck function $B_\nu(T_d)$ with an extra factor $Q_{em} \propto \nu^\beta$, which incorporates additional dust emission. Hildebrand (1983) derived that the emissivity index β should lie between 1 and 2, depending on the dust model. In this case, a value of $\beta = 2.0$ was used, yielding a dust temperature of 21.8 K and a total dust mass of $3.14 \times 10^6 M_\odot$.

The general trend is that the mass estimates from this work lie in between the mass estimates from optical extinction in the literature and the FIR mass estimates. However, it should be noted that different distances to the galaxies were used here, see table 1.3. If a galaxy is further away, the derived dust mass will be much higher for a galaxy at closer distance but with the same flux.

6.4.3 Discussion

Figure 6.18 shows a plot of the total dust mass for each galaxy, using the three different methods: Multi-Gaussian Expansion fitting, colour index maps and far-infrared flux conversion. The first two techniques agree for most of the galaxies within the 3-σ error
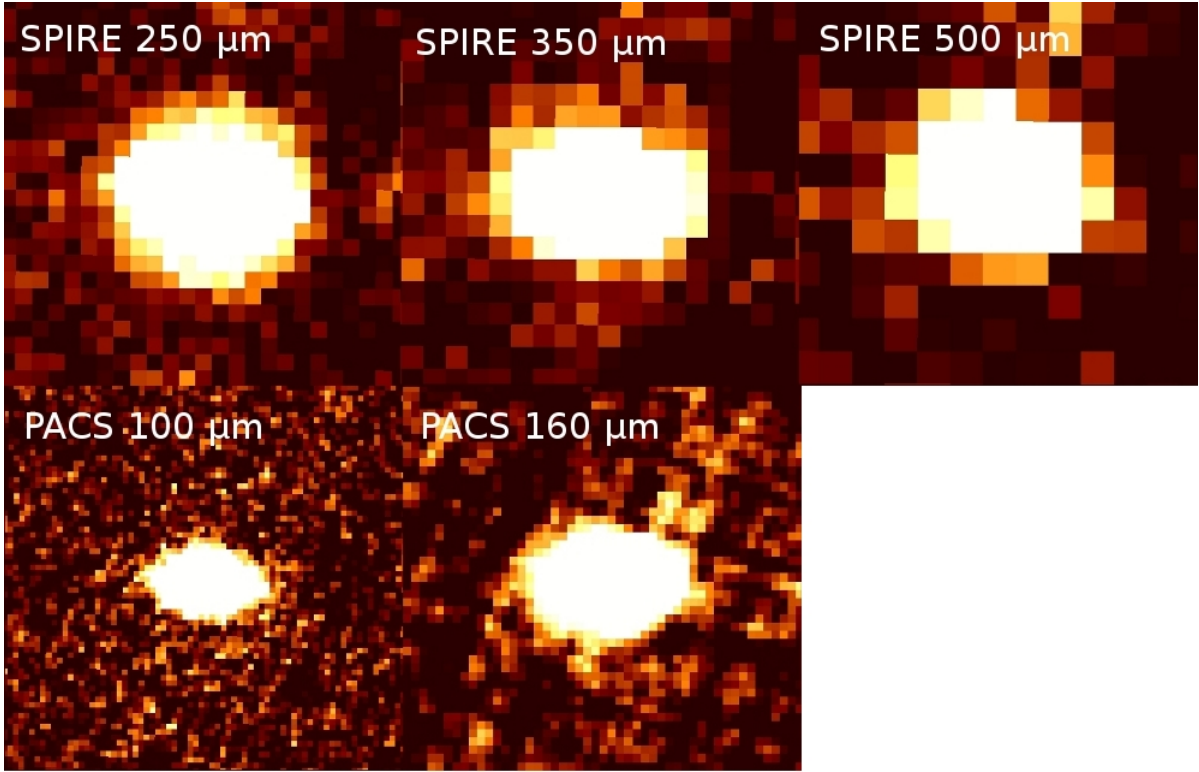
Figure 6.16: FIR observations of NGC 4370 in the five Herschel wavelength bands. The images were extracted from the HeViCS public data archive (Davies et al. 2010).
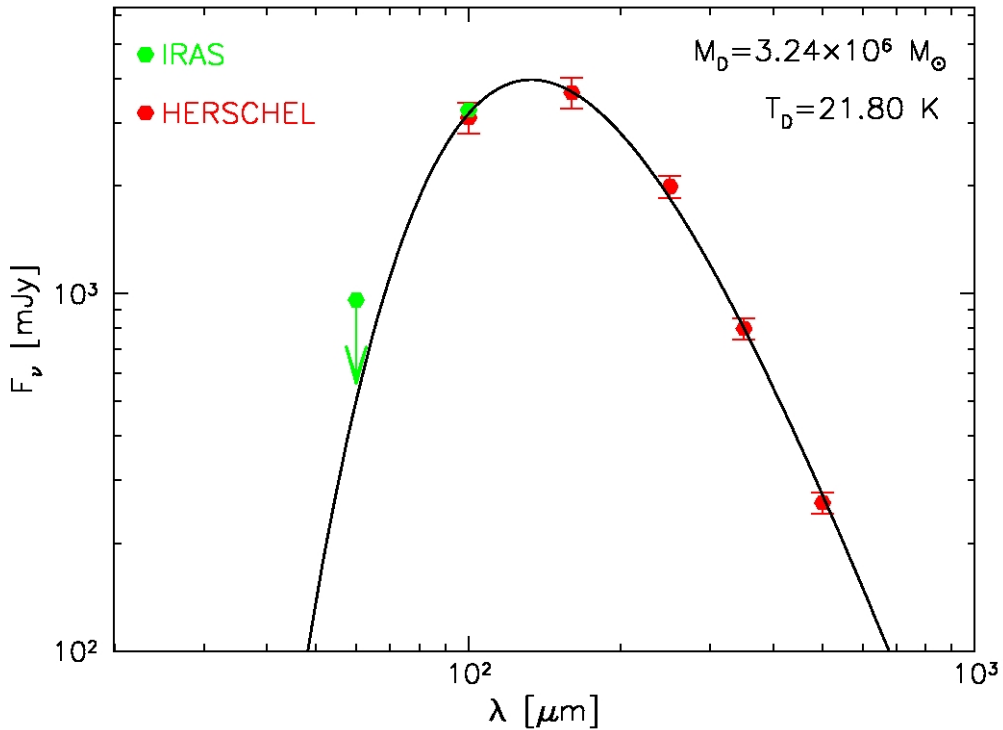
Figure 6.17: Black body fit to the Herschel PACS and SPIRE fluxes of NGC 4370. The temperature of the black body was derived to be $T_d = 21.80^{+0.41}_{-0.46}$ K and the total dust mass $6.51^{+0.03}_{-0.02}$.
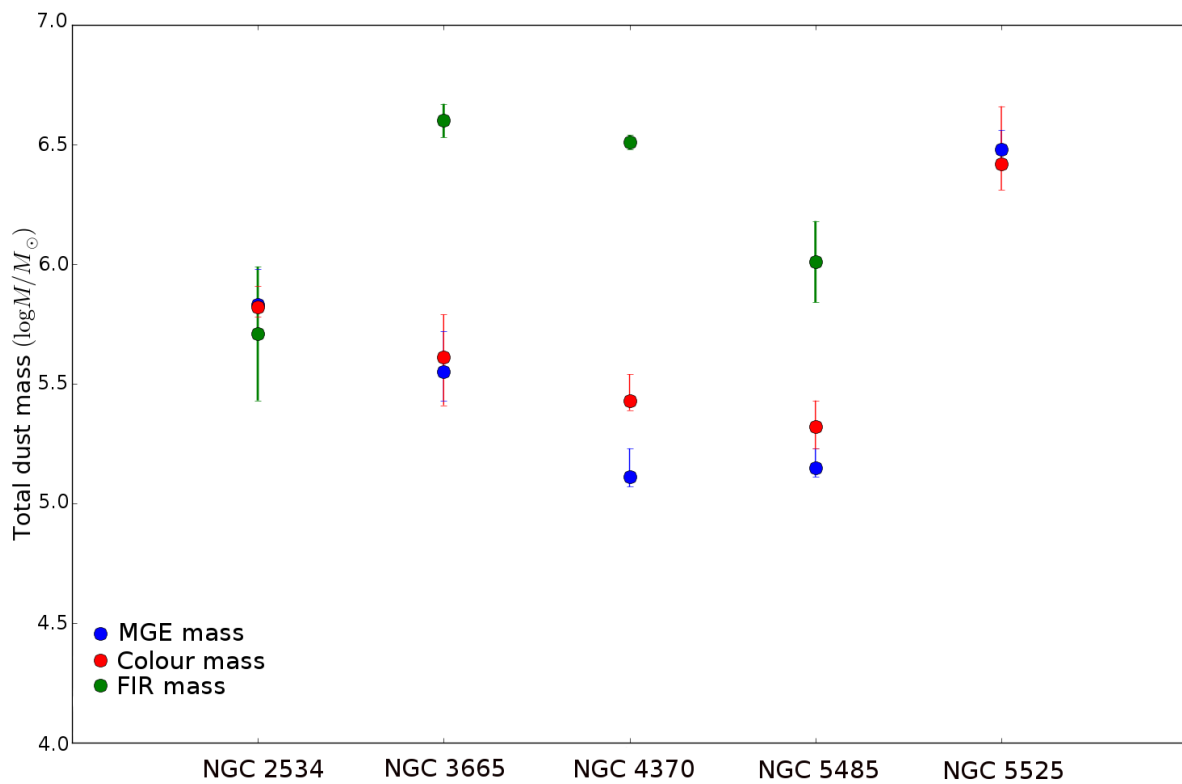
Figure 6.18: Overview of the total dust mass estimations for each of the used methods. MGE and colour masses were obtained from optical and NIR data, while the FIR masses were derived from IRAS fluxes (NGC 2534, NGC 3665, NGC 5485) and Herschel PACS and SPIRE data (NGC 4370). No FIR data was available yet for NGC 5525.

bars. Generally, the dust mass estimation from colour maps is slightly higher than the MGE modelling. There is only a significant discrepancy in dust mass for NGC 4370. This could be caused by a various range of factors, like the definition of a suitable polygon region for the dust lane, positive noise which was falsely counted as dust, inconsistencies in the colour difference maps or even seeing related effects. In any case, it is probably so that the uncertainty of the total mass should be larger then it is now. It is however quite difficult if not impossible to estimate the uncertainty on certain steps throughout the process. Nevertheless, the difference between the two techniques is 'only' a factor 2 and both dust mass estimates yield the same order of magnitude. More obvious is the difference between dust masses from optical extinction (MGE, colour masses) and the masses from FIR emission. Often, the latter are an order of magnitude higher than the former. Needless to say, something more than a low error estimation is behind this discrepancy. Turning back to the assumed dust distribution to convert attenuation to optical depth (equation 6.16) it must be kept in mind that this thin slab of dust only yields minimum dust masses to explain given attenuations. As mentioned before, this model does not apply for the case of inclined elliptical galaxies with thin dust lanes. For this type of objects, a distribution with a fraction p of foreground emission as described by 6.18 might give better results. In fact, it is possible to derive the value of the parameter p for each galaxy by iteratively varying this parameter until $M_{optical} = M_{FIR}$.

This method, however does not incorporate clumpy dust structures which are thought to be the cause of the energy balance problem in edge-on spiral galaxies (see the discussion in section 1.1). In fact, by applying the above method, the fraction of foreground emission will probably be overestimated. A full study of the energy balance problem in all regions of the galaxies requires advanced modelling like 3-D panchromatic radiative transfer and will be the future of the FRIEDL project.

Summary

<div style="text-align: right;">7</div>

*Astronomy? Impossible to understand
and madness to investigate.*

Sophocles

This work reports the acquisition and reduction of optical and near-infrared data of both edge-on spiral galaxies and early-type galaxies with prominent dust lanes. The first part covers the various observing runs which provided the data. Edge-on spiral galaxies were observed by the author at the observatory of Skinakas in Greece with the 1.3 m telescope. The observed objects are part of several larger efforts, including the HEROES and NHEMESES projects. Data reduction and calibration came without significant issues. Secondly, optical and near-infrared imaging of most of the NHEMESES galaxies was executed in service mode with the TNG on La Palma. Data reduction for this observing run spawned several problems, which could all be overcome and high quality science frames could be constructed. The fourth chapter covers the data reduction of NHEMESES and HEROES edge-on galaxies observed in the optical in service mode with the WHT on La Palma. Some minor calibration issues occurred but could be solved within a good accuracy. Last was a set of early-type galaxies for the FRIEDL project, which were observed by FRIEDL colleagues with the 2.1 m (near-infrared) and 1.5 m (optical) telescope on the San Pedro Martír observatory in Mexico. Calibration issues occurred here too, but could be solved as well. In short, all acquired data were successfully reduced and calibrated. An overview of the various galaxies and their corresponding projects is listed below (appendix A).

The second part of this work presents a case study of the five FRIEDL galaxies, for which optical U, B and V and NIR J, H and K data was acquired. Additionally optical g, r and i bands were obtained from the SDSS archive and added to our data to cover the entire optical to NIR region. For each galaxy, these images were used to derive the dust mass from optical extinction by using two separate methods. Method one involves the creation of colour difference maps, which can be converted to selective attenuation maps. By assuming a specific dust distribution, selective attenuations can be converted

to selective optical depths and so to dust masses. The assumed dust model here was a thin foreground screen, yielding minimum values for the dust masses. Method two consisted out of the modelling of a dust-free galaxy for each wavelength band by performing a Multi-Gaussian Expansion (MGE) fit to the dust-free regions of the galaxy. Attenuation maps could be created by subtracting the models from the original images. Using the same foreground dust model, these attenuation maps were converted to dust masses. Total dust masses were extracted from the dust maps by defining a polygon region to the dust lane and summing all the pixels inside. The total dust masses differ slightly depending on the colour or broad band image used to derive them. For each galaxy, a general total dust mass was derived from both colour maps and MGE models. These dust masses were compared to the observed dust masses from far-infrared emission from Herschel and IRAS observations and to masses found in the literature (see table 6.4).

Dust masses from colour maps and MGE models were found to lie no farther than a factor 2 apart. In general, error analysis confirms that both methods are consistent in predicting the dust mass from optical extinction. However, these masses do not agree with the literature values in some cases. The main reason for this is a difference in the used distance to the galaxies. In all cases, dust masses from optical extinction are about an order of magnitude smaller than the dust masses derived from FIR emission. Although it must be noted that we have used a simple dust model, yielding minimum dust masses, the discrepancy is quite large. The current understanding of this phenomenon is a partial mixing of the dust lane and the surrounding stars. This may mathematically be achieved by introducing a parameter p, which is the fraction of optical emission from stars in front of the dust. Additionally the existence of clumpy dust structures may also explain why more dust is visible in emission (FIR) than there is in extinction (optical).

More advanced techniques, such as pixel-to-pixel Spectral Energy Distribution (SED) fitting and 3-D radiative transfer modelling of these galaxies in combination with Herschel observations, should be able to distinguish both sources of missing dust in extinction and will allow for detailed energy balance studies.

Bibliography

Abazajian, K. N., Adelman-McCarthy, J. K., Agüeros, M. A., et al. 2009, ApJS, 182, 543

Allaert, F., Baes, M., Gentile, G., et al. 2012, Master theses

Alton, P. B., Xilouris, E. M., Misiriotis, A., Dasyra, K. M., & Dumke, M. 2004, A&A, 425, 109

Amblard, A., Cooray, A., Serra, P., et al. 2010, A&A, 518, L9

Baes, M., Fritz, J., Gadotti, D. A., et al. 2010, A&A, 518, L39

Benn, C., Dee, K., & Agócs, T. 2008, in Society of Photo-Optical Instrumentation Engineers (SPIE) Conference Series, Vol. 7014, Society of Photo-Optical Instrumentation Engineers (SPIE) Conference Series

Benn, C. R. & Ellison, S. L. 1998, New A Rev., 42, 503

Bertin, E. & Arnouts, S. 1996, A&AS, 117, 393

Bianchi, S. 2008, A&A, 490, 461

Bianchi, S. & Xilouris, E. M. 2011, A&A, 531, L11

Binney, J. 1998, Galactic astronomy (Princeton, NJ: Princeton University Press)

Brosch, N. 1988, in Dust in the Universe, ed. M. E. Bailey & D. A. Williams, 501–507

Calzetti, D., Kinney, A. L., & Storchi-Bergmann, T. 1994, ApJ, 429, 582

Cappellari, M. 2002, MNRAS, 333, 400

Cortese, L., Ciesla, L., Boselli, A., et al. 2012, A&A, 540, A52

Cruz-Gonzalez, I., Avila, R., & Tapia, M., eds. 2003, Revista Mexicana de Astronomia y Astrofisica, vol. 27, Vol. 19, San Pedro Martir : astronomical site evaluation

Cruz-González, I., Carrasco, L., Ruiz, E., et al. 1994, Rev. Mexicana Astron. Astrofis., 29, 197

Dalcanton, J. J., Yoachim, P., & Bernstein, R. A. 2004, ApJ, 608, 189

Dasyra, K. M., Xilouris, E. M., Misiriotis, A., & Kylafis, N. D. 2005, A&A, 437, 447

Davies, J. I., Baes, M., Bendo, G. J., et al. 2010, A&A, 518, L48

De Geyter, G., Baes, M., Fritz, J., Verstappen, J., & De Looze, I. 2012, in prep.

de Looze, I., Baes, M., Fritz, J., & Verstappen, J. 2012, MNRAS, 419, 895

Draine, B. T. 2003, ARA&A, 41, 241

Draine, B. T. & Lee, H. M. 1984, ApJ, 285, 89

Draper, P. W., Berry, D. S., Jenness, T., & Economou, F. 2009, in Astronomical Society of the Pacific Conference Series, Vol. 411, Astronomical Data Analysis Software and Systems XVIII, ed. D. A. Bohlender, D. Durand, & P. Dowler, 575

Dunne, L., Eales, S., Edmunds, M., et al. 2000, MNRAS, 315, 115

Emsellem, E., Monnet, G., & Bacon, R. 1994, A&A, 285, 723

ENO. 2012, TNG Telescope Web Page, http://www.tng.iac.es

ESA. 2012, Herschel Space Observatory, www.esa.int/herschel

ESO. 2012, The ESO-MIDAS environment, version 11FEB, https://www.eso.org/sci/software/esomidas/news/11feb_pl1_3.html

Finkelman, I., Brosch, N., Funes, J. G., et al. 2012, MNRAS, 422, 1384

Finkelman, I., Brosch, N., Funes, J. G., Kniazev, A. Y., & Väisänen, P. 2010, MNRAS, 407, 2475

Finkelman, I., Brosch, N., Kniazev, A. Y., et al. 2008, MNRAS, 390, 969

Gordon, K. D., Galliano, F., Hony, S., et al. 2010, A&A, 518, L89

Goudfrooij, P., Hansen, L., Jorgensen, H. E., & Norgaard-Nielsen, H. U. 1994, A&AS, 105, 341

Greisen, E. W. & Calabretta, M. R. 2002, A&A, 395, 1061

Griffin, M. J., Abergel, A., Abreu, A., et al. 2010, A&A, 518, L3

Gunn, P. 2001, SDSS document

Hawarden, T. G., Longmore, A. J., Tritton, S. B., Elson, R. A. W., & Corwin, Jr., H. G. 1981, MNRAS, 196, 747

Hildebrand, R. H. 1983, QJRAS, 24, 267

Holwerda, B. W., Bianchi, S., Baes, M., et al. 2011, ArXiv e-prints

ING. 2012, William Herschel Telescope, http://www.ing.iac.es/astronomy/telescopes/wht/

ITTvis. 2012, The Interactive Data Language, http:www.ittvis.com

Jacob, J. C., Katz, D. S., Berriman, G. B., et al. 2010, in Astrophysics Source Code Library, record ascl:1010.036, 10036

Jester, S., Schneider, D. P., Richards, G. T., et al. 2005, AJ, 130, 873

Knapen, J. H., Hes, R., Beckman, J. E., & Peletier, R. F. 1991, A&A, 241, 42

Kylafis, N. D. & Bahcall, J. N. 1987, ApJ, 317, 637

Landolt, A. U. 1992, AJ, 104, 340

Landsman, W. B. 1989, in Bulletin of the American Astronomical Society, Vol. 21, Bulletin of the American Astronomical Society, 784

Lawson, C. 1995, Solving least squares problems (Philadelphia: SIAM)

MacLachlan, J. M., Matthews, L. D., Wood, K., & Gallagher, J. S. 2011, ApJ, 741, 6

Makovoz, D. & Khan, I. 2005, in Astronomical Society of the Pacific Conference Series, Vol. 347, Astronomical Data Analysis Software and Systems XIV, ed. P. Shopbell, M. Britton, & R. Ebert, 81

Mannucci, F. 2012, Speedy Near-IR data Automatic reduction Pipeline (SNAP), http://www.arcetri.astro.it/~filippo/snap/

Misiriotis, A., Popescu, C. C., Tuffs, R., & Kylafis, N. D. 2001, A&A, 372, 775

Murray, D. 2012, Pythons Random Generator, http://docs.python.org/library/random.html

NAO. 2012, National Astronomical Observatory of SPM, http://www.astrossp.unam.mx/indexspm.html

NASA-GSFC. 2012, The IDL Astronomy User's Library, http://idlastro.gsfc.nasa.gov/

NOAO. 2012, The IRAF environment, version 2.14, http://iraf.noao.edu/

Patil, M. K., Pandey, S. K., Sahu, D. K., & Kembhavi, A. 2007, A&A, 461, 103

Patsis, P. A. & Xilouris, E. M. 2006, MNRAS, 366, 1121

Pence, W. D., Chiappetti, L., Page, C. G., Shaw, R. A., & Stobie, E. 2010, A&A, 524, A42

Poglitsch, A., Waelkens, C., Geis, N., et al. 2010, A&A, 518, L2

Popescu, C. C., Misiriotis, A., Kylafis, N. D., Tuffs, R. J., & Fischera, J. 2000, A&A, 362, 138

Popescu, C. C., Tuffs, R. J., Dopita, M. A., et al. 2011, A&A, 527, A109

Roeser, S., Demleitner, M., & Schilbach, E. 2010, AJ, 139, 2440

Sadler, E. M. & Gerhard, O. E. 1985, MNRAS, 214, 177

SITe inc. 1995, Camera characteristics document

Skrutskie, M. F., Cutri, R. M., Stiening, R., et al. 2006, AJ, 131, 1163

Smith, J. A., Tucker, D. L., Kent, S., et al. 2002, AJ, 123, 2121

UOC. 2012, Skinakas Observatory, http://skinakas.physics.uoc.gr

Varosi, F. & Landsman, W. B. 1993, in Astronomical Society of the Pacific Conference Series, Vol. 52, Astronomical Data Analysis Software and Systems II, ed. R. J. Hanisch, R. J. V. Brissenden, & J. Barnes, 515

Verstappen, J., Baes, M., Fritz, J., De Looze, I., & De Geyter, G. 2012, in prep.

Walterbos, R. A. M. & Kennicutt, Jr., R. C. 1988, A&A, 198, 61

Xilouris, E. M., Byun, Y. I., Kylafis, N. D., Paleologou, E. V., & Papamastorakis, J. 1999, A&A, 344, 868

York, D. G., Adelman, J., Anderson, Jr., J. E., et al. 2000, AJ, 120, 1579

Young, J. S., Xie, S., Kenney, J. D. P., & Rice, W. L. 1989, ApJS, 70, 699

Zacharias, N., Monet, D. G., Levine, S. E., et al. 2004, in Bulletin of the American Astronomical Society, Vol. 36, American Astronomical Society Meeting Abstracts, 1418

Zubko, V., Dwek, E., & Arendt, R. G. 2004, ApJS, 152, 211

A

Overview of the dataset

A.1   List of the galaxies

Name	RA (J2000)	DEC (J2000)	U	B	V
FRIEDL					
NGC2534	08:12:54.1	+55:40:19.0	1200	600	
			2.26	2.79	
NGC2907	09:31:36.7	−16:44:05.0			
NGC3283	10:31:11.6	−46:15:05.0			
NGC3497	11:07:18.1	−19:28:18.0			
NGC3665	11:24:43.7	+38:45:46.0	2400	1800	1200
			2.59	2.43	3.15
NGC4370	12:24:54.9	+07:26:42.0	2400	1800	1500
			2.15	2.05	2.52
NGC5485	14:07:11.3	+55:00:06.0	3600	1800	600
			1.95	2.00	2.07
NGC5525	14:15:39.2	+14:16:57.0	3600	1800	600
			1.94	1.73	1.55
NGC5626	14:29:49.1	−29:44:54.0			
NGC5799	15:05:35.2	−72:25:58.0			
NGC5866	15:06:29.5	+55:45:48.0			

Table A.1: Overview of the FRIEDL data used in this work The purple colour represents the SPM telescope. All seeing values are in arcseconds.

Name	RA (J2000)	DEC (J2000)	U	B	V	R	J	K	u	g	r	I	z
NHEMESIS													
IC2233	08:13:58.9	+45:44:32.0			750			2875	6000				
					1.29			1.14	1.17				
NGC3501	11:02:47.3	+17:59:22.0											
NGC4144	12:09:58.6	+46:27:26.0			750			3105	4800				
					1.40			1.06	1.20				
NGC4183	12:13:16.9	+43:41:55.0			750			3105	4800				
					1.34			1.69	1.87				
NGC4206	12:15:16.8	+13:01:26.0											
NGC4244	12:17:29.6	+37:48:26.0			750			3105					
					1.37			1.44					
UGC7321	12:17:34.0	+22:32:25.0			750			3105					
					1.60			0.99					
NGC4460	12:28:45.5	+44:51:51.0			750			3105	4800				
					1.81			1.43	1.53				
NGC4526	12:34:03.0	+07:41:57.0											
NGC4634	12:42:40.9	+14:17:44.9											
NGC5023	13:12:12.6	+44:02:28.0		3600	1800 + 750	1800		2875					
				2.03	2.25 / 1.14	2.24		1.08					
NGC5746	14:15:34.1	+36:13:36.0											

Table A.2: Overview of the NHEMESES data used in this work. The colours represent different telescopes: blue = Skinakas, red = TNG and green = WHT. All seeing values are in arcseconds.

Name	RA (J2000)	DEC (J2000)	U	B	V	R	J	K	u	g	r	I	z
HEROES													
UGC2048	02:34:20.1	+32:30:20.0		9000 / 1.72	5400+750 / 1.58 / 1.52	3600 / 1.55		2880 / 1.13	4800 / 1.15	3600 / 1.77	1500 / 1.72	3600 / 1.41	1740 / 1.32
UGC4277	08:13:57.2	+52:38:54.0							4800 / 1.66	3600 / 1.47	1200 / 1.51	3600 / 1.13	2700 / 1.13
IC2531	09:59:55.8	-29:37:01.0											
NGC4013	11:58:31.4	+43:56:48.0											
NGC4217	12:15:50.9	+47:05:30.0											
NGC5529	14:15:34.1	+36:13:36.0		3600 / 1.55	1800 / 1.90	1800 / 1.82	2025 / 1.05						
NGC5907	15:15:53.8	+56:19:44.0		12600 / 2.12	5400 + 750 / 1.80 / 1.52	3600 / 1.92		3105 / 1.21					
Other													
NGC0128	00:29:15.0	+02:51:51.0			5400 / 1.54								
NGC0891a	02:22:33.4	+42:20:47.0							4800 / 0.99	1200 / 1.24	1235 / 0.69	1260 / 1.13	1980 / 1.1
NGC0891b	02:22:33.4	+42:20:47.0							4800 / 1.49	1830 / 1.91	1280 / 1.54	1980 / 1.64	1830 / 1.41
M104	12:39:59.4	-11:37:23.0	1200 / 2.92	600 / 2.90									
NGC7332	22:37:24.5	+23:47:54.0			7200 / 1.58								

Table A.3: Overview of the data used in this work for HEROES and other projects. The colours represent different telescopes: blue = Skinakas, red = TNG, green = WHT and purple = SPM. All seeing values are in arcseconds.

Below are images of each galaxy which were acquired for this work. The galaxies are listed per observing project, though some were observed by multiple telescopes (see the tables in appendix A.1).

A.2.1   HEROES galaxies

Imaging for the Herschel Observation of Edge-on Spirals was done during observing runs at the Skinakas 1.3 m telescope (chapter 2), the Telescope Natzonale Galileo (chapter 3) and the William Herschel Telescope (chapter 4). Most of the HEROES galaxies are presented here, except for IC 2531, NGC 4013 and NGC 4217. These objects were not observed for this work.
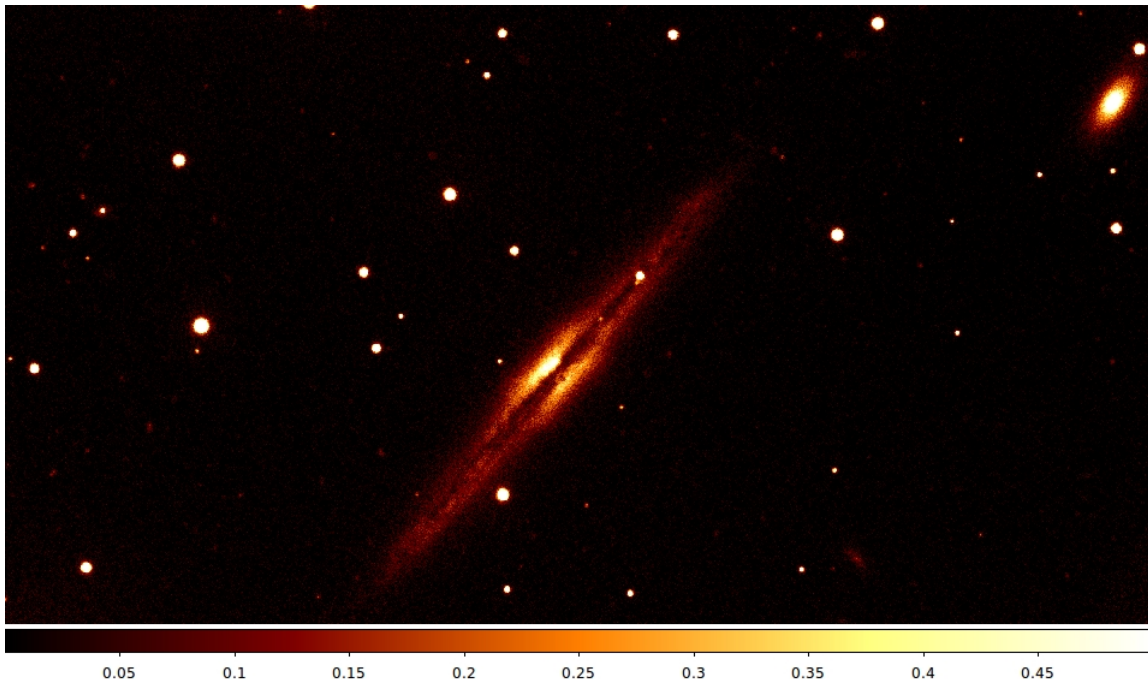
Figure A.1: Sloan u band image of UGC 2048 from 4800 seconds of exposure on the WHT.
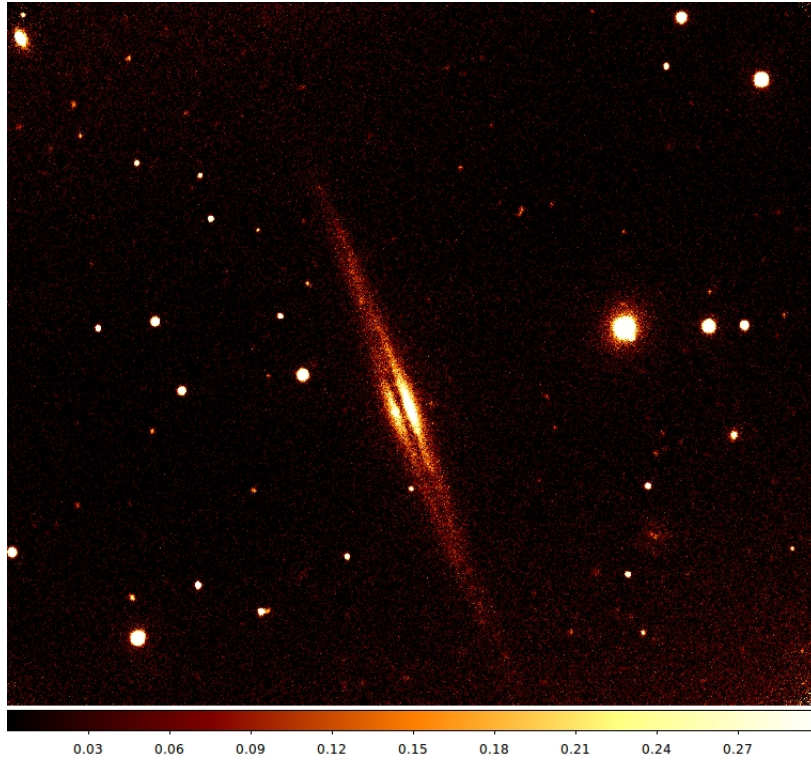
Figure A.2: Sloan u band image of UGC 4277 from 4800 seconds of exposure on the WHT.
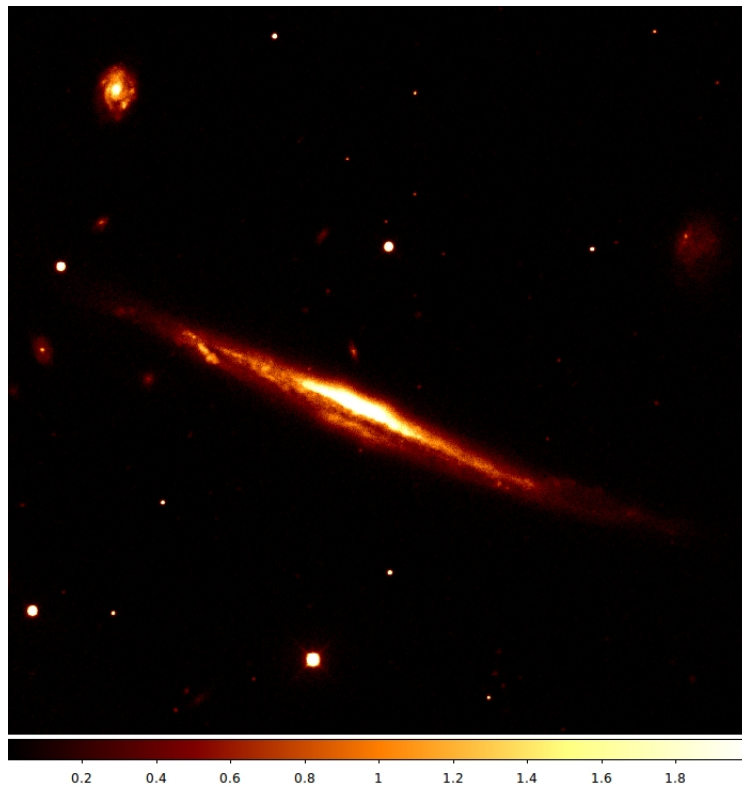
Figure A.3: B band image of NGC 5529 from 3600 seconds of exposure on the Skinakas 1.3 m telescope.
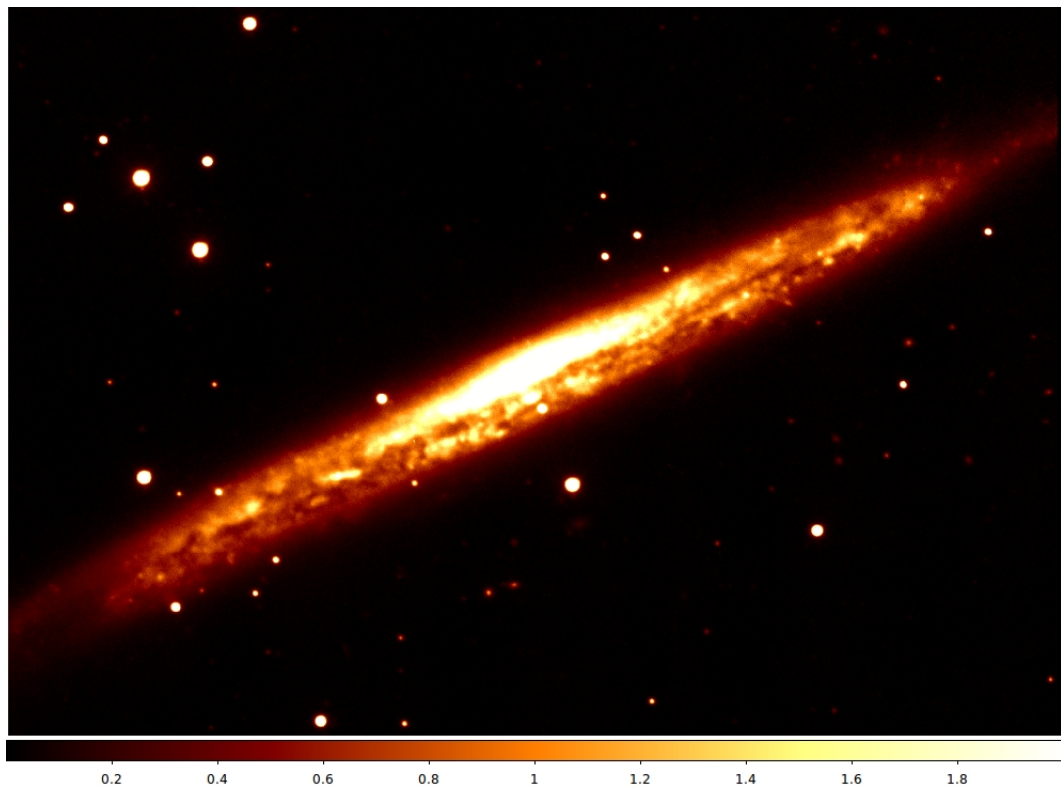
**Figure A.4:** B band image of NGC 5907 from 12600 seconds of exposure on the Skinakas 1.3 m telescope.

A.2.2   NHEMESES galaxies

Imaging for The New HErschel Multi-wavelength Extragalactic Survey of Edge-on Spirals was done during observing runs at the Skinakas 1.3 m telescope (chapter 2), the Telescope Natzonale Galileo (chapter 3) and the William Herschel Telescope (chapter 4). Most of the NHEMESES galaxies are presented here, except for NGC 3501, NGC 4206, NGC 4526, NGC 4634 and NGC 5746. These objects were not observed for this work.
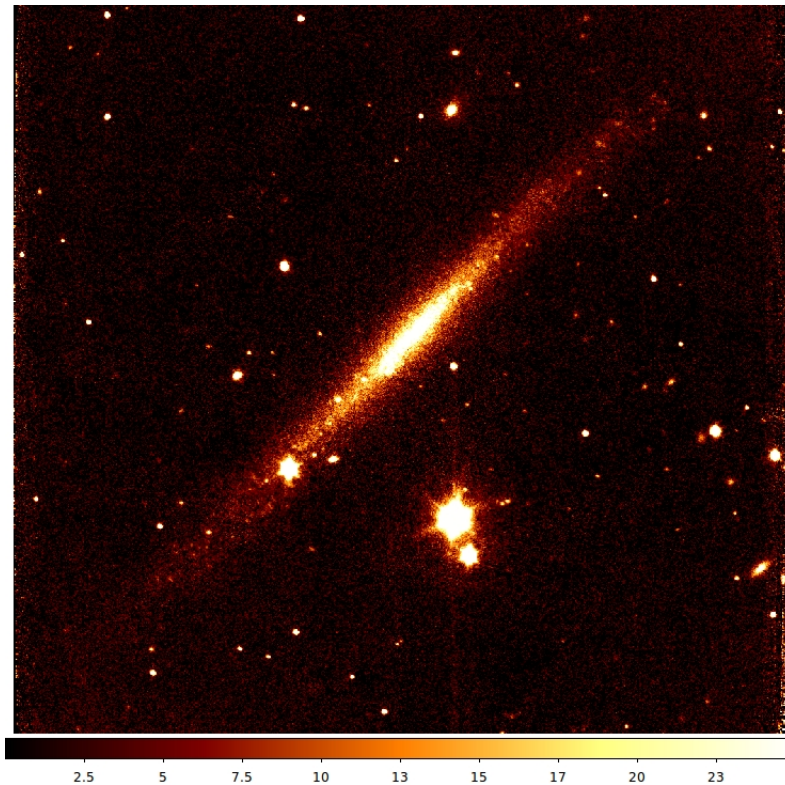
Figure A.5: K band image of IC 2233 from 2875 seconds of exposure on the TNG.
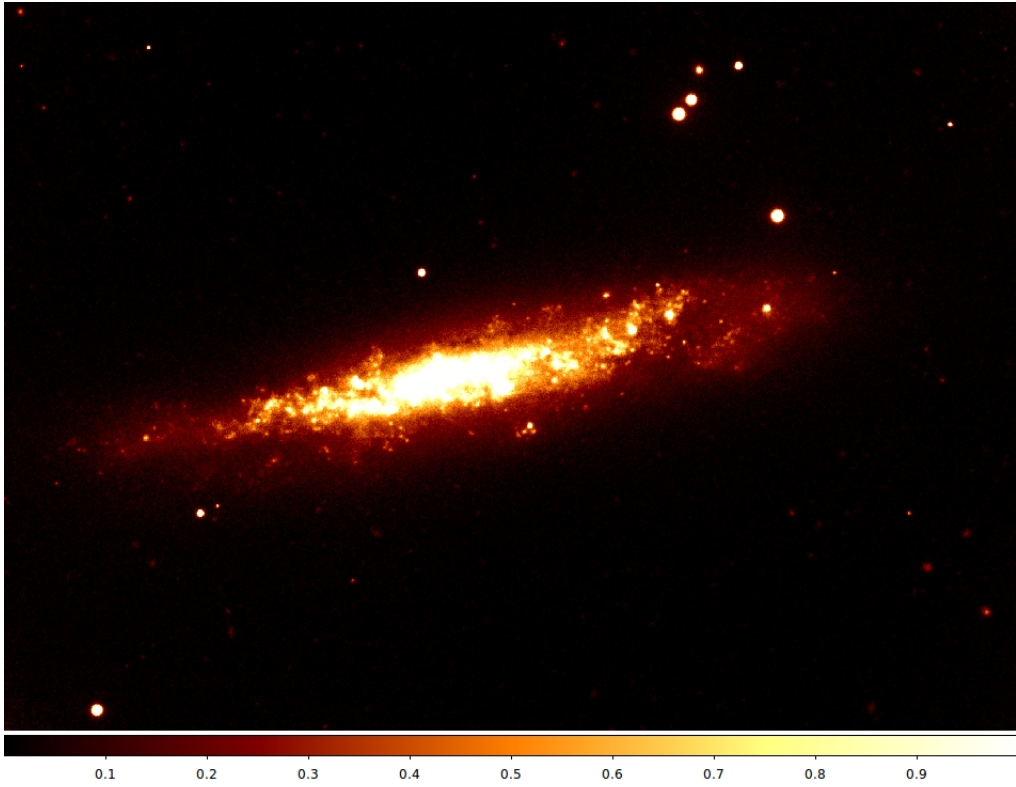
Figure A.6: Sloan u band image of NGC 4144 from 4800 seconds of exposure on the WHT.
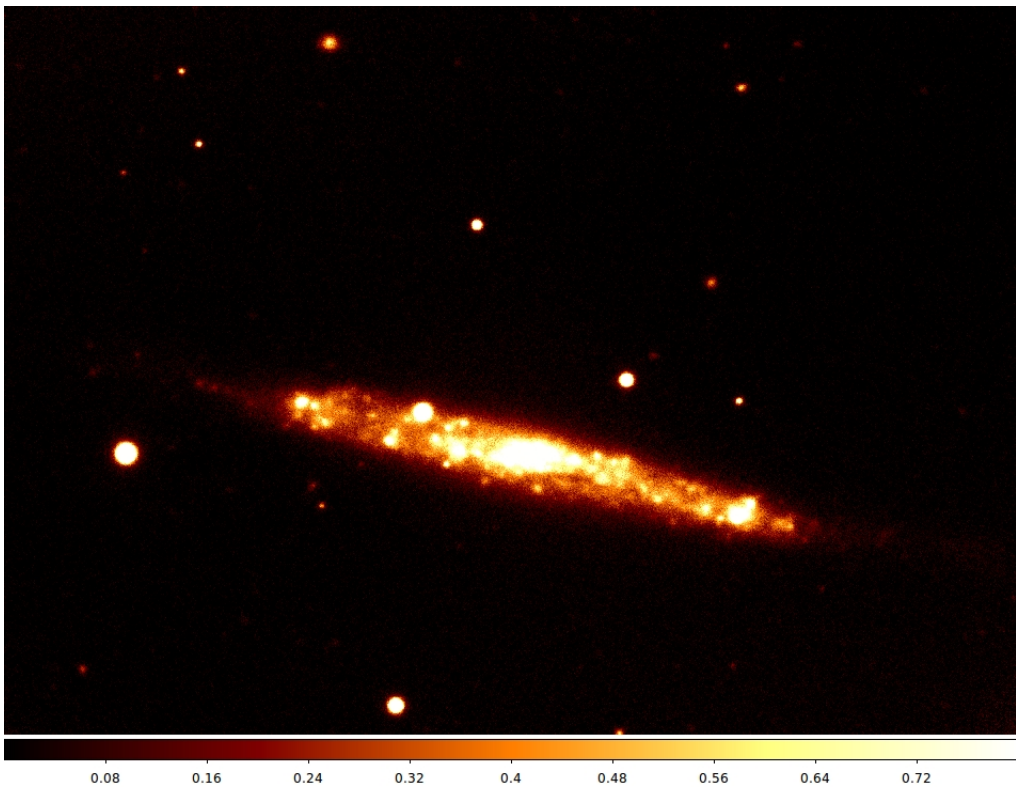
Figure A.7: Sloan u band image of NGC 4183 from 4800 seconds of exposure on the WHT.
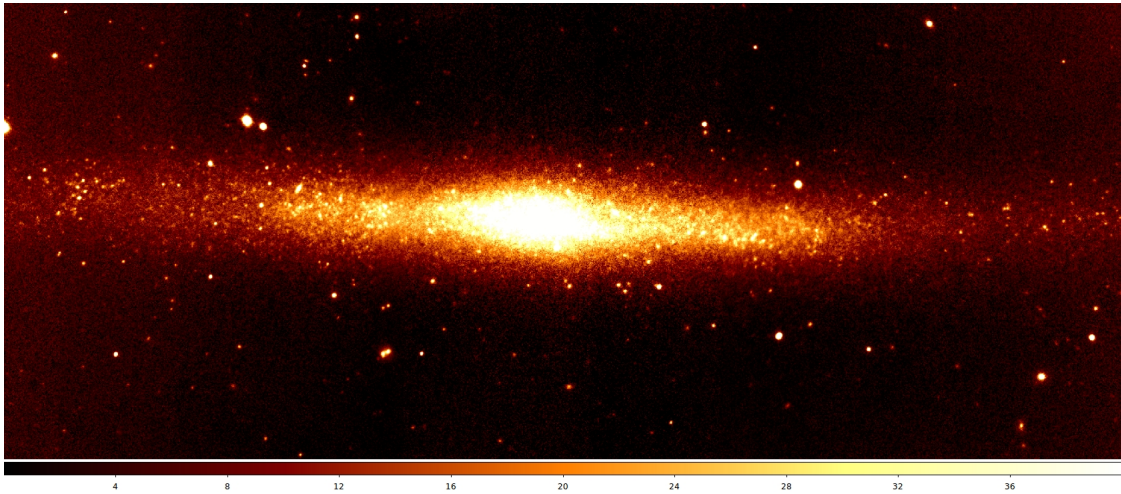
Figure A.8: K band image of NGC4244 from 3105 seconds of exposure on the TNG.
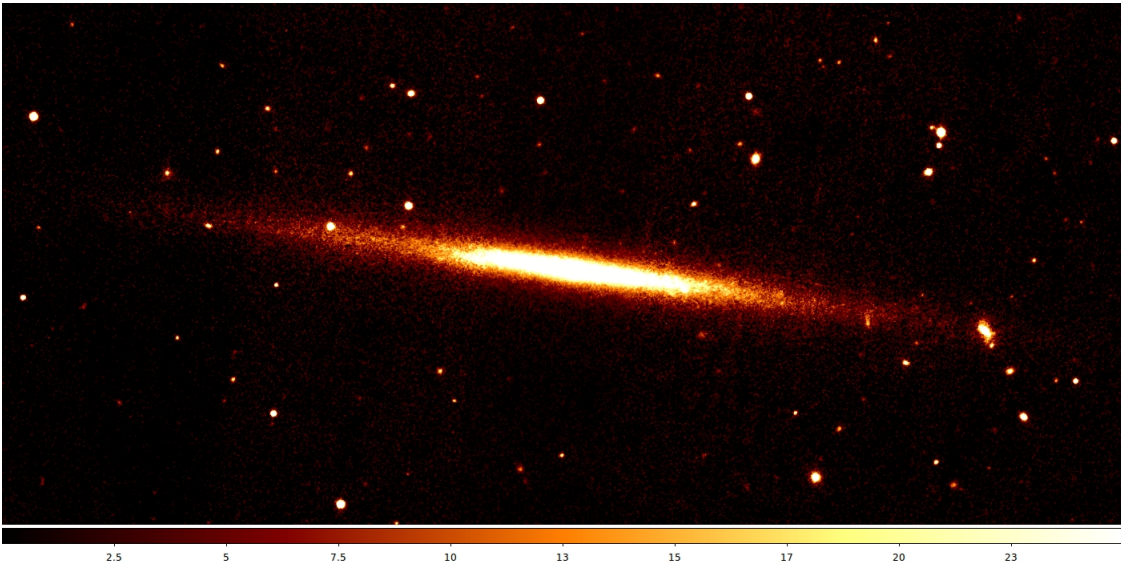
Figure A.9: K band image of UGC 7321 from 3105 seconds of exposure on the TNG.
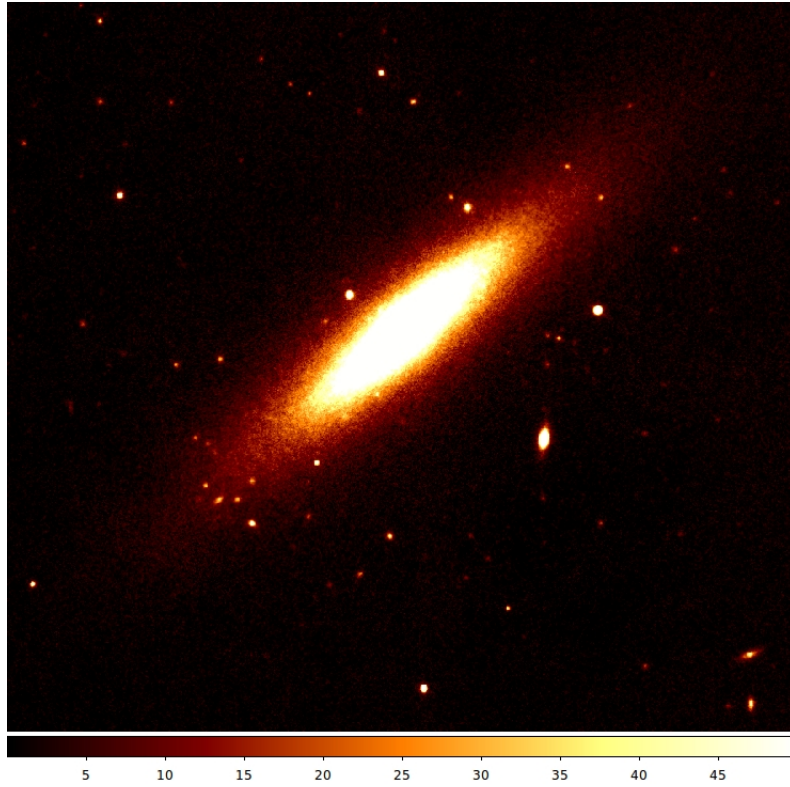
Figure A.10: K band image of NGC 4460 from 3105 seconds of exposure on the TNG.
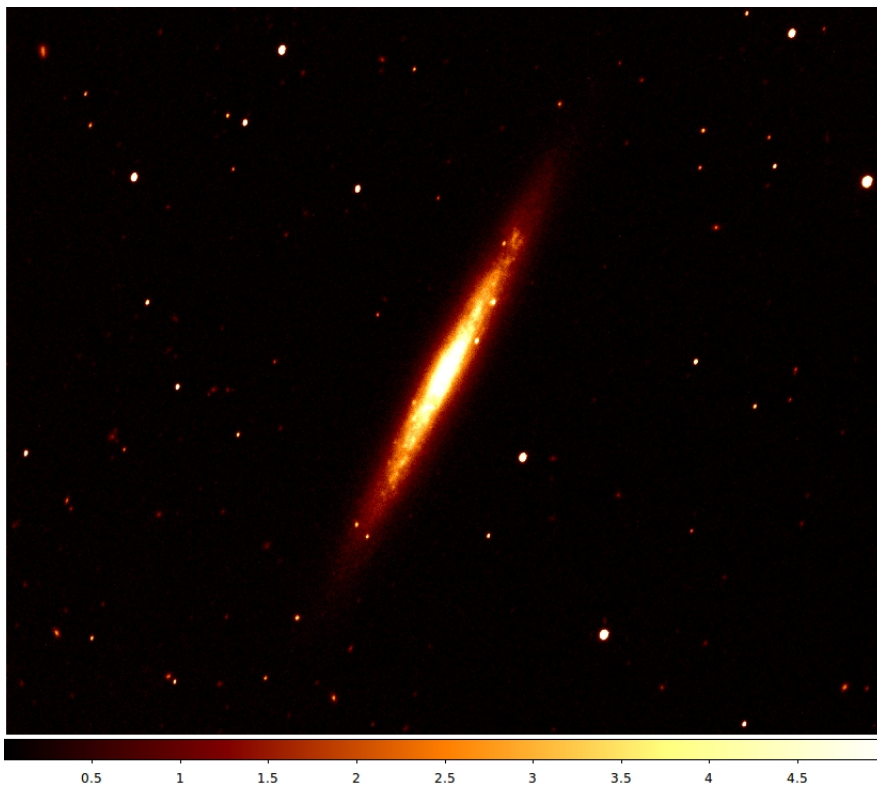
Figure A.11: R band image of NGC 5023 from 1800 seconds of exposure on the Skinakas 1.3 m telescope.

A.2.3   FRIEDL galaxies

Imaging for the Far-infraRed Investigation of Early-type galaxies with Dust Lanes was done during the observing runs at 2.1 m and 1.5 m telescopes at the San Pedro Martír observatory (chapter 5). Only the five northern galaxies were observed. New observations are scheduled for the remaining FRIEDL galaxies: NGC 2907, NGC 3283, NGC 5626, NGC 5799 and NGC 5866.
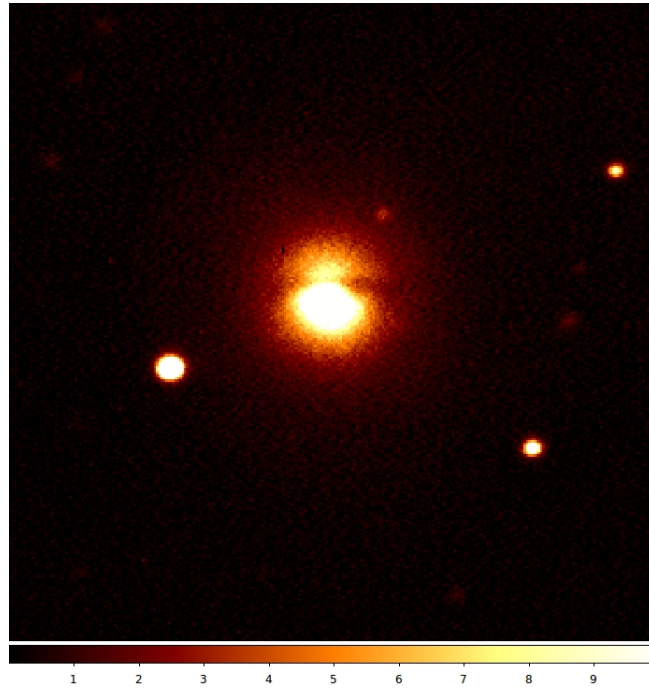
Figure A.12: B band image of NGC 2534 from 600 seconds of exposure on the SPM 1.5 m telescope.
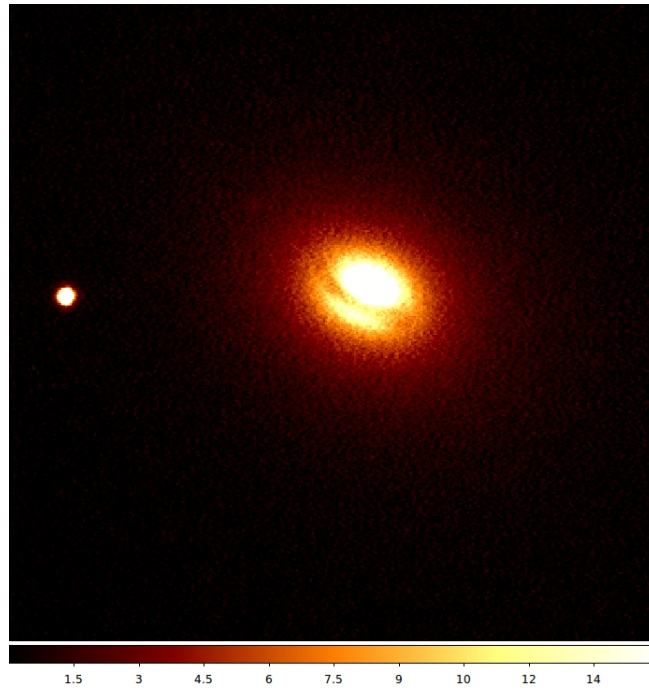
Figure A.13: U band image of NGC 3665 from 2400 seconds of exposure on the SPM 1.5 m telescope.
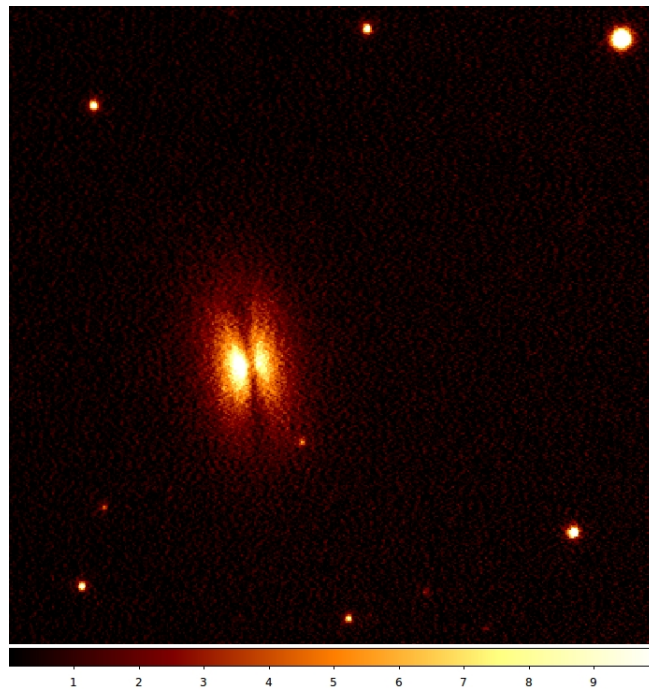
Figure A.14: U band image of NGC 4370 from 2400 seconds of exposure on the SPM 1.5 m telescope.
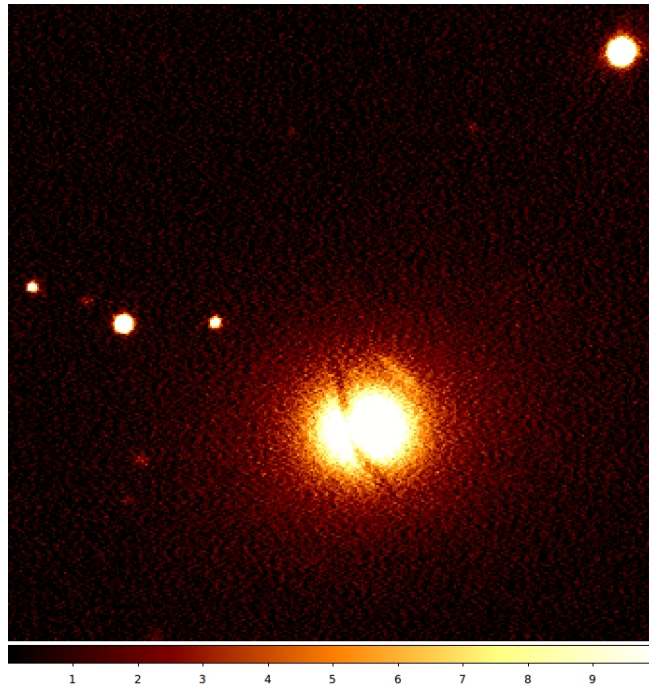
Figure A.15: U band image of NGC 5485 from 2400 seconds of exposure on the SPM 1.5 m telescope.

Figure A.16: U band image of NGC 5525 from 2400 seconds of exposure on the SPM 1.5 m telescope.

A.2.4   Other galaxies

Some galaxies were no part of a specific larger project such as the three covered here. Most of them will be used for single galaxy case studies.

Figure A.17: V band image of NGC 128 from 5400 seconds of exposure on the Skinakas 1.3 m telescope.
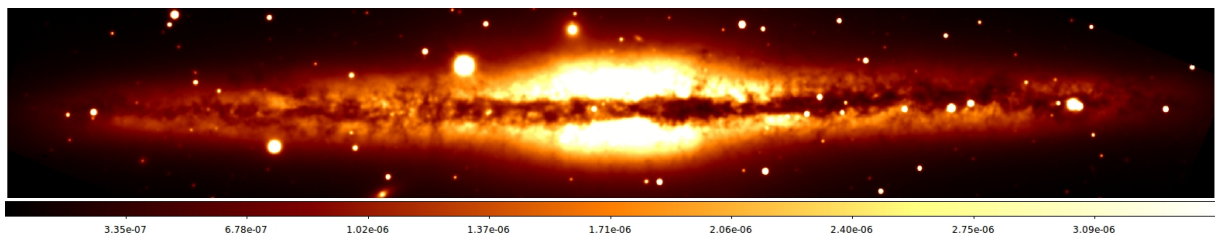
Figure A.18: Sloan r band image of NGC 891 from 1200 seconds of exposure on the WHT.
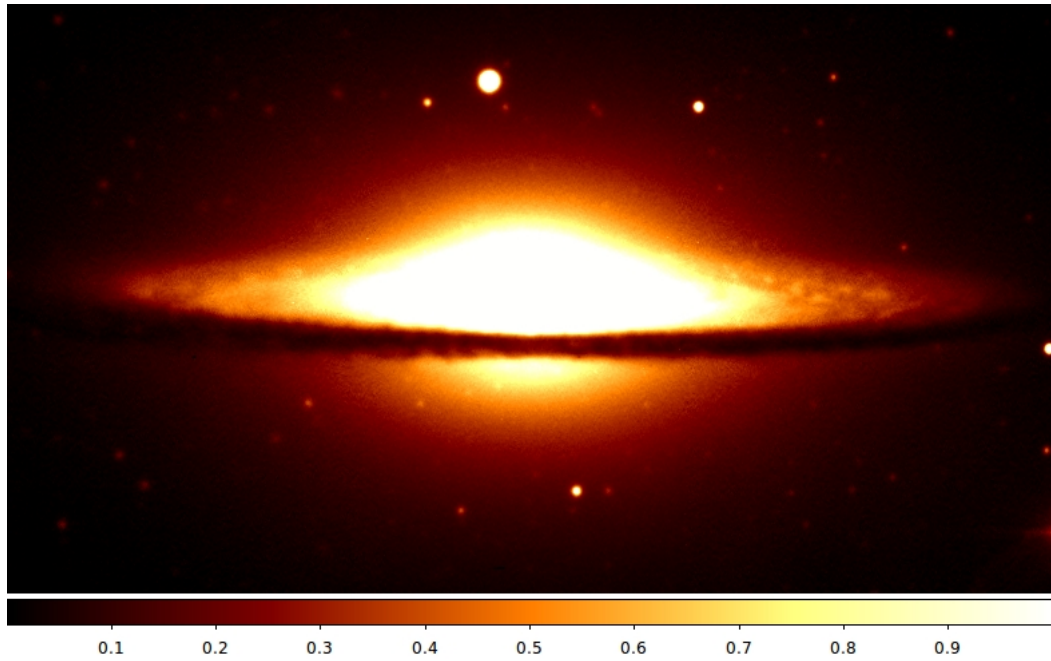
Figure A.19: B band image of M104, the Sombrero galaxy, from 600 seconds of exposure on the SPM 1.5 m telescope.
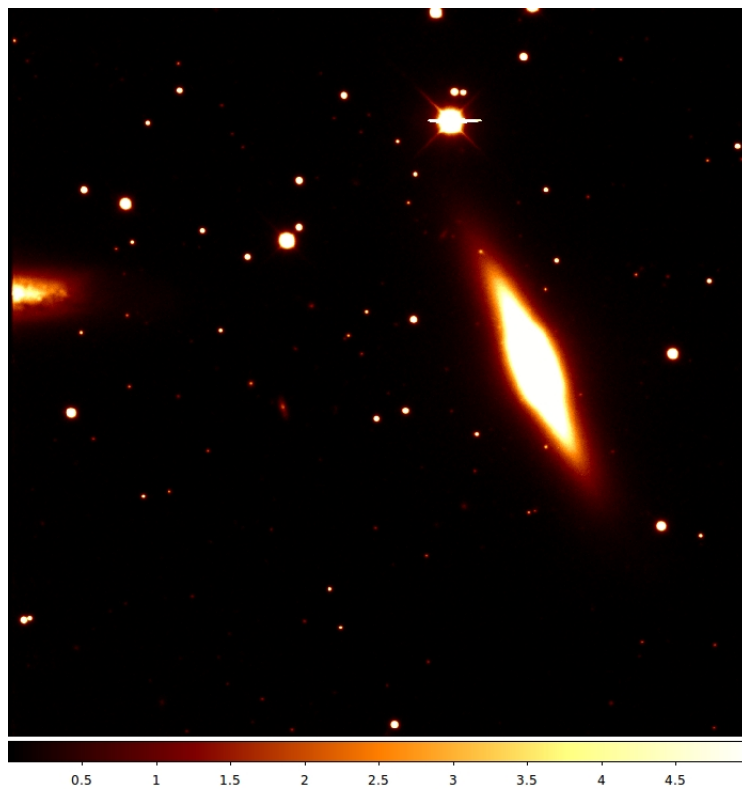
Figure A.20: V band image of NGC 7332 from 7200 seconds of exposure on the Skinakas 1.3 m telescope.

B Dust property maps of the FRIEDL galaxies

Chapter 6 mainly focusses on NGC 4370 to outline the techniques and procedures which lead to the general dust masses. This appendix holds the analogue results for the other galaxies of the FRIEDL subset.

B.1	Attenuation maps

Below are the attenuation maps of the five northern FRIEDL galaxies, derived from both MGE models (section 6.2) and colour index maps (section 6.1).

Attenuation maps from MGE models
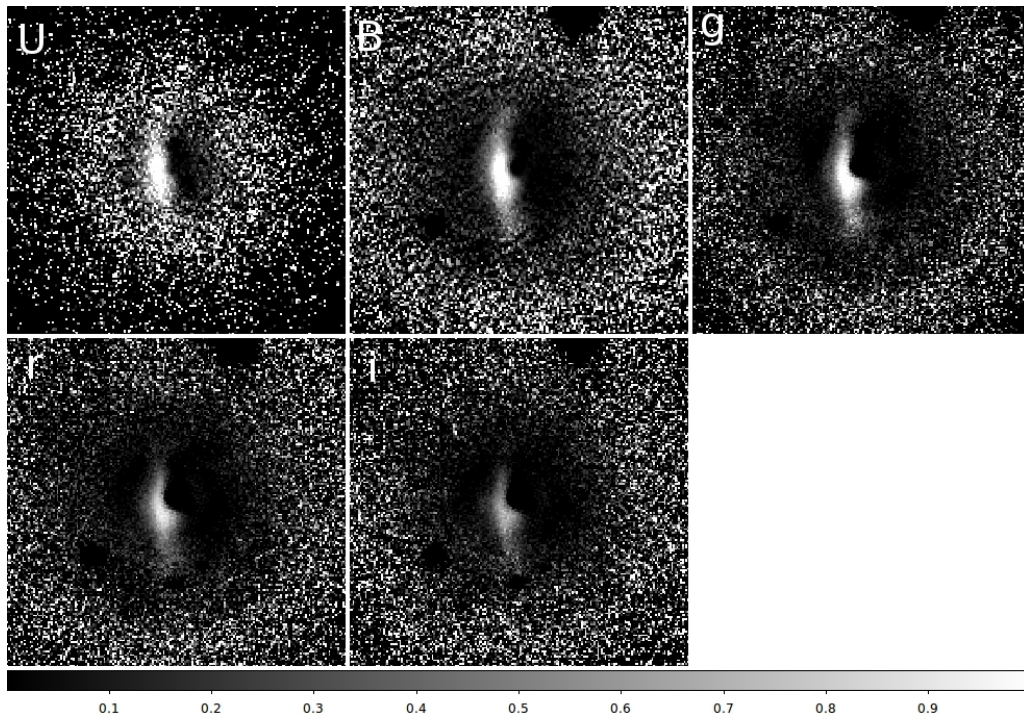
Figure B.1: Attenuation maps for NGC 2534. Note that no V band data was available for this galaxy.
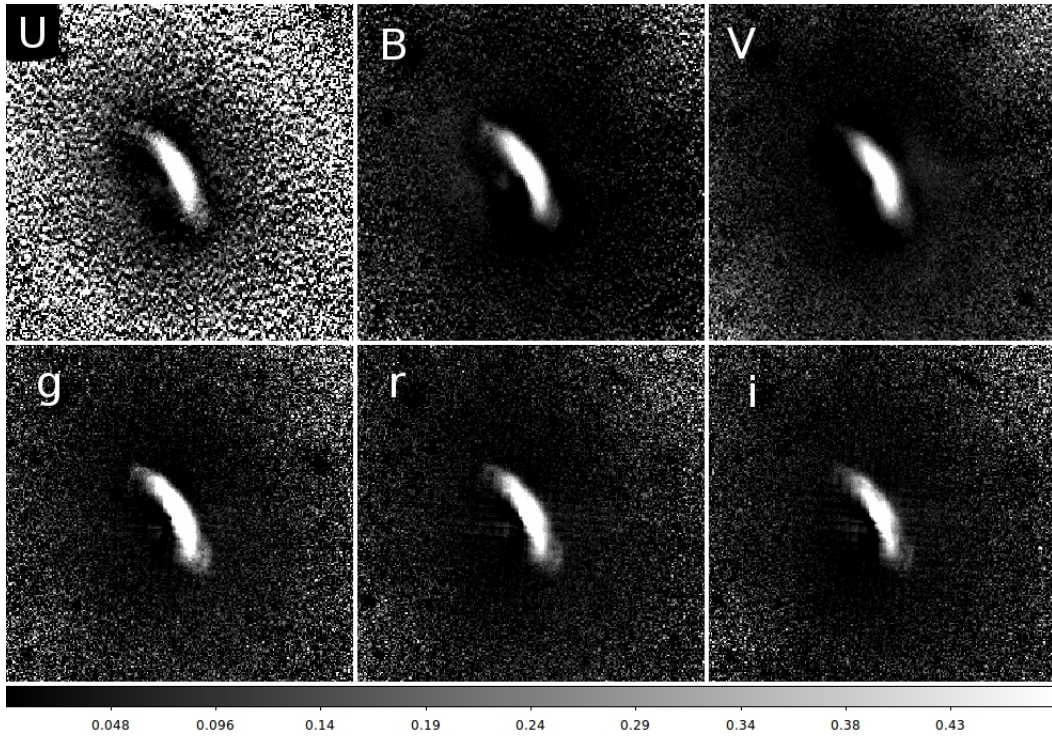
Figure B.2: Attenuation maps for NGC 3665 based on the MGE models.
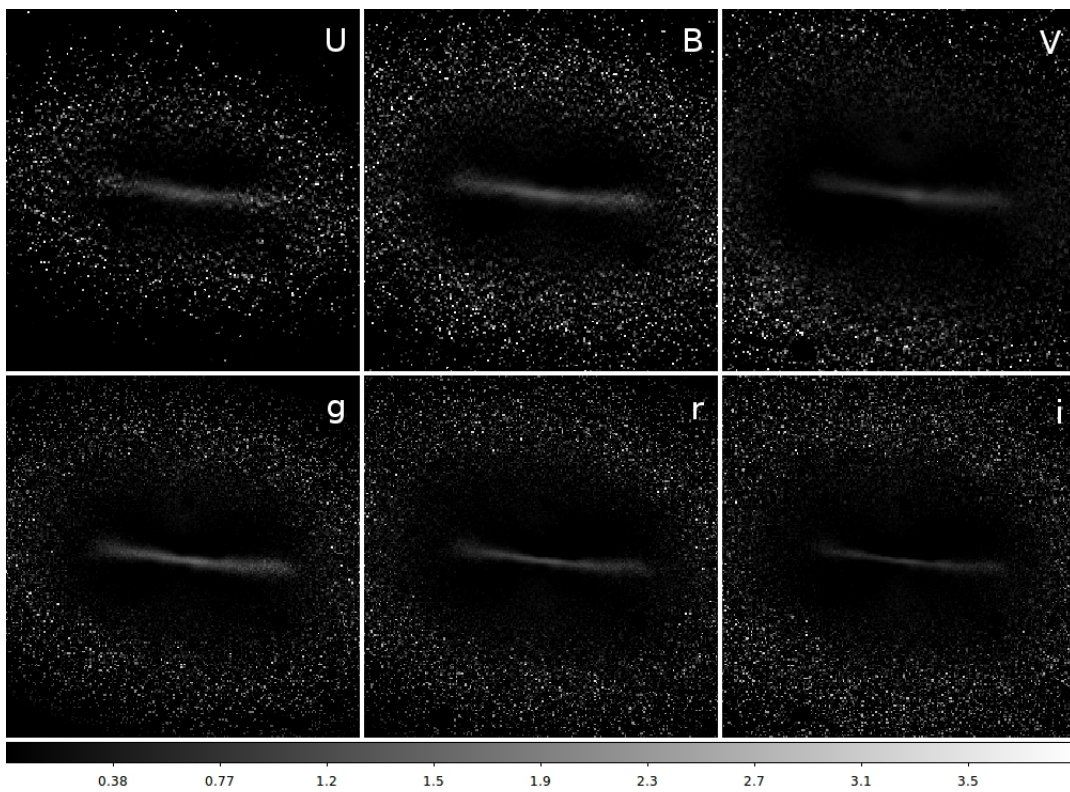
Figure B.3: Attenuation maps for NGC 4370 based on the MGE models.
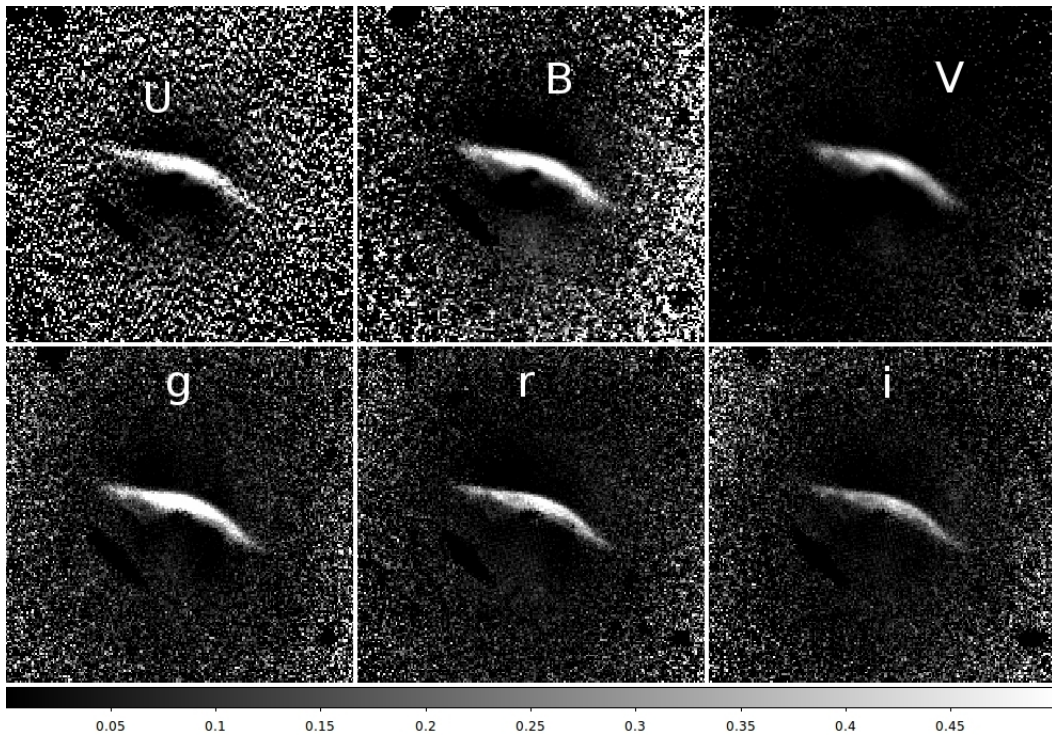
Figure B.4: Attenuation maps for NGC 5485 based on the MGE models.
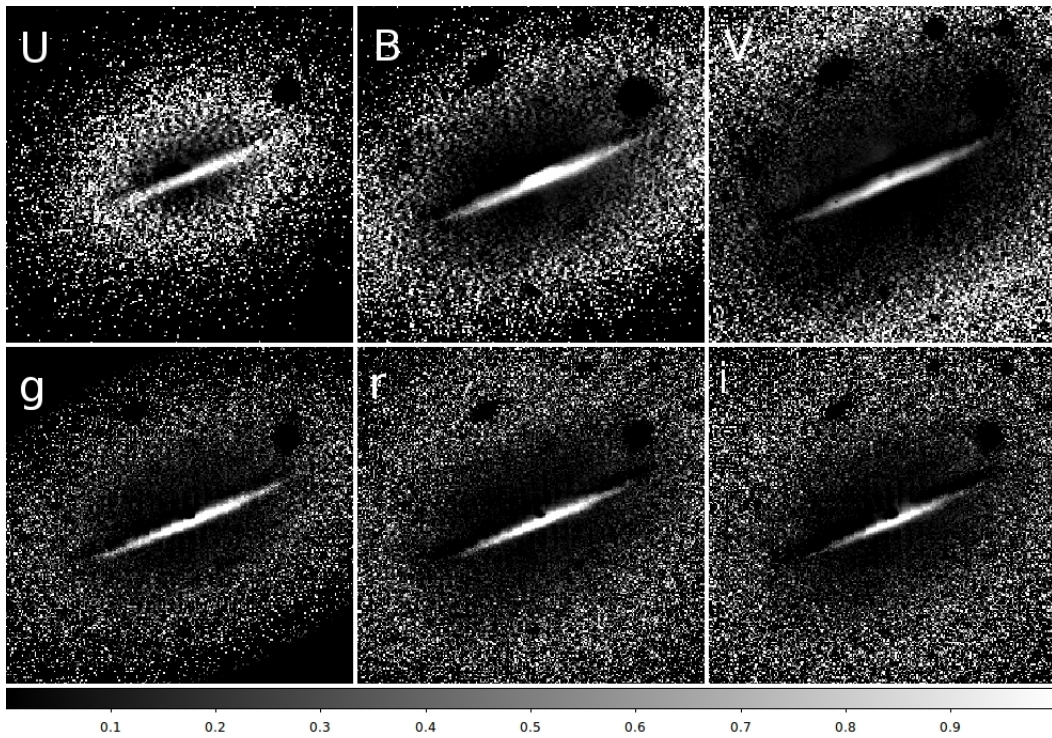
Figure B.5: Attenuation maps for NGC 5525 based on the MGE models.

Selective attenuation maps from colour maps
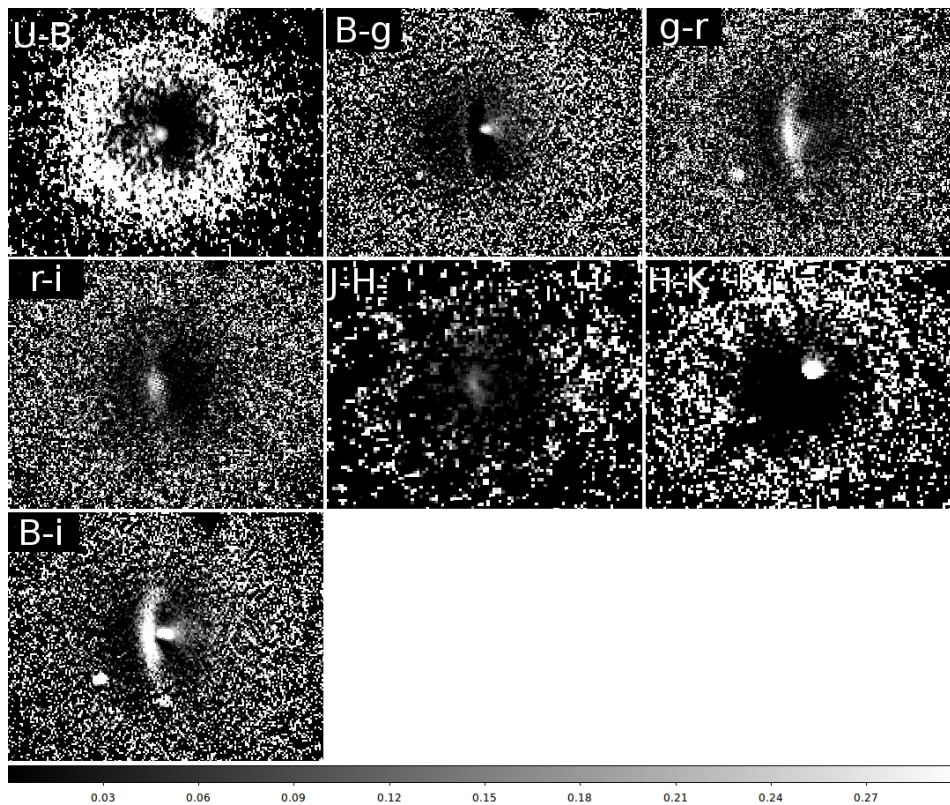
Figure B.6: Maps of selective attenuation for NGC 2534 based on the colour index maps. Note that no V band data was available for this galaxy.
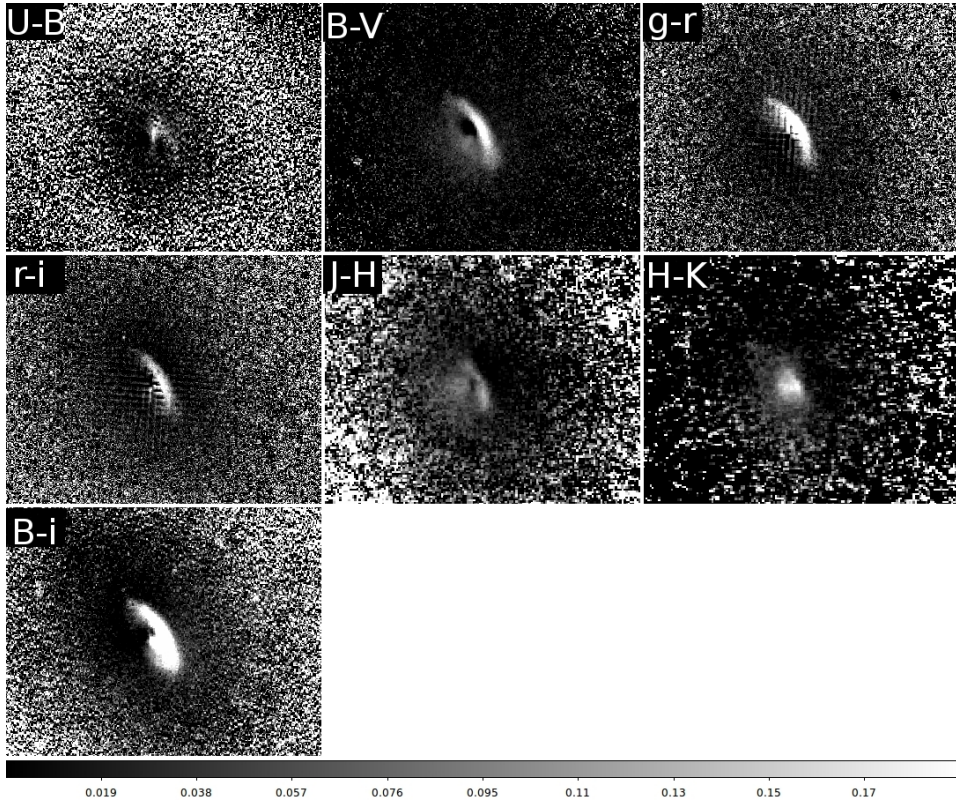
Figure B.7: Maps of selective attenuation for NGC 3665 based on the colour index maps.
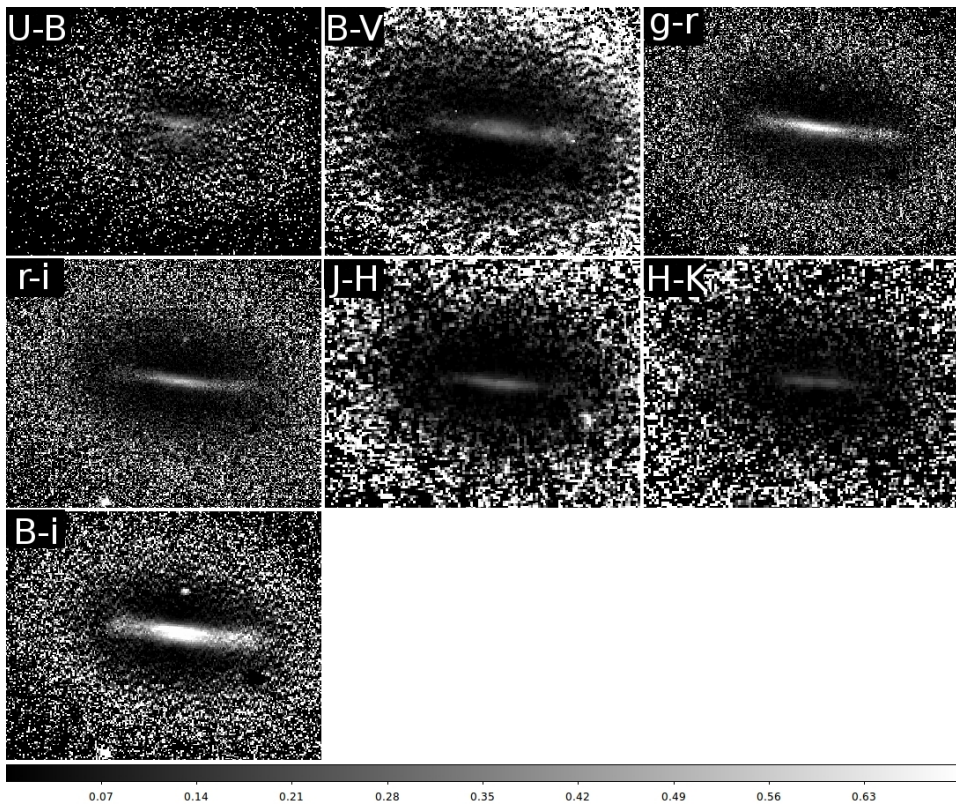
Figure B.8: Maps of selective attenuation for NGC 4370 based on the colour index maps.
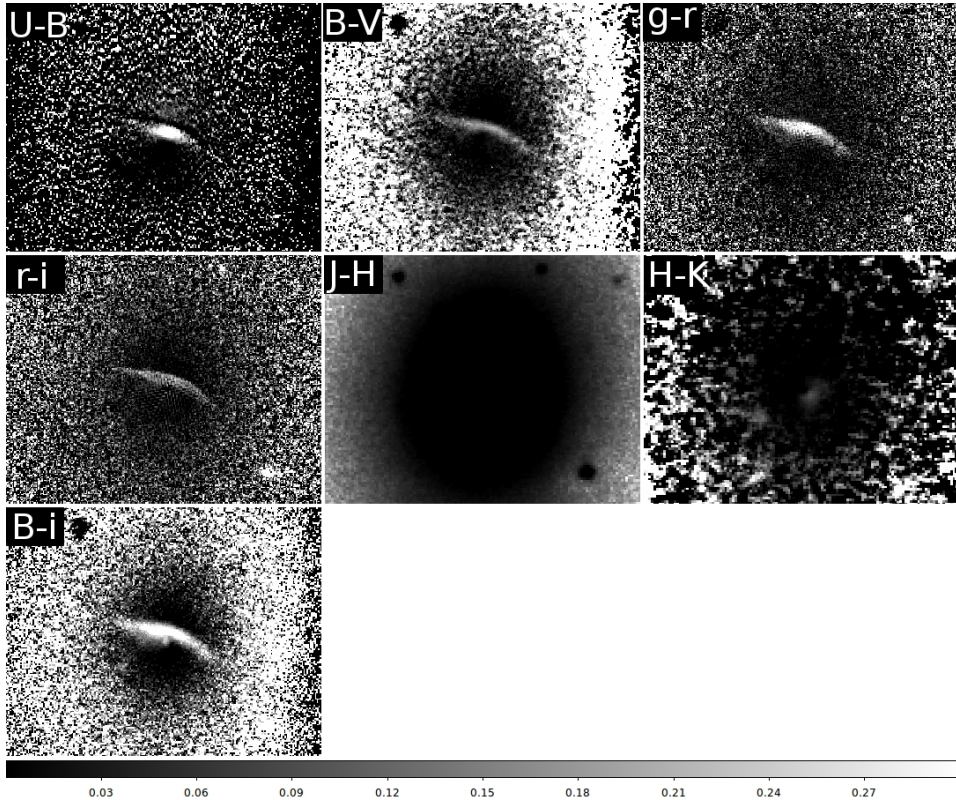
Figure B.9: Maps of selective attenuation for NGC 5485 based on the colour index maps.
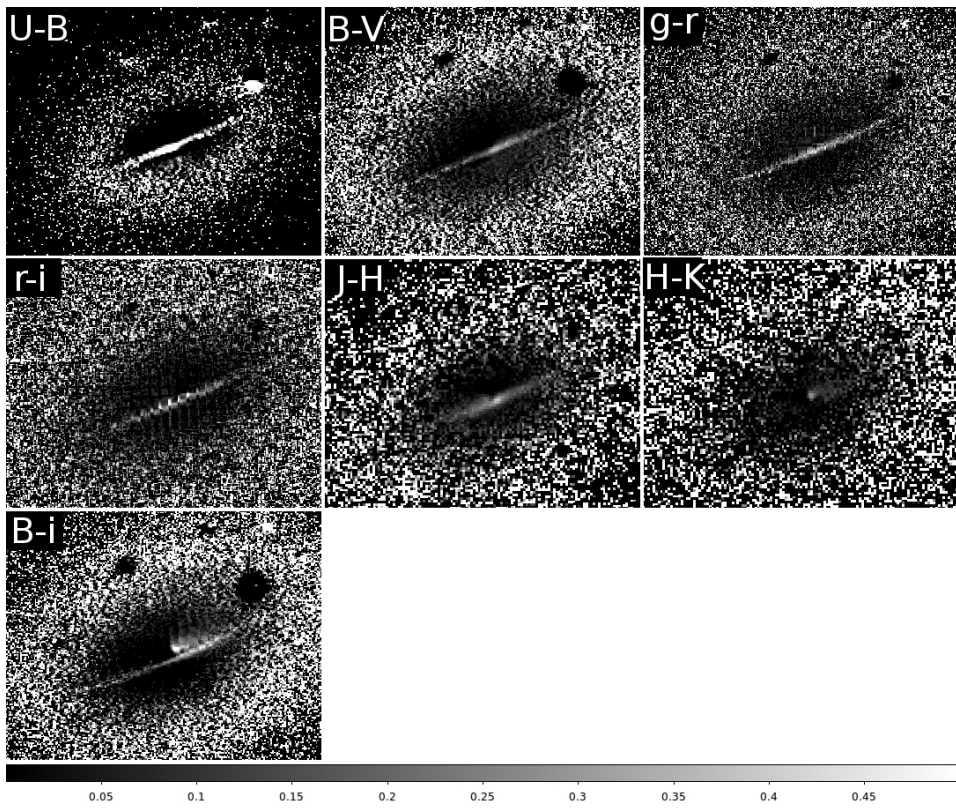
Figure B.10: Maps of selective attenuation for NGC 5525 based on the colour index maps.

Section 6.3 outlines the path to create dust maps from both MGE models and colour index maps. For reasons of saving paper and still remaining informative, only one set of dust maps for each galaxy is displayed. The other wavelengths and colours shared similar properties.
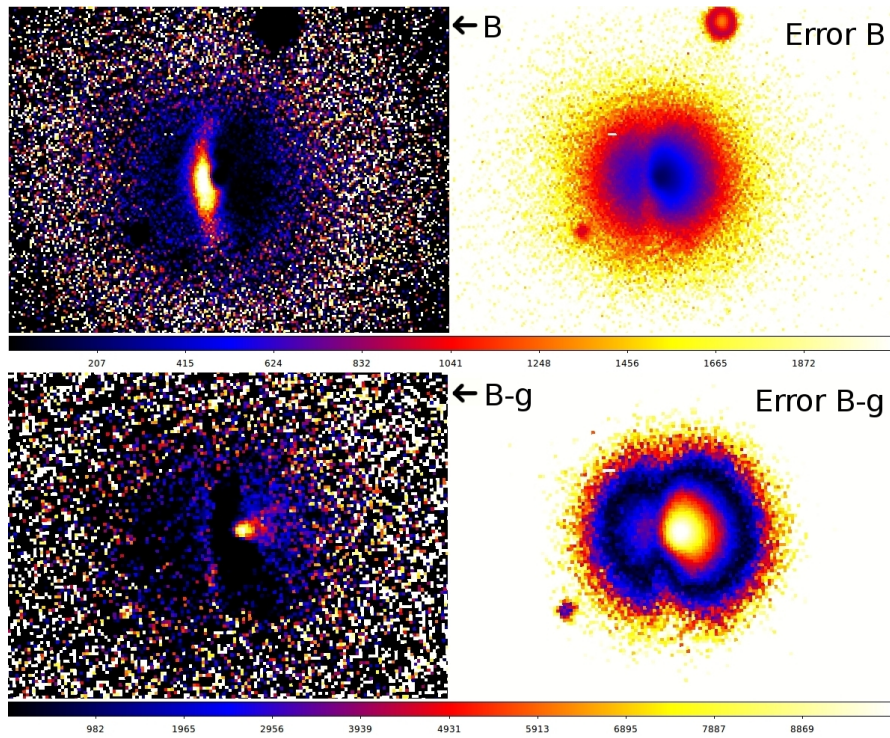
Figure B.11: Dust maps and their corresponding error maps for NGC 2534.
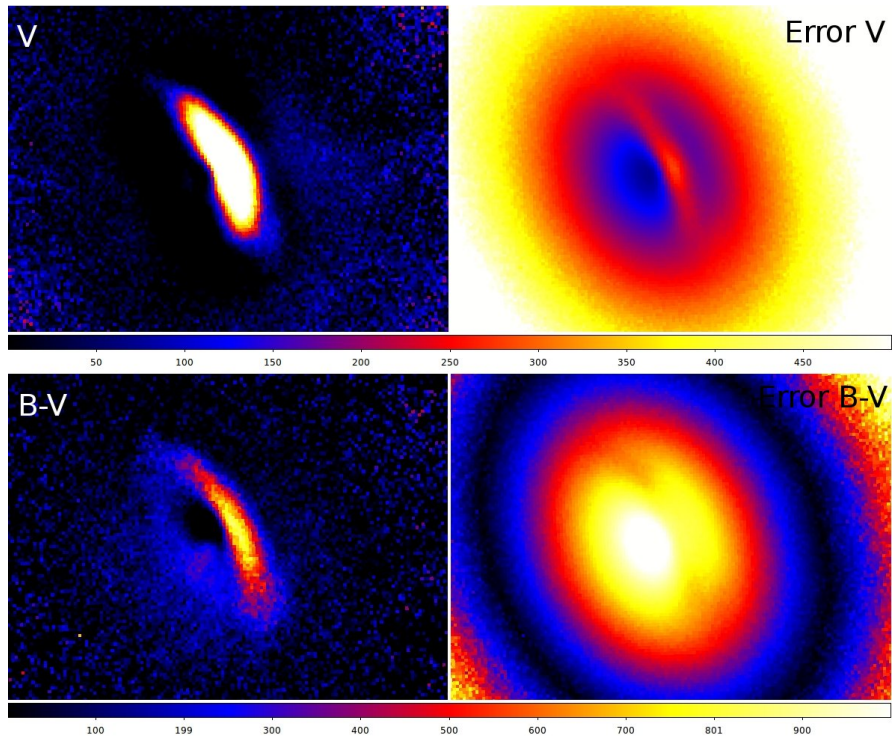
Figure B.12: Dust maps and their corresponding error maps for NGC 3665.
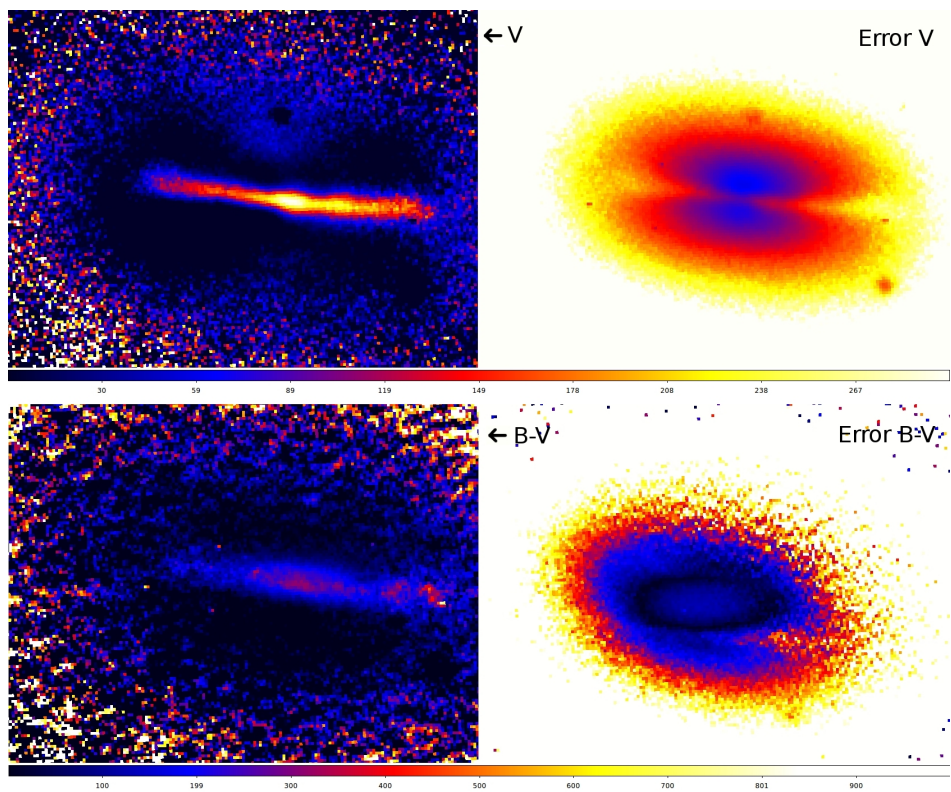
Figure B.13: Dust maps and their corresponding error maps for NGC 4370.
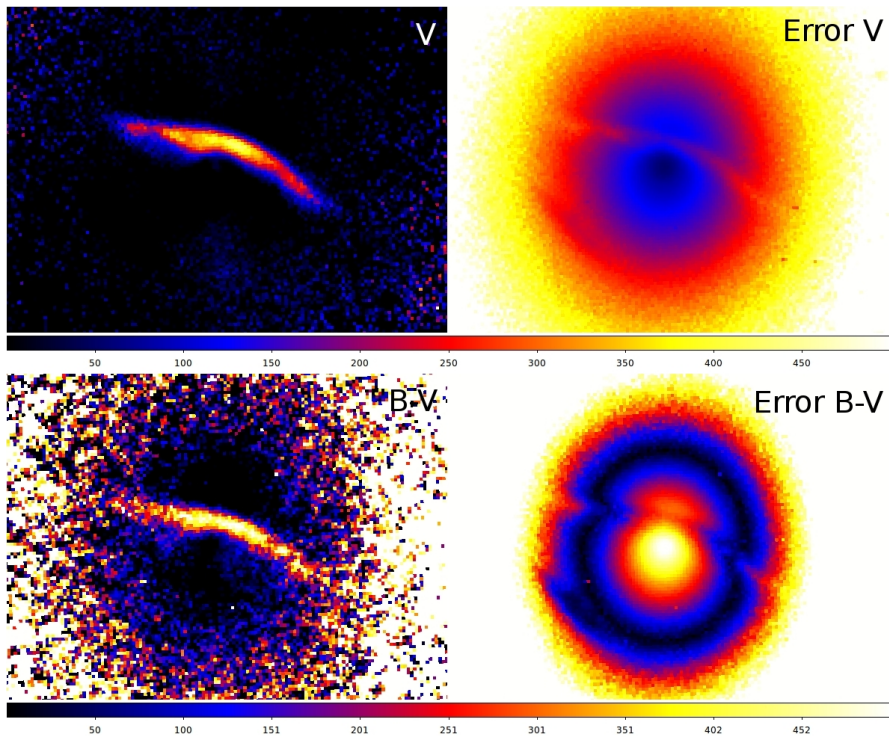
Figure B.14: Dust maps and their corresponding error maps for NGC 5485.
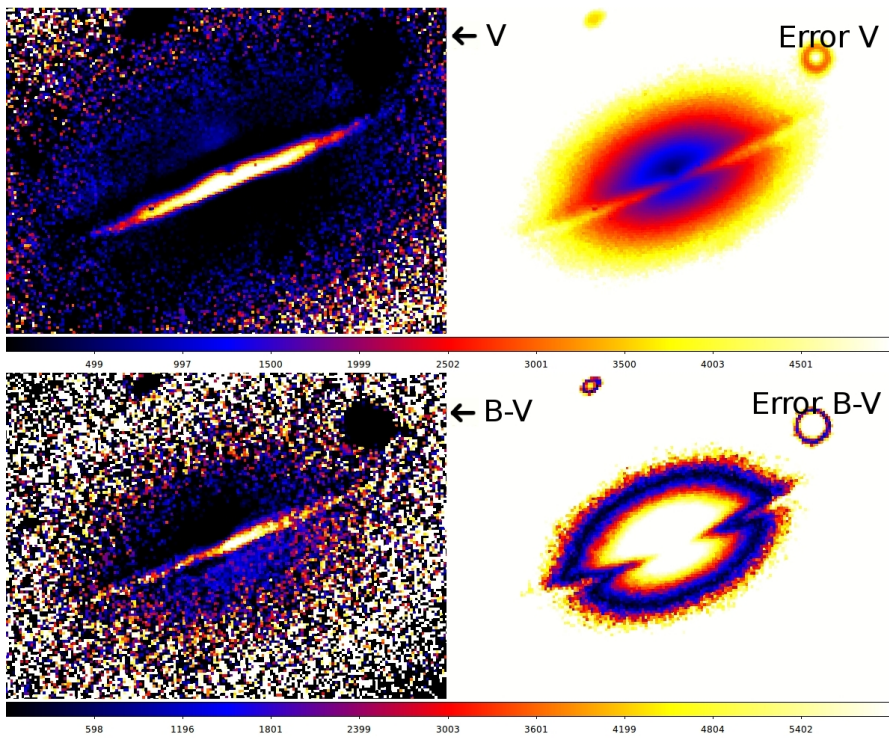
Figure B.15: Dust maps and their corresponding error maps for NGC 5525.

Total dust masses for each of the galaxies were derived according to the procedures outlined in section 6.4. In analogy of figure 6.15, composite plots of the general dust mass fits are displayed below.
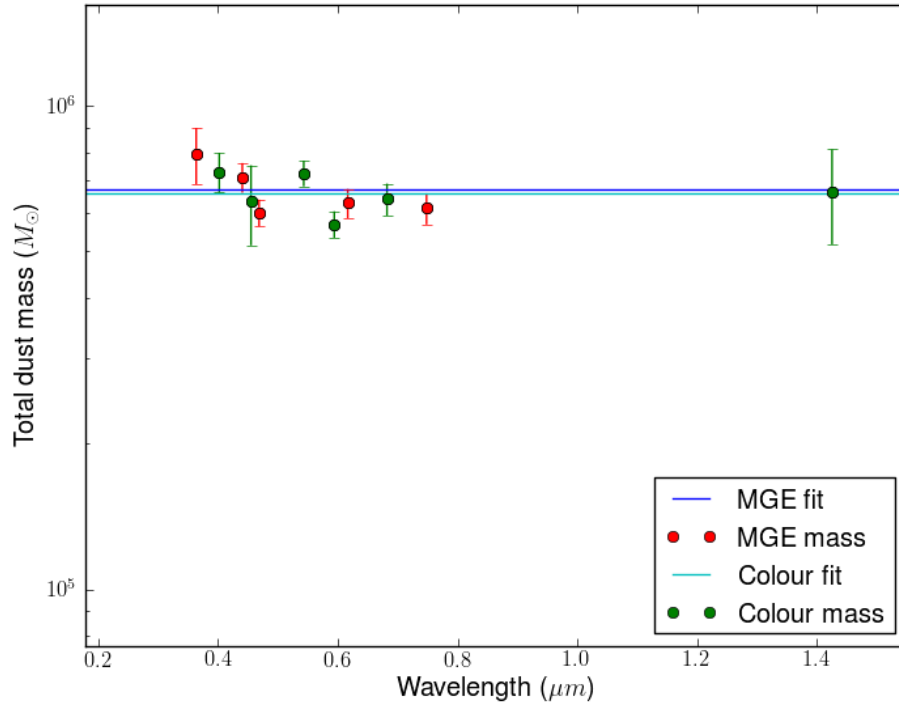

Figure B.16: Fitted dust masses for NGC 2534, based on the two approaches.
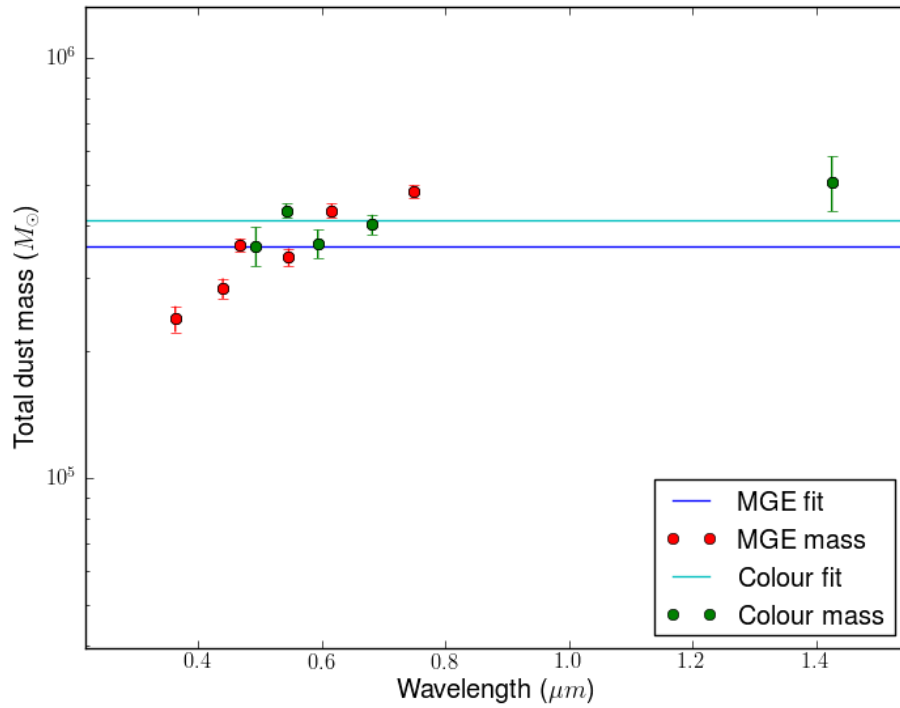
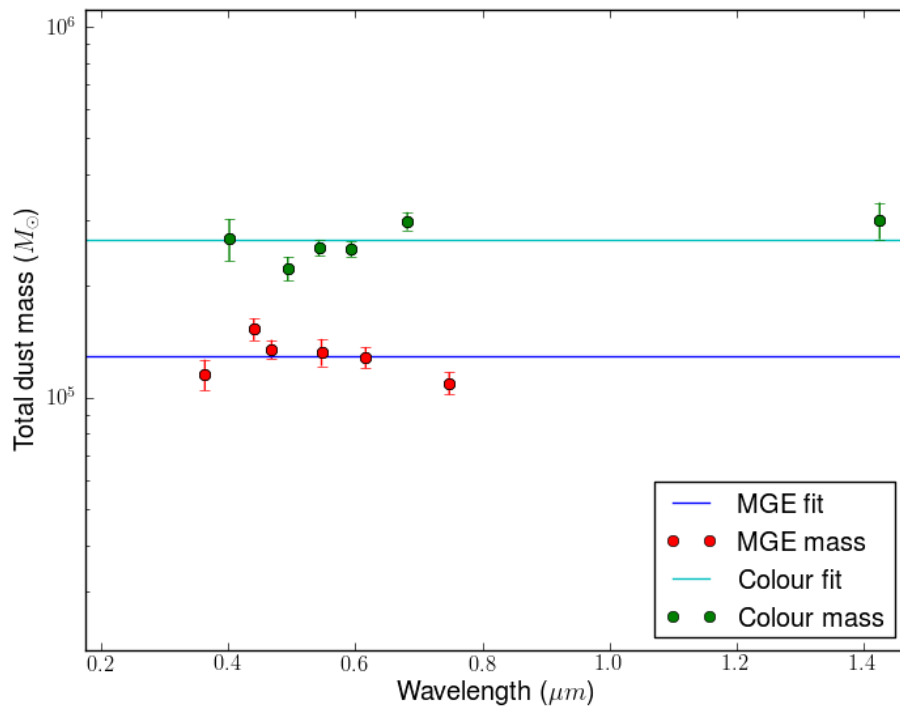**Figure B.17:** Fitted dust masses for NGC 3665, based on the two approaches.

Figure B.18: Fitted dust masses for NGC 4370, based on the two approaches.
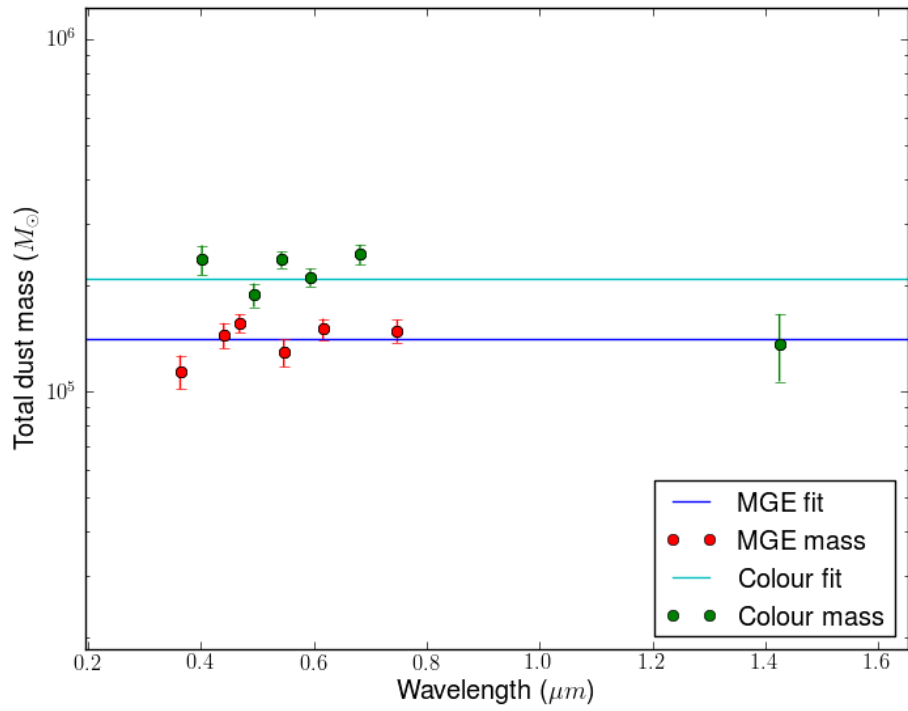
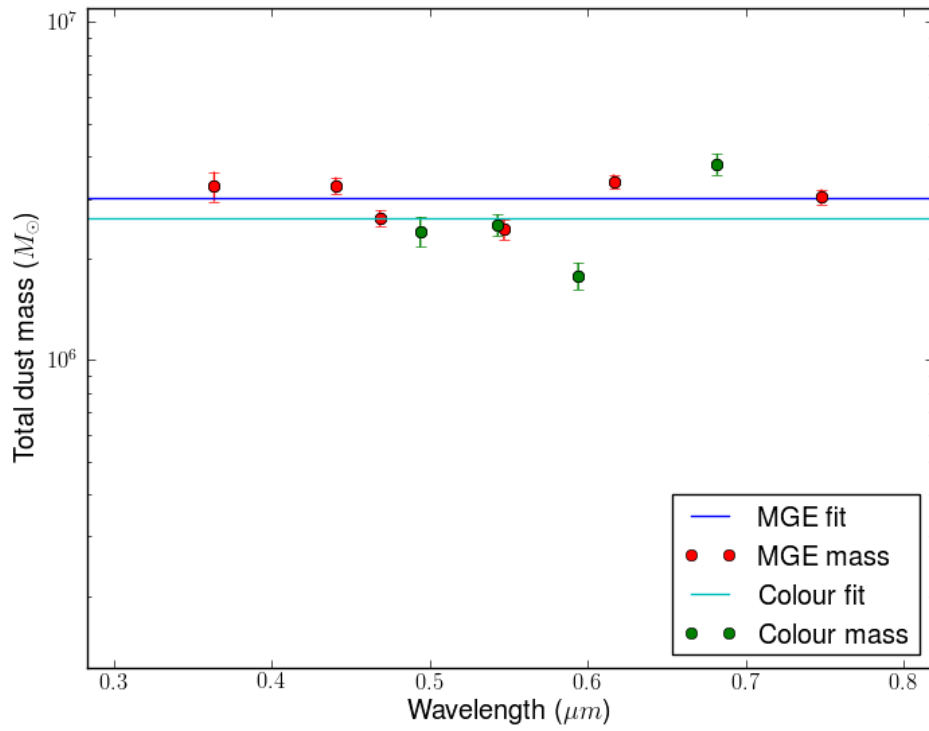**Figure B.19:** Fitted dust masses for NGC 5485, based on the two approaches.

Figure B.20: Fitted dust masses for NGC 5525, based on the two approaches.